Modeling Hexacopter's Flight Dynamics on Earth and Martian Surface Using FLIGHTLAB

a project presented to

The Faculty of the Department of Aerospace Engineering

San Jose State University

In partial fulfillment of the requirements for the degree

Master of Science in Aerospace Engineering

By

Raghuvir Singh

December 2022

approved by

Dr. Carlos Malpica
Mentor

Dr. Maria Chierichetti
Faculty Advisor

San José State
UNIVERSITY

ABSTRACT

Modeling Hexacopter's Flight Dynamics on Earth and Martian Surface Using FLIGHTLAB

Raghuvir Singh

The use of rotorcraft have expanded the range of surface which is not explorable by traditional landers and rovers. Due to uneven, rocky terrain on Marian surface, aerial mobility can assist in discovering the areas where ground vehicles are not able to travel to. The very first rotorcraft planetary mission was conducted in 2021. The tech demonstrator knows as Ingenuity was deployed to Mars to show its capability of flying in an environment where density and gravity is less than that of Earth's. After many successful flights performed by Ingenuity within the last year, Ingenuity have opened up many possibilities for a second-generation Mars rotorcraft that can conduct mission on its own. One of the main requirements of Mars mission is to perform fully autonomous flight from the beginning to the end. This requirement puts heavy reliance on analyzing flight behavior on Mars' atmosphere before manufacturing or deploying a rotorcraft to the Martian surface. Moreover, considering no vehicle can be brought back easily in case of any failures, the second-generation rotorcraft should have enough redundancy to continue its missions on Mars, in case a failure does occur. In this project, a hexacopter is considered as one of the second-generation rotorcraft since a hexacopter holds redundancy of flying in case one or two rotors do fail. This project utilizes FLIGHTLAB to model differences in flight behavior in both Earth and Mars' environments. FLIGHTLAB is high fidelity comprehensive analysis tool that is capable of modeling aerial vehicles in user defined environments. Four Frequency responses such as heave, pitch, roll, and yaw rates of the hexacopter in hover are analyzed. Based on the obtained results, it is determined that each attitude response of designed hexacopter responds very differently in both Earth and Mars' atmosphere. The pitch response is stable in both Earth and Mars' atmosphere, whereas the roll response is stable on Earth and unstable on Mars. Therefore, the technique of applying only proportional gain cannot be utilized to stabilize all four responses being analyzed in this project. It is best to further carry the research and analyze flight behavior differences in different configurations in the future. Analyzing different flight configuration in both environments will help understand flight behavior differences thoroughly and determine if a dynamically matched surrogate rotorcraft can be designed to perform testing on Earth.

ACKNOWLEDGEMENTS

I would like to express my sincere gratitude towards several individuals who have guided me throughout my graduate studies. At first, I would like to express heartful appreciation to Dr. Carlos Malpica for making himself available for me whenever I needed some guidance inregards to the project. Meeting with him every day really kept me motivated and his valuable advice helped me overcome many challenges that I faced during the project. I look forward to working under your guidance to determine if a dynamically matched surrogate hexacopter can be designed for testing on Earth. Thank you once again for being understanding, kind, and making yourself available and teaching me valuable rotorcraft lessons relevant to this project. I would also like to express my gratitude towards Dr. Wayne Johnson for his very insightful observations regarding FLIGHTLAB and his help with understanding CAMRAD output files. Dr. Wayne Johnson was kind, patient and encouraging whenever I ran into problems with FLIGHTLAB. I would also like to express my gratitude towards our branch chief Dr. William Warmbrodt for letting me be the first one in the branch to conduct a project with FLIGHTLAB which will help the branch conduct more studies in the near future. Dr. Warmbrodt kept me motivated by appreciating the work and time I have put into the project. I would also like to thank my advisors Dr. Maria Chierichetti and Dr, Nikos Mourtos for their guidance and support over the last several years. Dr. Chierichetti have been very helpful and welcoming as my faculty advisor. She provided me with her valuable thoughts and feedback throughout the project. Thank you Dr. Mourtos for your guidance for the last several years. Both of their expertise have helped me succeed and learn valuable topics. Lastly, I would also like to thank my fiancé and family for keeping me motivated and being understanding as I dedicated my time towards this project.

TABLE OF CONTENTS

LIST OF TABLES

LIST OF FIGURES

NOMENCLATURE

ω_o	=	nondimensionalized flap frequency
Υ	=	is the ratio of aerodynamic to inertial forces
ρ	=	air density
c	=	chord length
M	=	Mach
°	=	Degree
$C_{l\alpha}$	=	lift curve slope of the blade
R	=	rotor radius
I	=	blade inertia about flap hinge
ψ_b	=	blade azimuth
ψ_{b0}	=	phase angle
$r_{c/i}^{i}$	=	displacement vector of the child frame with respect to the parent frame expressed in the inertial coordinate system
$T_{p/i}^{T}$	=	transformation matrix from inertial coordinate system to parent coordinate system.
$v_{c/i}^{c}$	=	translation velocity vector of the child frame with respect to the initial frame expressed in the child coordinate system
$w_{p/i}^{p}$	=	angular velocity vector of parent frame with respect to the inertial frame expressed in the parent coordinate system
$a_{c/i}^{c}$	=	translation acceleration vector of child frame with respect to the inertial frame expressed in the child coordinate system.
$w_{p/i}^{\prime p}$	=	angular acceleration vector of the parent frame with respect to the inertial frame expressed in the parent coordinate system
α	=	angle of rotation
$T_{\frac{c}{p}}$	=	transformation with y-axis of rotation
(γ, ϕ, θ)	=	transformation angles about x, y, and z
γ'	=	Transformation angle rate about x
θ'	=	Transformation angle rate about y
ϕ'	=	Transformation angle rate about z
p, q, r	=	Roll, pitch and yaw motion
C_{T_f}	=	thrust coefficient
θ_0	=	blade collective pitch
B	=	tip loss factor
r_t	=	blade root cutout
θ_{tw}	=	blade twist
σ	=	rotor solidity
L	=	Lift
D	=	Drag
c_0	=	Zero lift angle
U_T	=	Tangential velocity
δ_3	=	pitch flap coupling factor

μ_x	=	longitudinal advance ratio
C_n^P	=	linear normal force coefficient
q	=	step change in non-dimensional pitch rate
S	=	distance traveled by the airfoil section in semi-chords
M	=	Mass matrices
C	=	Damping matrices
K	=	stiffness matrices

Chapter 1. Introduction

1.1.Motivation

Mars known as the Red Planet, provides an ideal landscape to understand the early history of transformation of the solar system. Planets like Mars, Venus, and Earth are all formed from the same minerals and elements; however, all three planets went through different transformations. Unlike Earth's atmosphere, Mars' surface pressure is only 1% of the surface pressure of the Earth [1]. Moreover, Mars contains history of dehydration, loss of its atmosphere and surface water turning into ice. Research is being conducted to understand Mars as a planet. Specifically, NASA's Mars Exploration Program is studying the formation and early evolution of Mars as a planet, the history of geological processes, the potential for Mars to have hosted life, and the future exploration of Mars by humans [1]. With the advancement in technology and knowledge, the research has evolved from "Follow the Water" to "Explore Habitability" to "Seek Signs of Life" [1]. Like the evolvement in strategy, the means to conduct Mars exploration has also evolved over time.

The exploration became more sophisticated with the use of orbiters, stationary landers, rovers and now aerial vehicles [2]. Orbiters like MAVEN helped explore the upper atmosphere of Mars. Stationary landers like Insight made it possible to detect quakes on Mars and revealed details about the depth and composition of Mars' crust, mantle, and core [3]. The Perseverance rover helped understand the dust processes on Mars and contributed to a body of knowledge that could one day help predict the dust storms that Mars is famous for, which poses a threat to future robotic, and human explorers. Moreover, the rover is also designed to seek the evidence of life and accumulate rocks and soil to conduct future mission and bring samples back to the Earth [1]. Stationary landers and rovers have spread over distances in search of new knowledge [2], however the aerial dimension of Mars is still yet to be full discovered.

To discover the aerial dimension of Mars through atmospheric flyers, NASA sent a small helicopter as a tech demonstrator to the Martian surface. The Ingenuity Mars Helicopter was sent to verify the possibility of using helicopters as a means of conducting future Mars' exploration. Using helicopters for Mars' exploration links a resolution gap of low-resolution large area imagery provided by orbiters to the rovers that can only obtain detailed images within their limited line of sight [2]. A helicopter can be used to create a forward reconnaissance platform; thus, mapping the best and the most suitable terrain ahead of a rover. With further advancement in technology, a helicopter may carry its own payload to areas that are not accessible through rovers [2].

More research needs to be conducted for a helicopter to conduct an independent science mission on Mars. This project will model flight behavior of a hexacopter in both Earth's and Mars' environment, such that a dynamically equivalent surrogate helicopter can be created to conduct flight testing on Earth.

1.2.Literature Review

1.2.1. Past Mars Rotorcraft Studies

The idea of flying on Mars has been around since early days of space exploration. The idea of flying in thin, cold and CO_2 based environment became prevalent after the Viking Lander Mission of the 1970s [2]. The idea of flying on Mars using compressed gas was first introduced by Savu and Trifu in mid 1990s [4]. Soon after, the University of Stanford and JPL tested a small rotorcraft under Mars' atmospheric conditions in JPL's own vacuum chamber [5]. Even though no data was published from the above research, they certainly opened up the arena of flying on Mars. At the same time, NASA Ames conducted research on possible conceptual design of rotorcraft for Mars exploration. Young, Chen, and Briggs discusses the possible challenges associated with developing autonomous vertical lift planetary aerial vehicles (PAVs) [6]. Young, et.al concluded that vertical lift planetary aerial vehicles could potentially be developed for planets like Mars, Venus, and Titan [6]. Following the research, University of Maryland and Georgia Institute of Technology formed possible designs of Martian rotorcrafts. The University of Maryland produced the "Martian autonomous rotary wing vehicle (MARV)". MARV was a coaxial helicopter designed to carry a payload of 10.8 kg with an endurance of 39 min [7]. Separately, the Georgia Institute of Technology developed a quad-rotor design with rotors of 1.84 m in diameter and endurance of 30 min [8]. Figure 1.1 shows the MARV and GTMARS designs developed by both institutes.

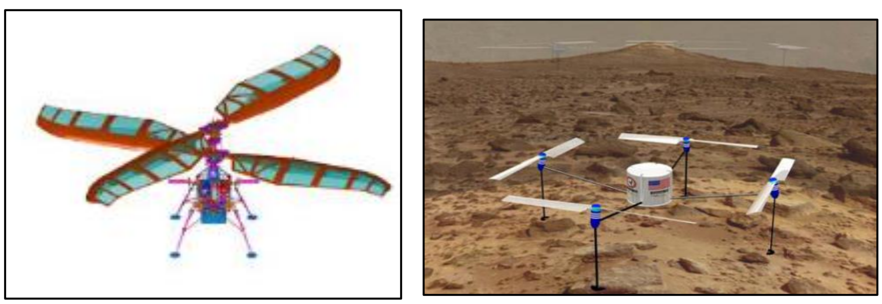

Figure 1.1: Martian rotorcraft designs: MARV [10] and GTMARS [11].

Soon after the development of the above Martian rotorcrafts, many other rotorcraft concepts were produced. Mars UAV concept was produced by the Georgia Institute of Technology. Figure 1.2 illustrates the concept, a combination of a ground rover and a rotary-wing UAV, designed to use for exploration purposes [9] . Tohoku University also came up with a four-rotor conceptual design that met Mars' flying requirements and restrictions. Figure 1.3 and Table 1.1 shows design specifications of Mars helicopter designed by Tohoku University [10]. The main body of the design was developed to carry all necessary avionics and the mission payload. The legs of the helicopter were designed hemispherical such that the helicopter can land on uneven, rocky surface of Mars.

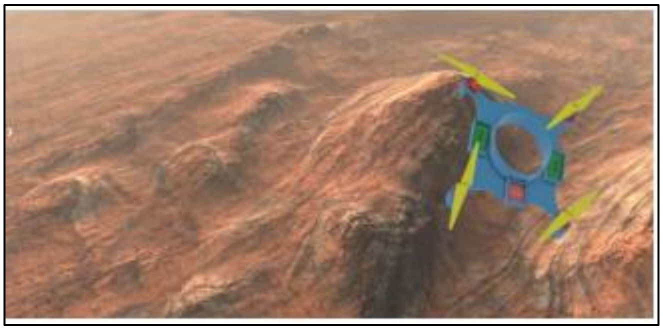

Figure 1.2: UAV design by Georgia Institute of Technology [9]

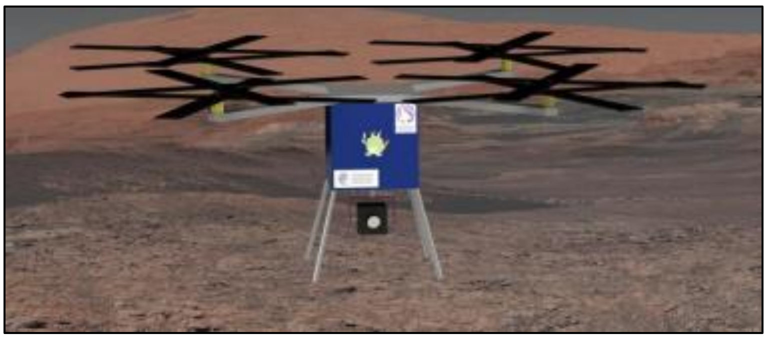

Figure 1.3: Mars Helicopter design by Tohoku University [10].

Table 1.1: Tohoku University mars helicopter specifications.

Parameter	Value
Rotor Radius	0.5 m
Helicopter Radius	1.3 m
Total Mass	10.7 m
Horizontal Flight Distance	100 m
Flight Time	422 s

Following the developments described above, a tech demonstrator known as Ingenuity was developed as a collaboration between Jet Propulsion Laboratory and NASA Ames Research Center [11]. Ingenuity features a coaxial rotor that are counter-rotating hinge less two bladed rotors. Each rotor measures 1.21 m in diameter and is approximately 0.096 m apart from the other [12]. The rotors performed at 2800 rpm at atmospheric densities ranging from 0.0145-0.0185 $\frac{kg}{m^3}$. The vehicle is controlled using both upper and lower slant disks which provides both collective and cyclic control of 22 deg and $\pm$ 10 deg for each rotor, respectively [12]. Differential collective is used to achieve yaw control while keeping the rotor speed constant.

Figure 1.4 shows a CAD model of Ingenuity and *Table 1.2* shows vehicle characteristics of Ingenuity.

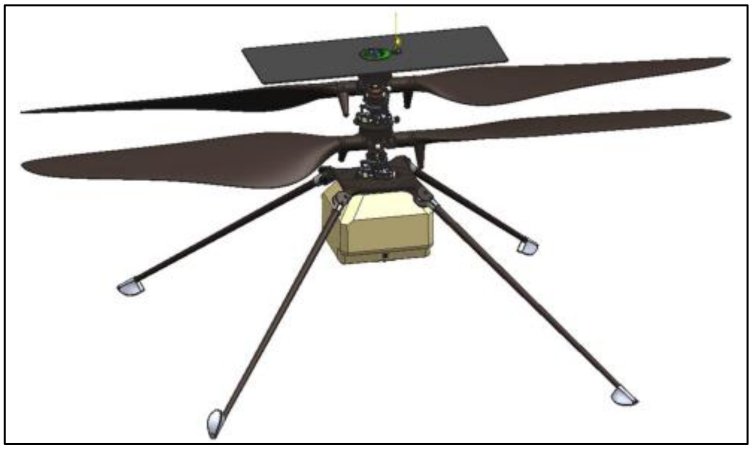

Figure 1.4: Mars Helicopter or Ingenuity [12].

Table 1.2**:** Ingenuity specifications [12]

Parameter	Value
Total Mass	1.8 kg
Rotor Diameter	1.21 m
Rotor Spacing	0.1 m
Ground Clearance (lower Rotor)	0.3 m
Landing gear footprint	0.6 X 0.6 m
Thrust-Weight ratio	135 to 155%
Endurance	$\geq 1.5 min$
Rotor Speed	$\leq 2800\, rpm$
Collective control (both rotors)	-4.5 to 17.5 deg
Cyclic control (both rotors)	$\pm 10\, deg$

Furthermore, Ingenuity is designed to fly in conditions with wind speed limited to 9 $\mathrm{m/s}$ horizontally and 2 $\mathrm{m/s}$ vertically. The design also compensates for 3.5 $\mathrm{m/s}$ of gust and limits ground, climb/descent airspeed to 10 $\mathrm{m/s}$ horizontally and 3.5$\mathrm{m/s}$ vertically, thus limiting horizontal advance ratio to 0.07 [12]. The vehicle is battery powered and can provide 90 s of flight time per charge. Rechargeable batteries via a solar panel are mounted above the upper rotor. The vehicle can conduct mission/flights based on the flight plan uploaded from the ground. Due to delays in communication between Earth and Mars, the vehicle is required to be fully autonomous. To meet the above requirement, a camera looking downward, a laser rangefinder, and an inclinometer work together to provide onboard navigation for the vehicle. Ref [13] and [14] describes the guidance, and navigation system of Ingenuity.

1.2.2. Challenges of Flying on Mars

Flying on Mars constitutes a set of challenges and requirements. The challenges are imposed due to the Martian atmosphere being very different when compared to Earth's atmosphere. Unlike Earth's atmosphere, 95.32 % of Martian atmosphere is composed of carbon di-oxide and 4.68% is composed of gasses like argon, oxygen, carbon monoxide, water, and trace gasses [15]. Moreover, Mars experiences temperature “range from -140 degrees C at the poles to up to 30 degrees C on the equator during daytime and as low as -80 degrees C at night” [16] . Besides the high variance in temperature, Mars’ atmosphere is also very different from Earth’s in numerous other ways. For example, the Martian atmosphere differs in atmospheric composition, density, and gravitational acceleration. The pressure on Mars averages 6.36 millibars which is 0.6% to the Earths atmospheric pressure [15]. With the change in pressure the air density at Mars also reduces to 0.02 $\frac{kg}{m^2}$. Mars gravitational acceleration is about one-third of Earth’s gravitational acceleration [15]. Lower gravitational pull-on Mars, while helpful, does not nearly make up for the reduced lift due to other atmospheric conditions.

To overcome the challenges, rotors operating on Mars should have a larger surface area and/or should rotate at a higher speed than they would in Earth’s atmosphere. However, rotors also have an upper bound limitation to them due to having a requirement of not exceeding rotor tip speed [15]. Specifically, it is required that the rotor tip speed should stay below 0.8 Mach, due to the speed of sound on Mars only being 240 m/s. The lower speed of sound results in increased drag and loss in lift when the rotor tip speed exceeds 200 m/s [17].

1.2.3. Flight Dynamics

When compared to the flight dynamics of stationary airfoils relative to its body frame, helicopter flight dynamics are complicated due to having rotating airfoils relative to the body frame. Periodic forces and moments are produced due to control inputs or environmental disturbances. Blade flapping is introduced which differs in important ways from helicopters operating on Earth.

1.2.4. Blade Flapping

To understand blade flapping on Mars, a simpler model of rod rotating about a hinge is considered. Figure 1.5 shows an illustration of blade model being considered.

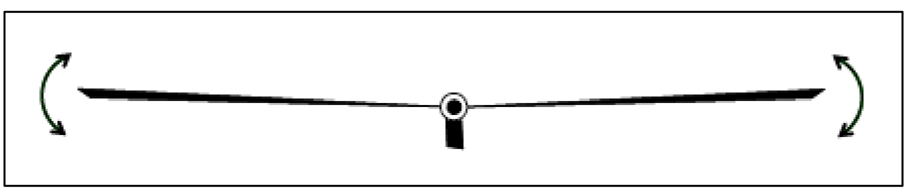

Figure 1.5: Blade flapping model [2]

The model shown in Figure 1.5 acts as a classical mass spring-damper system. Centrifugal and structural stiffening creates a restoring moment on the hinge. Damping is present due to the available aerodynamic forces. When cyclic pitch is applied to a helicopter blade, a periodic change in lift is produced at the rotor frequency, with maximum lift on the opposite side. Given the above conditions, a blade responds like a mass spring damper; “flapping with the same frequency, but with a different phase than the input” [18].

In other words, when cyclic control is applied to a rotor, it settles into a periodic flapping motion that reaches its maximum at some point later than the maximum cyclic pitch. Roll and pitch moments are generated due to flapping of the blade. The moments produced tilts the thrust vector and creates direct hub moments [2]. The blue line in Figure 1.6 shows the magnitude and phase response of a centrally hinged blade flap angle response to blade pitch with Earth parameters. The red line is where cyclic control is applied. For the following example, the peak flap output occurs 90 ° after the peak cyclic pitch input due to rotor speed coinciding with the natural frequency of the mass spring damper. Specifically, a peaking cyclic input applied on the right-hand side of the vehicle will result in a nose up moment. The green line shows the response of the same blade in Mars density. Change in response is noticed due to reduced aerodynamic damping. In Mars' atmosphere the phase angle drops to near-zero if the rotor is stiffened to increase the natural frequency, described in detail below.

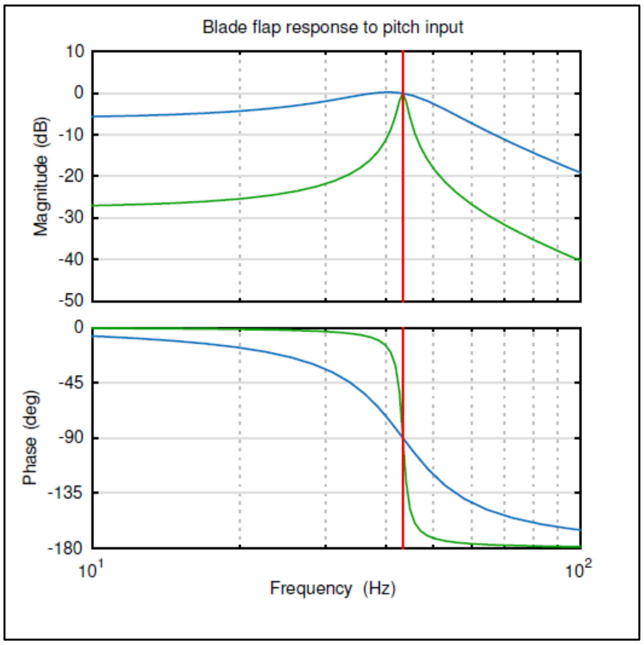

Figure 1.6: Magnitude and phase response of a blade to pitch input [18]

1.2.5. Aerodynamic Damping

The flapping motion of the blade changes the angle of attack. The flapping is typically aerodynamic and is a function of flap rate; thus, resulting in change in lift opposing the flap rate. The equation 1.1 calculates the nondimensionalized damping of a blade that is hinged centrally and has straight chord along with standard linear lift model.

$$\zeta = \frac{\Upsilon}{16\ \omega_o} \tag{1.1}$$

ω_o is nondimensionalized flap frequency, Υ is the ratio of aerodynamic to inertial forces, which is given by

$$\Upsilon = \frac{\rho c C_{l\alpha} R^4}{I} \tag{1.2}$$

ρ is the air density, c is chord length, $C_{l\alpha}$ is the lift curve slope of the blade, R is the rotor radius, and *I* is the blade inertia about flap hinge. As shown in equation 1.2, the blade Lock number depends on the density; therefore, the blade Lock number being reduced on Mars. As seen in Figure 1.6, the green line represents the reduced damping to 2% when compared to damping on Earth.

1.2.6. Effects of Flap Modes on Helicopter Dynamics

It is important to consider the overall dynamics of helicopter in its non-rotating frame. The moments generated in the non-rotating frame are a function of flap angle and the current azimuth of the blade [12]. Equation 1.3 is used to calculate the moment about a fixed axis for a blade spinning at a nondimensionalized frequency.

$$\mathrm{A}\sin(\omega_o\psi_b)\sin(\psi_b+\psi_{b0}) = \frac{1}{2}\mathrm{A}\cos\big((\omega_o-1)\psi_b-\psi_{b0}\big)-\frac{1}{2}\mathrm{A}\cos\big((\omega_o+1)\omega_b+\omega_{b0}\big) \tag{1.3}$$

In the above equation, ψ_b is the blade azimuth, ψ_{b0} is a phase angle. The above equation illustrates the rise of two modes in the non-rotating frame from one poorly damped mode. The two modes occur at approximately (ω_o-1) and (ω_o+1), known as regressive and progressive modes [19]. Due to the fuselage being unconstrained in free flight, the modes show up as flight dynamic modes of free flying vehicle at a shifted frequency. Figure 1.7 illustrates the frequency response of a transfer function from cosine cyclic input to pitch angle for a Mars helicopter dynamics. Both regressing and advancing modes are visible in Figure 1.7 [12].

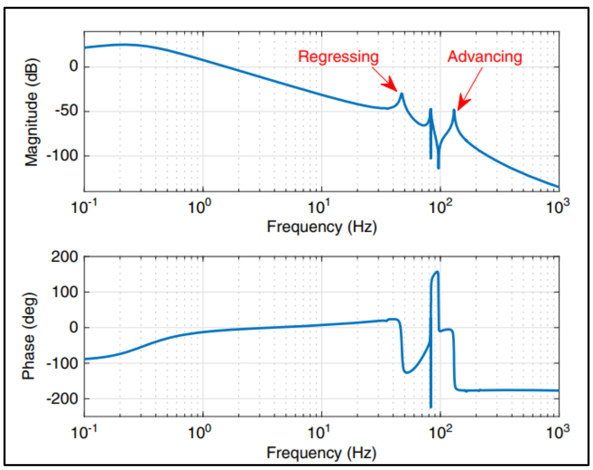

Figure 1.7: Pitch angle response to cosine cyclic Input

The modes shown in Figure 1.7 can be problematic due to them being poorly damped. Specifically, regressive mode in the system can be more problematic for flight control due to being within the range of flight control. In other words, poorly damped modes can potentially interfere with controls and can destabilize system. However, destabilize modes can be stabilized by using strategies ensuring that the phase of the mode is stabilized by confirming the control loop prevents unwanted encirclements of the critical points. Notch filters can also be employed such that the gain of the control is reduced at frequencies. Moreover, gain stabilizing the modes ensures the gains of the control loop rolls off well in advance of the modes [18].

Strategies like stabilizing modes by ensuring that the control loop is preventing unwanted encirclements and applying notch fillers assumes that the dynamics will never change which is not justified in Mars environment. When bending is coupled with flap dynamics it complicates the modes shows in Figure 1.7. The system also needs to account for gusty conditions on Mars. To meet Mars' flying conditions, the vehicle should be constructed in such a way that its mechanical design moves resonant modes to high frequencies. For instance, the blade and hub of a vehicle operating in Mars' atmospheric condition should be stiff, with a rotating flap frequency of approximately 80-90 Hz [18].

1.3.Projective Objective

The above limitations and challenges put a greater reliance on analysis, modeling and simulation due to not being able to fully replicate Mars environment on Earth [2]. This project will compare flight dynamics of a hexacopter in hover state using FLIGHTLAB in both Earths and Mars' atmospheric conditions. The comparison will allow a better understanding of the flight behavior differences of a hexacopter between the two environments. The analysis can potentially help determine if a dynamically matched surrogate helicopter to conduct flight testing on Earth can be designed. Furthermore, FLIGHTLAB is a complete flight simulation tool that will allow NASA to execute full-mission flight control simulations which is not achievable with any other NASA owned computational tools.

1.4.Methodology

FLIGHTLAB is a finite element, multi-body, selective fidelity modeling and analysis software package used to simulate rotorcraft, fixed wing aircraft, compound aircraft, drones and experimental aircraft configurations [20]. FLIGHTLAB allows its users to generate run-time models for real time applications in their own choice of environment. Using FLIGHTLAB, a hexacopter will be modelled and simulated in both Earths and Mars' environment. The modelled hexacopter will used geometry and rotors designed by NASA's Jet Propulsion Laboratory and NASA Ames Research Center for their Mars Science Helicopter [21], which are configured to Mars' environment. This project will replicate the model of a hexacopter previously created in NDARC by NASA Ames Research Center. Once the model is replicated in FLIGHTLAB, eigenvalues and flight behavior will be observed for the same model operating under Earths and Mars's atmosphere to understand the behavior of a hexacopter. The FLIGHTLAB model will be validated by comparing it to the hexacopter model simulated in CAMRAD II by NASA Ames Research Center.

Chapter 2. Kinematic Components

FLIGHTLAB is a finite element, multi-body, selective fidelity modeling and analysis software package used to simulate rotorcraft, fixed wing aircraft, compound aircraft, drones, and experimental aircraft configurations [20]. In other word, FLIGHTLAB allows its users to build each component of the desired configuration separately and later model the full vehicle altogether by combining each component together.

When creating and solving a model in FLIGHTLAB, the model is instanced into four components, i.e., structural components, aerodynamic components, control components, and solution components [22]. Structural components consist of "parent" and "child" nodes which emphasizes the relationship of precedent versus antecedent among the nodes. For instance, a flap hinge may be a structural component. A hinge connecting the flap hinge to the hub may be the parent of the flap hinge, and another offset connecting the hinge to a bearing may be the child [22]. Structural components use Motion Solution Method which passes the motion and Force Solution Method which transfers forces from the child to the parent node or vice versa. Newton Raphson Method is used to zero out any imbalance forces transferred between the components. Moreover, blade element and finite element method can be used to model the structural components. For example, a hingeless rotor can be modeled using finite element. Airloads can also be calculated based on if the flow is linear unsteady, quasi-steady, nonlinear unsteady or due to any dynamic stall. Furthermore, aerodynamic interference between each component can also be computed. For example, dynamic stall can be computed which is coupled with blade dynamics. In other words, a sudden change is airfoil motion and can cause stall a rotor dynamically and response can be modeled in FLIGHTLAB [22].

The Control components constitutes of gains, state space models, limiters, transfer functions, and pure time delays. Initial pilot commands can also be inputted along with longitudinal, lateral, collective, and pedal travel range.

The Solution components includes interaction of all four components which generates continuous equations of all four components equations, difference equations are generated that relates functions and derivatives of all components together. All current states are solved, and an output is propagated, and integrate to the next time step. The interaction between each component takes place every time step to get the most accurate result [22]. Figure 2.1 depicts the solution process followed in FLIGHTLAB.

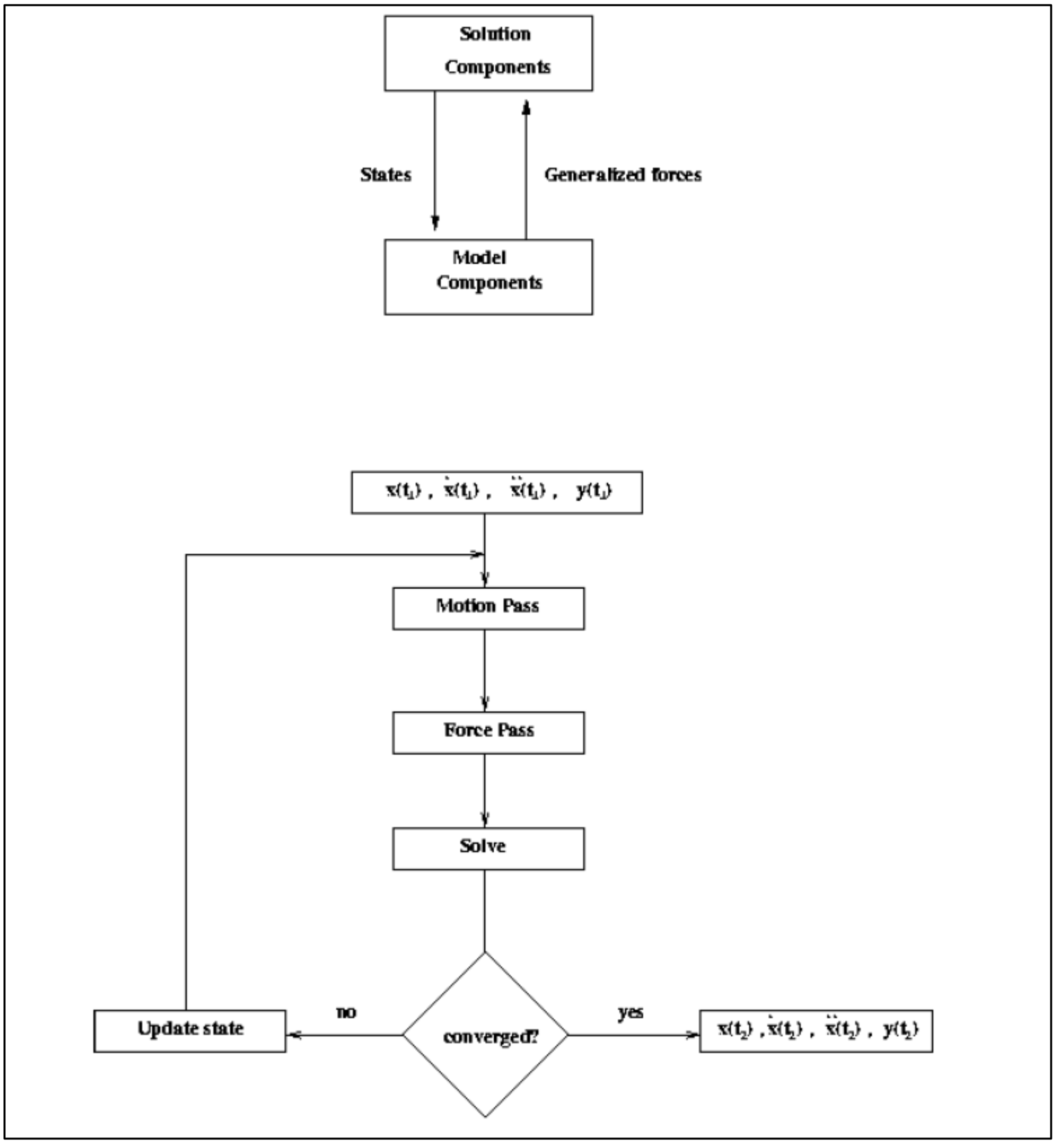

Figure 2.1: FLIGHTLAB solution flow chart *[22]*

FLIGHTLAB also follows the process shown in Figure 2.1 to account for any cross coupling. For instance, the fuselage forces can be solved for first, with the hub forces then being used to solve for the rotor forces. Iterations between these quantities are then performed until the solution converges.

2.1. Helicopter Governing Equations

2.1.1. Reference Frames

As mentioned previously, FLIGHTLAB uses parent and child nodes to describe the relationship within one component. The parent and child node analogy are used in describing the coordinate system and frames of references. A parent frame of component is a reference frame that is attached to a component at the point of connection to its parent. A coordinate system is associated with the parent frame. Likewise, a child frame of a component is a frame attached to the component at the point of connection to its child. The motion of a child frame is the sum of the motion of the parent frame and the motion of the child frame relative to the parent frame. Equations 2.1-2.3 describes the translation motion of the child frame.

$$r^{i}_{\frac{c}{i}} = r^{i}_{\frac{p}{i}} + T^{T}_{\frac{p}{i}} * r^{p}_{\frac{c}{p}} \tag{2.1}$$

$$v^{c}_{\frac{c}{i}} = v^{p}_{\frac{p}{i}} + w^{p}_{\frac{p}{i}} * r^{p}_{\frac{c}{p}} \tag{2.2}$$

$$a^{c}_{\frac{c}{i}} = a^{p}_{\frac{p}{i}} + w'^{p}_{\frac{p}{i}} * r^{p}_{\frac{c}{p}} + w^{p}_{\frac{p}{i}} * \left(w^{p}_{\frac{p}{i}} * r^{p}_{\frac{c}{p}} \right) \tag{2.3}$$

Where,

- $r^{i}_{c/i}$ is the displacement vector of the child frame with respect to the parent frame expressed in the inertial coordinate system.
- $T^{T}_{p/i}$ is the transformation matrix from inertial coordinate system to parent coordinate system.
- $v^{c}_{c/i}$ is the translation velocity vector of the child frame with respect to the initial frame expressed in the child coordinate system.
- $w^{p}_{p/i}$ is the angular velocity vector of parent frame with respect to the inertial frame expressed in the parent coordinate system.
- $a^{c}_{c/i}$ is the translation acceleration vector of child frame with respect to the inertial frame expressed in the child coordinate system.
- $w'^{p}_{p/i}$ is the angular acceleration vector of the parent frame with respect to the inertial frame expressed in the parent coordinate system.

Fixed rotation of component can also be modeled in FLIGHTLAB. Specifically, the connection between two physical components where they are rigidly linked at an angle can be modeled. The motion of child frame is computed given the absolute motion of the parent frame. The axis of rotation and angle of rotation (α) is needed to compute the motion of child frame.

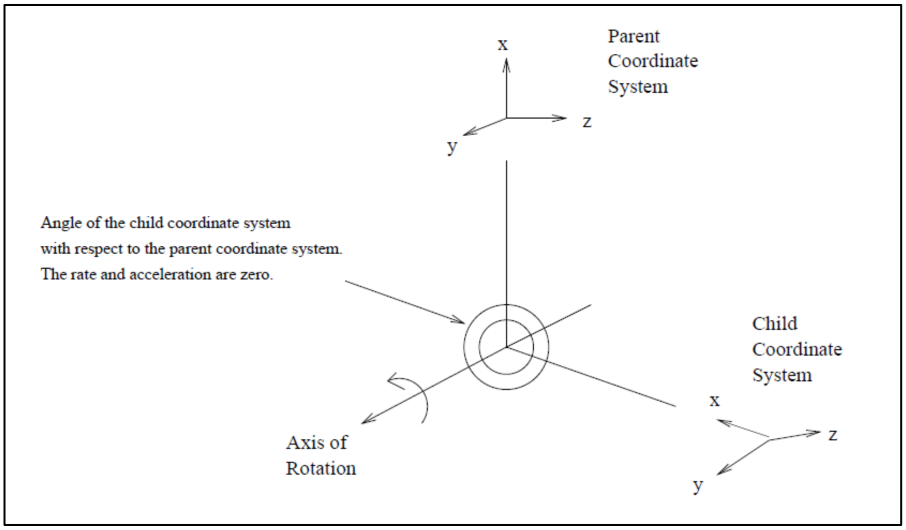

Figure 2.2: A constant rotation about single axis *[22]*

Figure 2.2 shows the coordinate system of both child and parent frames and y-axis as the axis of rotation. To compute the motion of the child frame with respect to the parent frame, a transformation matrix is formed that transforms the motion from the parent coordinate to the child coordinate system. A transformation with y-axis of rotation is presented $\left(T_{\frac{c}{p}}\right)$.

$$T_{\frac{c}{p}} = \begin{bmatrix} \cos\alpha & \sin\alpha & 0 \\ -\sin\alpha & \cos\alpha & 0 \\ 0 & 0 & 1 \end{bmatrix} \qquad 2.4$$

The angular velocity and acceleration of the child frame are computed as follows.

$$w_{\frac{c}{i}}^{c} = T_{\frac{c}{p}} * w_{\frac{p}{i}}^{p} \qquad 2.5$$

$$w_{\frac{c}{i}}^{\prime c} = T_{\frac{c}{p}} * w_{\frac{p}{i}}^{\prime p} \qquad 2.6$$

From the above equations, the translation motion of the child frame can be computed with respect to the inertial coordinate system.

$$r_{\frac{c}{i}}^{i} = r_{\frac{p}{i}}^{i} \qquad 2.7$$

$$v_{\frac{c}{i}}^{c} = T_{\frac{c}{p}} * v_{\frac{p}{i}}^{p} \qquad 2.8$$

$$a^{c}_{\frac{c}{i}} = T_{\frac{c}{p}} * a^{p}_{\frac{p}{i}} \qquad 2.9$$

2.1.2. Euler Angles

Euler Angles are used to create transformation from one coordinate system to another. Specifically, Euler angles are used to transform vector quantities from inertial coordinate system to the body coordinate. (γ, ϕ, θ) are transformation angles about x, y, and z axes of the body reference frame. The transformation matrix is shown below.

$$T_{\frac{p}{i}} = \begin{bmatrix} cos\gamma\, cos\theta & sin\gamma\, cos\theta & -sin\theta \\ -sin\,\gamma\, cos\varphi + cos\,\gamma\, sin\theta\, sin\varphi & cos\gamma\, cos\varphi + sin\gamma\, sin\theta\, sin\varphi & cos\theta\, sin\varphi \\ sin\gamma\, sin\,\varphi + cos\gamma\, sin\theta\, cos\varphi & -cos\gamma\, sin\varphi + \; sin\gamma\, sin\theta\, cos\varphi & cos\theta\, cos\varphi \end{bmatrix} \qquad 2.10$$

Euler angles are defined as follow:

$$\theta = \text{asin}\left(-T_{\frac{p}{i}}(1,3)\right) \qquad 2.11$$

$$\phi = \text{atan2}\left(\frac{T_{\frac{p}{i}}(2,3)}{\frac{p}{i}(3,3)}\right) \qquad 2.12$$

$$\gamma = \text{atan2}\left(\frac{T_{\frac{p}{i}}(1,2)}{T_{\frac{p}{i}}(1,1)}\right) \qquad 2.13$$

In above equation 2.11, (1,3) represents the quantity in row one, third column from the transformation matrix $T_{\frac{p}{i}}$. The Euler rates are defined as follow:

$$\gamma' = \gamma_i - \gamma_{(i-1)} \qquad 2.14$$

$$\theta' = \frac{\theta_i - \theta_{(i-1)}}{dt} \qquad 2.15$$

$$\phi' = \frac{\phi_i - \phi_{(i-1)}}{dt} \qquad 2.16$$

In equations 2.14-2.33, *i* stands for the *ith* time step. Equations 2.11-2.33 are used to calculate the body axis rotational rates (p, q, and r). The body axis rotational rates are expressed below.

$$p = \phi' - \gamma' sin\theta \qquad 2.17$$

$$q = \theta' \cos\phi + \gamma' \cos\theta \sin\phi \quad 2.18$$

$$r = \gamma' cos\theta cos\phi - \theta' sin\,\phi \quad 2.19$$

2.2. Fuselage

FLIGHTLAB uses the method of motion and force to model physical systems. The motion method computes the motion of the child frame, given the motion of the parent frame and the current states of the system. Force methods compute the loads produced by force producing components such as masses and aerodynamics. The forces are summed and transformed to parent frames [22]. The same method is used to compute the motion and the generalized forces of a rigid fuselage which consists of six degrees of freedom. Here the fuselage is modeled as the distributed mass component that does not have an explicit parent. The inertial reference frame is its implicit parent, and it also consists of multiple children. For example, the *Translate* component is the child component attached to the distributed mass. The *Translate* component is used to model the rigid link between the rotor and the fuselage. In addition, a fuselage can also be model as rigid fuselage with nonlinear 6 DOF's, as constrained rigid body, as modal elastic fuselage, and as elastic fuselage with phase out.

The component is associated with three body translation velocities and three body angular velocities. All six body frame degrees of freedom are with respect to the inertial reference frame expressed in the child coordinate system. The three body translation velocities and their time derivatives are defined as,

$$v_{\underset{\bar{i}}{c}}^{c} = [u\ v\ w]^T \quad 2.20$$

$$v'^{c}_{\underset{\bar{i}}{c}} = [u'v'w']^T \quad 2.21$$

The three angular velocities and their derivatives are defined as,

$$w_{\underset{\bar{i}}{c}}^{c} = [p\ q\ r]^T \quad 2.22$$

$$w'^{c}_{\underset{\bar{i}}{c}} = [p'q'r']^T \quad 2.23$$

Three successive Euler angle rotations about x, y, and z are performed to transform the vector quantities from the inertial coordinate system to the child (body) coordinate system. First, γ is rotated about z-axis. Secondly, θ is rotated about y-axis and lastly, ϕ is rotated about the x-axis. The following angular velocities are obtained after performing the three transformations [22].

$$w_{\underset{\bar{i}}{c}}^{c} = \begin{bmatrix} \varphi' \\ 0 \\ 0 \end{bmatrix} + T_\varphi \begin{bmatrix} 0 \\ \theta' \\ 0 \end{bmatrix} + T_\varphi T_\theta \begin{bmatrix} 0 \\ 0 \\ \gamma' \end{bmatrix} \quad 2.24$$

The angular acceleration vector of the child frame is the derivative of the angular velocity as defined below.

$$\mathrm{w}_{\substack{\mathrm{c}\\ \bar{\mathrm{i}}}}^{\mathrm{c}} = \begin{bmatrix} \varphi'' \\ 0 \\ 0 \end{bmatrix} + \mathrm{T}_{\varphi}' \begin{bmatrix} 0 \\ \theta' \\ 0 \end{bmatrix} + \mathrm{T}_{\varphi} \begin{bmatrix} 0 \\ \theta'' \\ 0 \end{bmatrix} + \left(\mathrm{T}_{\varphi}'\mathrm{T}_{\theta} + \mathrm{T}_{\varphi}\mathrm{T}_{\theta}'\right) \begin{bmatrix} 0 \\ 0 \\ \gamma' \end{bmatrix} + T_{\varphi}T_{\theta} \begin{bmatrix} 0 \\ 0 \\ \gamma'' \end{bmatrix} \qquad 2.25$$

The above vector relates Euler angle rotational rates to the body angular velocities as defined below.

$$\gamma' = (qsin\phi + rcos\phi)cos\ \theta \qquad 2.26$$

$$\theta' = q\ cos\ \phi - r\ sin\ \phi \qquad 2.27$$

$$\phi' = \mathrm{p} + \gamma' \sin\theta \qquad 2.28$$

Given the above equations, the motion of the child frame is expressed as

$$v_{\substack{c\\ \bar{i}}}^{i} = [x'y'z']^{T} = T_{\substack{c\\ \bar{i}}}^{T} v_{\substack{c\\ \bar{i}}}^{c} \qquad 2.29$$

$$\mathrm{r}_{\substack{\mathrm{c}\\ \bar{\mathrm{i}}}}^{\mathrm{i}} = [\mathrm{x\ y\ z}]^{\mathrm{T}} = \int_{\mathrm{t}} v_{\substack{c\\ \bar{i}}}^{i}\, \mathrm{dt} \qquad 2.30$$

$$a_{\substack{c\\ \bar{i}}}^{c} = v_{\substack{c\\ \bar{i}}}^{\prime c} + w_{\substack{c\\ \bar{i}}}^{c} * v_{\substack{c\\ \bar{i}}}^{c} \qquad 2.31$$

As mentioned previously, the fuselage component can be modeled with multiple child components, however, the motion of all the children is the same and is expressed in the child coordinate system. The forces and moments transmitted from all the children at the child node are also expressed in the child coordinate system. Generalized force equations are defined below for all twelve governing equations. First, the generalized force equation of a free body is defined.

$$Q_{(1:6)} = \begin{bmatrix} F_c \\ M_c \end{bmatrix} \qquad 2.32$$

Secondly, the generalized equations for the auxiliary translational states are defined.

$$Q_{(7:9)} = T_{\substack{c\\ \bar{i}}}^{T} v_{\substack{c\\ \bar{i}}}^{c} - v_{\substack{c\\ \bar{i}}}^{i} \qquad 2.33$$

Lastly, the generalized equations for the auxiliar rotational states are defined.

2.3.Rotor

The blade element model is used to compute the thrust and torque produced by rotors. Entire rotor performance and forces are calculate using blade element theory. The forces on a rotor are caused by the moment of rotor through air. Furthermore, blade element theory is also known as lifting line theory. The solution of lifting line theory requires an estimation of induced velocity at the rotor disk. The wake induced velocity is computed using momentum theory, vortex theory or non-uniform inflow calculations. Blade element theory is important as it helps analyzes rotor aerodynamics which includes blade loading and relates rotor performance parameters and other characteristics to various design parameters. Rotor performance with non-uniform inflow can be obtained by using equation 2.34. Equation 2.34 is used to calculate thrust produced by N number of blades. computes fan thrust using blade element formulation.

$$\mathrm{d}C_T = \frac{\sigma a}{2}\left(\theta - \frac{\lambda}{r}\right) r^2 dr \qquad 2.34$$

In the above equation, C_T is the thrust coefficient, a is defined as the slope lift curve, θ is the blade collective pitch, r is rotor radial station, dr is width of the blade, λ is the inflow ratio. the, and σ is the rotor solidity. Equation 2.35 and 2.36 describes rotor solidity and non-uniform inflow respectively.

$$\sigma = \frac{\mathrm{bc}}{\pi\,\mathrm{R}} \qquad 2.35$$

$$\lambda = \sqrt{\left(\frac{\sigma a}{16} - \frac{\lambda_c}{2}\right)^2} + \sqrt{\frac{\sigma a}{8}\theta r} - \left(\frac{\sigma a}{16} - \frac{\lambda_c}{2}\right) \qquad 2.36$$

In hover condition, $\lambda_c = 0$. With blade element formulation, the rotor model consists of rotor dynamic degree of freedom for each individual blade, either rigid or elastic. A rotor blade is divided into many segments. Airloads are computed with respect to the local angle of attack and Mach number. From there, blade dynamic response is calculated for any non-uniform blade inertial and aerodynamic properties. FLIGHTLAB uses blade element model that consists of models for blade structure, airloads, and induced flow. Euler angles are used to define the orientation of rotor shaft. For example, Phi describes rotation about x-axis, Theta is defined as rotation about y-axis, and Psi is defined as the rotation about z-axis. It is necessary to define the rotation in the right order, such that the desired orientation of the shaft is obtained.

FLIGHTLAB also includes electric model option to model eVtol modeling. For instance, DC motor voltage can be defined by the interface variables. Like voltage, torque option is also provided as an input to the DC model motor. The torque option is also defined by the interface variables.

2.3.1. Blade Structure

FLIGHTLAB allows its users to model blade element model as both rigid and elastic blades for hub configurations such as articulated, hingeless, teetering, and gimballed. Elastic beam is modeled by the modal approach. The absolute motion of all the nodes on modal beam is computed by generalizing coordinates (q) and mode shape (ϕ). The linear displacement along the x-axis is computed bases on the assumption of axial displacement between nodes along the beam remains constant. Thus, using geometric constraints to compute the motion along the x-axis and then computing the axial displacement. Figure *2.3* shows the geometry of two frames, j-1 and j along the elastic beam. Delta in Figure *2.3* denotes the relative motion of the second frame j, with respect to j-1. Whereas equation 2.37 is the relative deflection along the x-axis. Equation 2.37 is differentiated twice to obtain both velocity and acceleration along x-axis.

$$\Delta x_j = \sqrt{l_j^2 - \Delta y_j^2 - \Delta z_j^2} \qquad 2.37$$

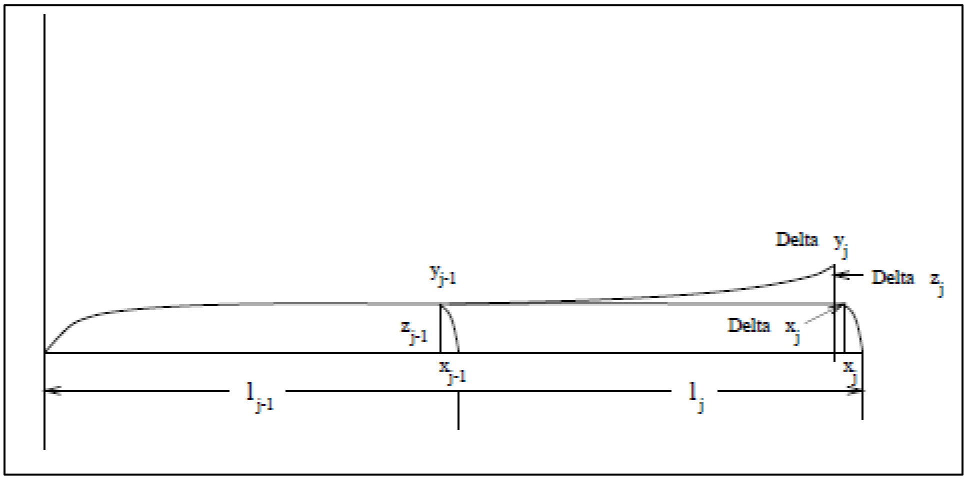

Figure 2.3:Elastic beam described by mode shapes *[22]*

2.3.2. Quasi-Steady Airloads

Two-dimensional quasi-steady aerodynamic theory is used to compute wing/blade segment airloads with respect to angle of attack and Mach number. Lift and drag are computed in terms of air velocity.

$$L = \frac{\rho}{2} U^2 c\{a(\theta - \phi_a) + c_0\} \qquad 2.38$$

$$D = \frac{\rho}{2} U^2 c c_{d0} \qquad 2.39$$

In the above equations, a is lift slope, c_0 is the lift at zero angle of attack, c is the chord length, θ is the blade pitch angle, ϕ_a is the aerodynamically induced angle which is simplified by a small angle assumption so that the angle $\phi_a \cong \frac{Up}{UT}$, and L and D are lift and drag per unit length. The total wind velocity in the blade undeformed coordinate system is defined as following.

$$U = \sqrt{U_T^2 + U_p^2} \cong U_T \qquad 2.40$$

U_T, U_P are the tangential, normal component respectively. The nondimensionalized aerodynamic forces on an arbitrary blade section are expressed as

$$\widehat{FA_x^b} \cong -\frac{\beta}{2}(U_T^2\theta - U_P U_T) - \frac{cd_0}{2a} U_R U_T \qquad 2.41$$

$$\widehat{FA_y^b} \cong -\frac{1}{2}(U_P U_T\theta - U_P^2) - \frac{cd_0}{2a} U_T^2 \qquad 2.42$$

$$\widehat{FA_z^b} \cong \frac{1}{2}(U_T^2\theta - U_P U_T) - \frac{c_0}{2a} U_T^2 \qquad 2.43$$

Where,

$$\mathrm{UP} = \lambda + \mathrm{x}\dot{\beta} + \beta\mu\cos\varphi \qquad 2.44$$

$$U_T = x + \mu_x \sin\varphi \qquad 2.45$$

$$\mathrm{U_R} = \mu_\mathrm{x}\cos\varphi \qquad 2.46$$

$$\tilde{\theta} = \theta_{\mathrm{con}} + \theta_{0.75} + \theta_{\mathrm{tw}}(\mathrm{x} - 0.75) \qquad 2.47$$

$$\theta = \tilde{\theta} - \beta\tan\delta_3 \qquad 2.48$$

$$\dot{\beta} = \mathrm{d}\beta/\mathrm{d}\varphi \qquad 2.49$$

In the above set of equations x is the blade station nondimensionalized with the blade radius, μ_x is the longitudinal advance ratio in the auxiliary hub frame, and $\varphi = \Omega t$ and $\theta_{0.75}$ is the twist angle at 75% span. θ_{con} is pitch control, and δ_3 pitch flap coupling factor.

2.3.3. Quasi-Unsteady Airloads

During forward flight, helicopters encounter several aerodynamic problems which leads to time variant aerodynamic loads. These forces and moments should be analyzed when conducting rotor analysis. FLIGHTLAB uses Leishman-Beddos dynamic model to provide a relative complete physical representation of the overall unsteady aerodynamic problem, while keeping the analysis within the bounds of computational tractability. Unsteady aerodynamics consists of both attached and separated flow effects. The attached flow consists of lift generated by circulation in the wake caused by vortex shedding. The lift around the airfoil reduces due to the decrease in circulation around the airfoil. The separated flow consists of the change in lift due to a phenomenon known as dynamic stall of an airfoil. Indicial function with four constants is used to predict the lift generated by unsteady attached flow. An impulsive force is added due to flow circulation caused by the separation of the flow. The vortex lift is also modeled which is generated due to vortex propagating over an airfoil.

When flow is attached, the unsteady linear normal force coefficient is the sum of the circulatory and non-circulatory components as shown below.

$$\mathrm{C_n^P} = \mathrm{C_n^c} + \mathrm{C_{n\alpha}^i} + \mathrm{C_{nq}^i} \qquad 2.50$$

In the above equation, C_n^c is unsteady circulatory normal force coefficient, α denotes step input in angle of attack, and q is step change in non-dimensional pitch rate. C_n^c is given by

$$\mathrm{C_n^c} = \mathrm{C_{n\alpha}}(M)\phi_{n_\alpha}^c(\alpha + \frac{q}{2}) \qquad 2.51$$

$$\phi_{n\alpha}^c = 1 - \mathrm{A_1 e}^{-b_1\beta^2 S} - \mathrm{A_2}e^{-b_2\beta^2 S} \qquad 2.52$$

$A_1, B_1, A_2, and\ B_2$ are values proposed by Leishman and Beddos as shown in Table 2.1. β equals $\sqrt{1-M^2}$ and S represents the distance traveled by the airfoil section in semi-chords.

Table 2.1**:** Leishman and Beddoes coefficients

Parameter	Value
A_1	0.3
B_1	0.14
A_2	0.7
B_2	0.53

A state space representation shows below is obtained by carrying out the Laplace transform.

$$\begin{bmatrix} \dot{x_1} \\ \dot{x_2} \end{bmatrix} = \frac{2U}{c}\beta^2 \begin{bmatrix} -b_1 & \\ & -b_2 \end{bmatrix} \begin{bmatrix} x_1 \\ x_2 \end{bmatrix} + \begin{bmatrix} 1 \\ 1 \end{bmatrix} \alpha_{\frac{3}{4}} \qquad 2.53$$

$$C_n^c = C_{n_\alpha}(M)\left(\frac{2U}{c}\right)\beta^2 [A_1 b_1 \quad A_2 b_2] \begin{bmatrix} x_1 \\ x_2 \end{bmatrix} \qquad 2.54$$

Similarly, $C_{n_\alpha}^i$and $C_{n_q}^i$is described as following. A detailed explanation is provided in FLIGHTLAB Theory Manual [23].

$$\begin{bmatrix} \dot{x_3} \\ \dot{x_4} \end{bmatrix} = \begin{bmatrix} -\frac{1}{K_\alpha T_1} & \\ & -\frac{1}{K_q T_1} \end{bmatrix} \begin{bmatrix} x_3 \\ x_4 \end{bmatrix} + \begin{bmatrix} 1 & \\ & 1 \end{bmatrix} \begin{bmatrix} \alpha \\ q \end{bmatrix} \qquad 2.55$$

$$\begin{bmatrix} C_{n_\alpha}^i \\ C_{n_q}^i \end{bmatrix} = \begin{bmatrix} \frac{4}{M} & \\ & \frac{1}{M} \end{bmatrix} \begin{bmatrix} \dot{x_3} \\ \dot{x_4} \end{bmatrix} \qquad 2.56$$

A very similar process is followed to derive unsteady pitching moment coefficient under the attached flow conditions which is described in ref [23]. In the separated unsteady flow model in FLIGHTLAB, leading edge separation is identified by using critical normal force coefficient. Lag is present in the leading-edge pressure due to circulation around the airfoil changing and its effect not being instantaneous. To compensate for this effect, a first order lag is applied to the normal force to obtain critical normal force coefficient. Likewise, trailing edge separation effect is also modeled. The flow separates at the trailing edge of an airfoil due to pressure distribution and boundary layer reaction. To model the nonlinear forces and moments under trailing edge separation, Kirchhoff theory is implemented that uses the equation used to model lift on a flat plate. First, the flow separation point is computed under the assumption that there is time lag between dynamic flow separation and the flow separation due to unsteady pressure on an airfoil. The separation point is determined as a function of angle of attack. The angle of attack is obtained by considering time lag in unsteady attached flow lift. The time lag is also factored in when deriving the deficiency function that uses time constant parameters to provide different flow interaction features at each time step. The nonlinear force coefficient that incorporates trailing edge separation is given by

$$\mathrm{C}_{\mathrm{N}_{\mathrm{n}}}^{\mathrm{f}} = \mathrm{C}_{\mathrm{Nn}}^{\mathrm{fC}} + \mathrm{C}_{\mathrm{Nn}}^{i} \tag{2.57}$$

Where, C_{Nn}^{fC} is the separation flow effect which equals

$$\mathrm{C}_{\mathrm{Nn}}^{\mathrm{fC}} = \mathrm{K}_{\mathrm{Nn}}\mathrm{C}_{\mathrm{Nn}}^{\mathrm{C}} \tag{2.58}$$

$$\mathrm{K}_{\mathrm{Nn}} = \frac{\left(1+\sqrt{\mathrm{f}_{\mathrm{n}}''}\right)^2}{4} \tag{2.59}$$

In equation 2.59, f'' is the trailing edge separation point. The derivation of separation point is covered in ref [24].

Furthermore, the aerodynamic airloads are also modeled in the presence of vortex effects. when a vortex is formed over the surface of an airfoil, the flow separates at the leading edge of an airfoil. The propagation of vortex results in increase of lift produced by an airfoil and is modeled using the difference between the lift produced by circulatory attached flow and the lift produced by flow separation at the trailing edge [23].

2.4. Solution Methods

FLIGHTLAB lets its users perform trim, run the model to steady state or static equilibrium, linearize the model, or perform a quasi-static reduction, eigen analysis, time and/or frequency response, or parameter sweep. A model can also be linearized after obtaining static equilibrium solution. In other words, the nonlinear model should contain its appropriate initial conditions that ensures steady state flight conditions.

2.4.1. Trim

The steady state flight condition is also referred to as trim condition of a model in which all forces and moments in the fixed body frame are constant or set to zero.

The above process is accomplished using Newton Raphson method. The Newton Raphson method is an iterative process that finds the root of an equation by linear approximation. In other words, a nonlinear function is approximated by a linear function tangent to it. Figure 2.4 shows a geometric interpretation of the Newton-Raphson method.

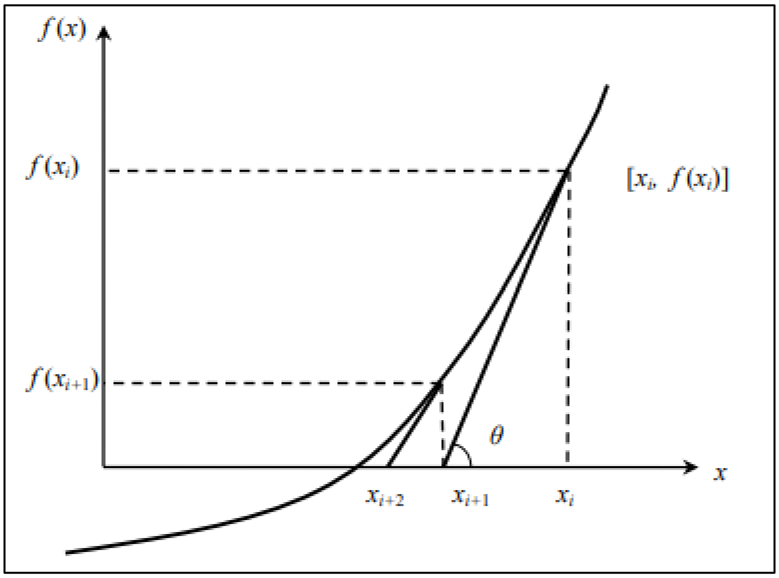

Figure 2.4: Newton Raphson method illustration *[32]*

The above figure illustrates the principal of linear approximation. x_i is the initial root guess of nonlinear function $f(x) = 0$. The Newton Raphson method approximates an improved estimate of the root through fitting a tangent line to the curve at point x_i. The point of intersection where the tangent intersects x-axis is the improved estimate of the root i.e. x_{i+1}. The process is iterated until the desired root is obtained. For example, a generalized force is set equal to nonlinear equations i.e., equation 2.60.

$$\begin{gathered} \mathrm{Q} = \mathrm{f}(\ddot{x}, \dot{x}, x, u) = 0 \\ \mathrm{y} = \mathrm{g}(x, \dot{x}, \ddot{x}, u) \end{gathered} \qquad 2.60$$

In the above equation Q is the imbalance in satisfying the differential equations. U is the inputs to the component and y represents the outputs from the component. Q is expanded by performing Taylor series expansion about initial point x_0 which results in the following.

$$\mathrm{Q} = \mathrm{Q}_0(\ddot{x_0}, \dot{x_0} x_0, u_0) + \frac{\partial \mathrm{Q}}{\partial \ddot{x}} \partial \ddot{x} + \frac{\partial \mathrm{Q}}{\partial \dot{x}} \partial \dot{x} + \frac{\partial \mathrm{Q}}{\partial \mathrm{x}} \partial \mathrm{x} \qquad 2.61$$

$$\mathrm{M}\, \partial \ddot{x} + \mathrm{C}\, \partial \dot{x} + \mathrm{K}\, \partial \mathrm{x} = -\mathrm{Q}_0 \qquad 2.62$$

Where, $M, C, and\ K$ are the mass, damping and stiffness matrices respectively and Q_0 includes all constants and higher order terms. From here, discretization in time is performed to obtain the following equation.

$$\delta \mathrm{x} = \widehat{K}^{-1} \widehat{F} \qquad 2.63$$

$\widehat{K}$ *and* $\widehat{F}$ are both known quantities and δx is the update point which can be expanded using Taylor series expansion to continue the iteration Q converges to zero. To summarize the above process, the nonlinear equations are differentiated with respect to states and are linearized. The goal in carrying out the process is to derive the generalized force equation equal to zero while satisfying the state equations.

2.4.2. Linearization

Once an equilibrium point is obtained to design a control system about a specific flight condition. For the designed hexacopter, an equilibrium point is achieved, and non-linear dynamics of the model are linearized. Furthermore, when designing a control system, Linear time-invariant model is desired as LTI models open up an option of using multiple frequency domain design and analysis tools. FLIGHTLAB uses “averaged genq” method to extract the stability, control, and output matrices. The matrices are extract by making perturbation at each rotor azimuth. The resulting perturbed generalized force is collected and then the resulting partial derivatives over one rotor revolution are averaged.

Chapter 3. Hexacopter Design

As mentioned before, planetary aerial vehicles are being envisioned to increase the distance traditional landers and rovers can travel along with having the ability to explore the surface from closer than orbiters. For the purpose of this project, a hexacopter is being considered. The hexacopter serving the project is designed and sized by NASA Ames Research Center to meet mission requirements defined by JPL.

The designed helicopter should be able to take off in 30 seconds and climb 200m above its landing site. Next, the helicopter must have a cruising range of 1km along with capability of being able to hover the science site for 2 min. Lastly, the helicopter should be able to land and sleep for 1 sol and recharge [21]. Figure 3.1 illustrates the mission requirements.

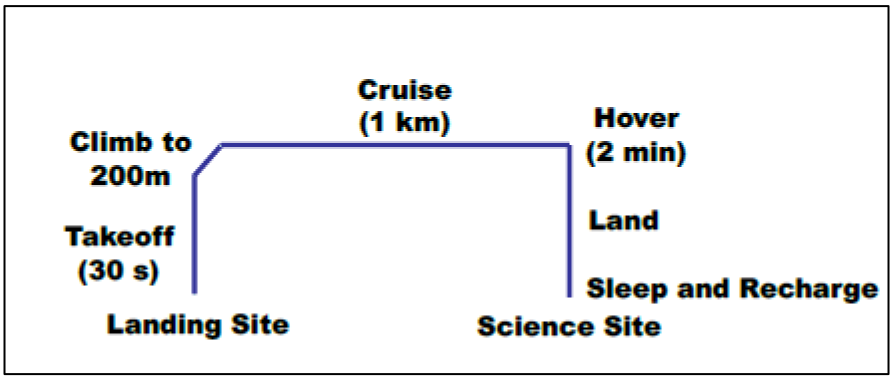

Figure 3.1: Mars Science Helicopter design mission *[21]*

3.1.Design Process

The design process of a hexacopter began with defining the mission. The mission included the amount of the payload the vehicle is required to carry, range, and its endurance. To have a reliable design, all components that make up a Hexacopter were identified along with their weight and performance. Motor and battery specifications were also identified to meet the power requirements of the payload [21].

Furthermore, the design of all Mars Helicopters is constrained to the size of the current aeroshell used to transport the vehicle from the Earth to Mars. A spreadsheet was designed by NASA Ames Research Center that sized and produced initial estimates of the design. The estimates considered sizing constraint imposed by the size of an aeroshell in which the vehicle need to be folded and packaged before being transported to Mars' surface [21]. After initial sizing, NDARC (NASA Design and Analysis of Rotorcraft) is used to develop a model of each component. NDARC, known as Conceptual/Preliminary Design and Analysis Computer Program [21] is developed by NASA Ames to quickly size and analyze performance of new concept vehicles. NDARC theory is further described in ref. [25] and is used by NASA to size concept designs such that the design can meet all mission operational flight envelope requirements. In case of a rotor design, the design produced in NDARC is iterated several times to achieve the most suitable design that provides max rotor performance along with rigid structural to minimize flapping.

3.2. Sizing

When compared to a coaxial helicopter, a hexacopter is advantageous due to it having lower disk loading which results in better performance. A hexacopter is also advantageous due to its flight dynamics characteristics. Specifically, due to having six rotors, the respective helicopter is also able to operate under four rotors if power is loss to one or two rotors. The redundancy in system makes it suitable to operate under unexpected Mars' environment. NASA used the weight and power of Ingenuity as design parameters and developed a spreadsheet to size a hexacopter for their next mission to Mars. The above design parameters were chosen to ensure the vehicle is not heavy and can at least output the same amount of power. The developed spreadsheet also used the legacy Pathfinder aeroshell as a sizing constraint which imposed a constraint of maximum rotor diameter to 2.5m for a helicopter to be folded and fit in the aeroshell [21]. The initial design was iterated several times to make model perform better.

3.2.1. Rotor Performance and Optimization

After developing the initial size of Mars helicopter the next step NASA performed was to analyze the rotor performance for the selected airfoil. Blade airloads and the power produced by the rotors were calculated by NASA to obtain the airfoil tables for the chosen airfoils. The airfoil tables which were generated after accounting how viscosity and Reynolds number affected the airfoil performance.

Mars' environment depicts about $Re = 15{,}000 - 25{,}000$ when it comes to flying in Mars's environment [21]. To obtain the best rotor performance, a circular arc airfoil was chosen by NASA as the most suitable for Mars' environment. A section of airfoil contains 5% chamber, 1% thickness which not only provides was good lift to drag ratio, also higher lift than many airfoils in Mars conditions. Figure 3.2 illustrates the circular arc airfoil section.

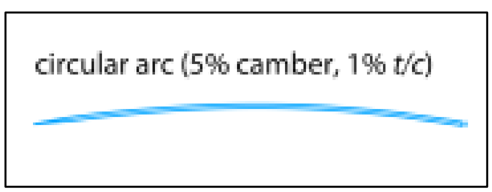

Figure 3.2: Circular arc airfoil section *[21]*

Next, NASA optimized the blade geometry to obtain the best rotor performance. Figure *3.3* shows optimized blade geometry of NASA's hexacopter model.

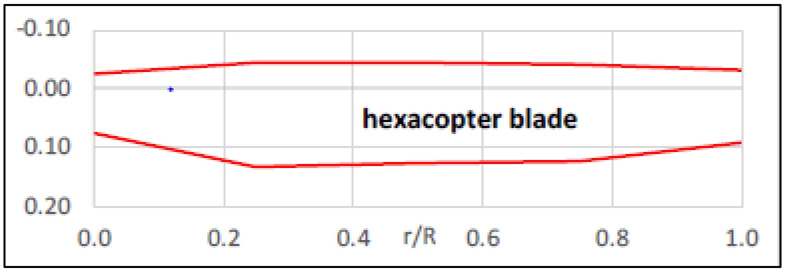

Figure 3.3: Hexacopter blade geometry *[21]*

The blade consists of a square tip such that tip vortexes can be form at the tip to provide better hover performance. As described in ref [21], the blade thrust-weight solidity is kept constant by varying the planform taper and blade twist. The figure above shows that the chord is reduced for the root. Negative taper at the root was performed to cut down the weight of the blade, since root of the blade is not necessary to achieve better performance [21].

3.3.Hexacopter Design

After optimizing the rotor blade for better performance, a hexacopter model was prepared by NASA. According to ref [21], parameters like blade loading C_T/σ and tip speed were kept as the design parameters, since increasing the tip speed resulted in reduced blade area and weight. Table 3.1 shows the design parameters of a hexacopter. As seen in the table below, the vehicle weighs 17.81 kg with rotor radius of 0.64m. Most of the parameters shown in Table 3.1 are used as design parameters which are replicated in FLIGHTLAB using structural parameters.

Table 3.1**:** Hexacopter design parameters

Parameters	**Values**
Design C_T/σ	0.115
Design M_{Tip}	0.8
Cruise speed (m/s)	30
Advancing Tip M_{at}	0.93
Payload (Kg)	2.02
Range (Km)	2
Hover Time (min)	4.5
Rotor Radius (m)	0.64
Gross weight (Kg)	17.81
Number Rotors	6
Number Blades	4

Disk Area (m^2)	7.72
Disk Loading (Kg/m^2)	2.29
Solidity	0.142
Tip Speed (m/s)	186.5
Rotor Speed (rpm)	2782
Total Power (KW)	2.80
Solar Cell (m^2)	0.62
Battery (Ah)	172
Rotor Group (kg)	3.00
Controls (kg)	1.06
Motor Weight (kg)	0.64
Battery Weight (kg)	2.31

Chapter 4. Modeling in FLIGHTLAB

In FLIGHTLAB, FLME (FLIGHTLAB Model Editor) is used to build or edit a pre-existing model. For the purpose of this project, a pre-existing model template was used to construct a hexacopter. Figure 4.1 shows a model template used to design model hexacopter. The template consists of solution parameters subsection that specifies solution parameters for the simulation. The subsection includes parameters for Newton-Raphson solution and simulation integration time. A user can set Newton-Raphson convergence tolerance value, maximum number of Newton-Raphson iterations and number of rotor azimuth step/rev.

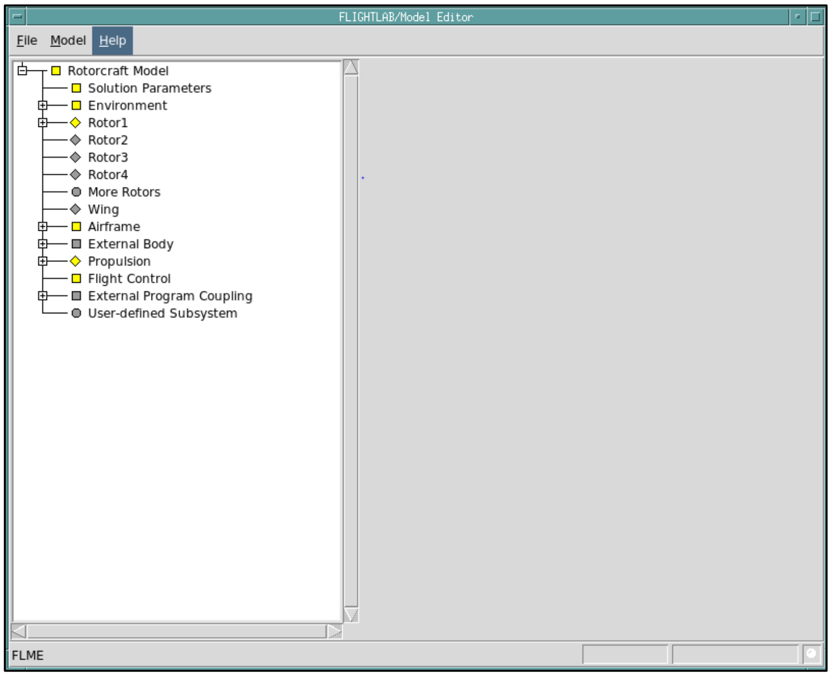

Figure 4.1: FLME model template

Furthermore, the “Environment” subsystem also lets user set the atmosphere condition for the model. The atmospheric table under the “Environment” subsystem consists of specific heat ratio, gas constant and initial latitude value. Moreover, the subsystem also consists of the following parameters.

- Altitude arguments
- Standard density table
- Standard pressure table
- Speed of sound
- Standard temperature table
- Standard temperature lapse rate table

The rotor subsystem is used to model a vehicle with one or multiple rotors. Rotor can be modeled using the following methods.

- Blade element

- Finite element
- Disk main rotor (coll/cyclic)
- Ducted fan

For the purpose of this project, blade element theory is used, and other ways of modeling rotors are described in ref [22]. Under blade element theory, the following blade structures can be modeled.

- Articulated
- Hingeless
- Teetering
- Gimballed

The hexacopter being modeled for this project uses articulated blade structure. Blades under articulated can be modeled as rigid or elastic blade. Flapping dynamics along with lead-lag dynamics of a blade can also be modeled. Blade parameters such as offsets, spring stiffness, damping coefficient, and spring angle can be set under the subsystem to model blade dynamics correctly. Blade element model divides the rotor blade into segments; thus, property table is needed to model the blade structure properly. The blade property requires the following parameters.

- Nondimensional rotor station
- Blade chord
- Blade twist
- Chordwise c.g. offset
- Blade rotary inertia distribution
- Blade flatwise inertia distribution
- Blade chordwise inertia distribution
- Blade mass distribution
- Blade midchord offset
- Blade tip sweep
- Blade tip droop

Modeling rotor airloads are optional. If no airload model is selected, a rotor structural dynamics model in vacuum is created. If there are airloads, they can be modelled using the following theories.

- Linear unsteady
- Quasi-steady
- Nonlinear unsteady
- Dynamic stall (Leishman-Beddoes)
- Dynamic stall (ONERA)

The thin airfoil theory is used to model linear unsteady airloads. Quasi-steady airloads can also be used that computes the wing/blade element airloads with respect to the angle of attack and Mach number. The above method allows for 3-D stall delay correction due to blade rotation. Unsteady airloads can also be modeled that uses combined linear airload with nonlinear look up tables [22]. The unsteady airloads option is used to model the effects of yawed flow and 3-D stall delay correction due to blade rotation. Linear airfoil modeling in a consistent manner can be used to model complicated rotor blade dynamic stall [22].

Rotor induced flow can also be modeled using the following selections.

- Glauert inflow
- Peters-He finite state wake
- Vortex wake models

All above selections can be used with blade element, finite element modeling methods. Peters-He finite model provides selective fidelity from uniform, 3-states, to high order state model. Rotor interference can also be modeled using both empirical and analytical models. Both methods are described in ref [23].

Similar to the rotor structure, the airframe structure is modeled by modeling the fuselage as rigid, elastic or as a constrained rigid body. The rigid fuselage has six nonlinear rigid body degrees of freedom. The method of modal formulation is used to model fuselage as elastic fuselage. Furthermore, spring and damper constraints are used to model fuselage as constrained rigid body. The mass and inertial properties of the airframe structure can be input as total vehicle mass/inertia or fuselage only mass/inertia.

Sensors like airframe motion, accelerometer, slip ball, and airspeed sensors can also be included. Moreover, pilot station can also be defined in the model which defines the pilot position in terms of fuselage, buttline, and waterline stations. Landing gear can also be modeled with spring/damper/friction formulation. For the purpose of this project all sensors, pilot station and landing gear were excluded from the model. Each sensor, pilot station and different types of landing gear are further described in ref [22].

Airframe aerodynamics are modeled via look up table which are with respect to angle of attack, side slip angle, and Mach number. Look up tables can either be monotonic with nonuniform increment, or uniform with low and high angle of attack division are acceptable. Airload tables can also be constructed in terms of body force/moment coefficients in body reference frame or in terms of drag, lift, side force, and moment coefficients in wind frame. Likewise, auxiliary body with inertial and aerodynamic effects can also be in included in the model if wanted [23]. Since we are modeling a hexacopter, no airframe aerodynamics along with no auxiliary body is being modeled.

To power the vehicle being modeled in FLIGHTLAB, the propulsion system of the vehicle can be modeled using the following engines.

- Ideal engine
- Simple engine
- Turboshaft engine

- Multiple turboshaft engines
- Electrical motor

Just like its terminology, ideal engine in FLIGHTLAB maintains a constant rotational speed and has no limit on power output. The simple engine includes engine governor and torque dynamics, excluding the engine thermodynamics and gas turbine dynamics. Turboshaft engines are used for turbine engine simulation. The turboshaft engine consists of engine fuel system, engine power loss, engine start/shutdown and engine malfunction. Furthermore, electric motor can also be selected with motor efficiency factor to use as the propulsion system of the selected vehicle [22].

Similar to FLME that is used to edit or build a model, CSGE (Control System Graphical Editor Manual) is used to design and build a control schematic as block diagrams. The control system constructed in CSGE editor can be integrated with FLIGHTLAB mode editor (FLME) to generate a full rotorcraft model for simulation. CSGE consists of the following element to construct a control system.

- Linear elements
- Nonlinear elements
- Matrix operations
- Discrete elements
- Logical elements

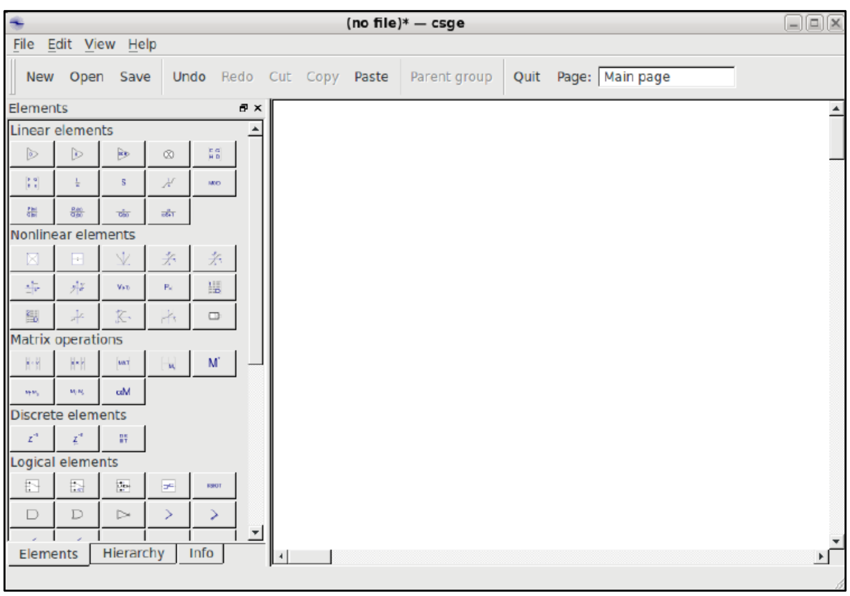

Figure 4.2: Control system graphical editor *[26]*.

Figure 4.2 shows CSGE. Once a control system is build it can be exported into .prolog, .exc, .epilog and .configure files to be integrated with FLIGHTLAB'S model editor. [26]. Once a model is successfully built in the editor, the model can be validated using the validate option from the graphical user interface. A scope model script is generated that is loaded into X-analysis. X-analysis is a user interface for the analysis of dynamic system models built in the editor. X-analysis provides a rapid tool for testing, performance, control, and stability analysis [27]. Moreover, X-analysis provides an option of visualizing a model, setting test condition and configuration. After a model is configured and test conditions have been set, the loaded model can be trimmed, check for static equilibrium, steady state analysis can also be formed. Furthermore, a model can be linearized and analysis such as eigen-analysis, model order reduction, time and frequency response analysis can also be formed. In addition, other analysis such as performance and stability, loads, handling qualities, control design, signal processing analysis can also be performed [27]. Figure 4.3 shows a model being loaded into X-analysis and ready for analysis.

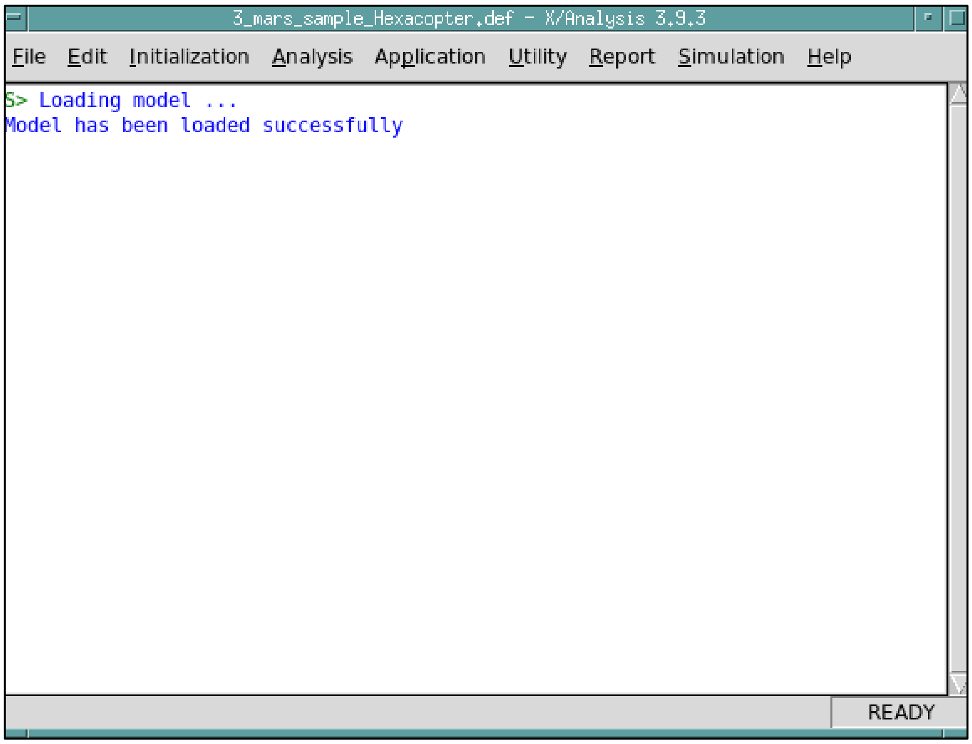

Figure 4.3: X-analysis window

Chapter 5. Configuring Hexacopter in FLME

To better understand the flight behavior differences of a hexacopter between the two environments, a hexacopter model was created in both Earth and Mars' environment.

5.1. Earth's Environment

5.1.1. Solution Parameters and Environment

Using the template described above in chapter 4, a hexacopter model in Earth atmosphere is built using the FLME editor. Table 5.1 consists of the solution parameters used to simulate a hexacopter in the Earth's atmosphere.

Table 5.1: Solution parameters

Parameter	Value
Newton-Raphson convergence tolerance	0.01
Maximum Newton-Raphson Iterations	5
Number of rotor azimuth step/rev	36

Appendix-A includes the atmospheric table used to set the test conditions to Earth's atmosphere.

5.1.2. Rotors

All six rotors of the hex are modeled with blade element theory with articulated blade structure. Like a quadcopter, an opposite pair of rotor in hex rotates in the opposite direction of each other. Each rotor model consists of four blades which are 0.64m in radius. Table 5.2 below shows other rotor parameters for all six rotors.

Table 5.2: Rotor parameters

Rotor Number	Parameter	Value
Rotor 1	Rotation Direction	CW
	Hub Orientation in Euler Angles (deg)	[0,180,0]
	Blade tip loss factor	0.97
	Rotor Nominal Speed (rpm)	507
Rotor 2	Rotation Direction	CCW
	Hub Orientation in Euler Angles (deg)	[0,180,0]
	Blade tip loss factor	0.97
	Rotor Nominal Speed (rpm)	507

Rotor 3	Rotation Direction	CW
	Hub Orientation in Euler Angles (deg)	[0,180,0]
	Blade tip loss factor	0.97
	Rotor Nominal Speed (rpm)	507
Rotor 4	Rotation Direction	CCW
	Hub Orientation in Euler Angles (deg)	[0,180,0]
	Blade tip loss factor	0.97
	Rotor Nominal Speed (rpm)	507
Rotor 5	Rotation Direction	CW
	Hub Orientation in Euler Angles (deg)	[0,180,0]
	Blade tip loss factor	0.97
	Rotor Nominal Speed (rpm)	507
Rotor 6	Rotation Direction	CCW
	Hub Orientation in Euler Angles (deg)	[0,180,0]
	Blade tip loss factor	0.97
	Rotor Nominal Speed (rpm)	507

Furthermore, each rotor blade is modeled as a rigid blade with flapping dynamics. Lead-lad dynamics are not needed for the hex. Blade flapping is a crucial aspect to include when designing a rotor as it can affect the stability and performance of a given blade. Flap response is also necessary to model such that a rigid control system can be built that can handle blade flapping in a given environment [28]. Table 5.3 describes the flapping parameters.

Table 5.3: Flapping parameters

Rotor	Parameter	Value
Rotors 1-6	Flap hinge offset (m)	0.0128
	Flap hinge spring stiffness (n-m/rad)	1410

In addition to adding flapping dynamics, blade property is defined by setting the chord, blade twist, inertia distribution and mass distribution of the blade. Blade chord is defined form 0 nondimensional rotor station to 1 rotor station in the increment of 0.25 rotor station. Whereas, blade twist, and mass distribution are defined from 0 to 1 rotor station. Table 5.4 and describes the blade chord length at each rotor station. Table *5.5* includes blades linear twist at each rotor station.

Table 5.4:Blade chord

Rotor Station	Chord (m)
0.00	0.0477
0.25	0.0830
0.5	0.0798
0.75	0.0765
1.00	0.0579

Table 5.5: Blade property

Rotor Station	Blade Twist(deg)	Mass Distribution (kg/m)
0.00	13.5	0.148
1.00	-4.5	0.148

Non-linear unsteady airloads option was selected to model airloads on blades that uses predefined airfoil table. User defined nodes are defined to model airloads accurately on each section of the blade. Non-uniform airfoil tables from CAMRAD were used to model non-linear unsteady airloads. Furthermore, Peters-He three state inflow model is used to incorporate the effects of induced velocity into the model. The following model can model the flow by three non-linear states. The three non-linear states are defined as follow [29].

- Uniform flow
- Side to side gradient
- A fore to aft gradient

5.1.3. Airframe

The airframe/fuselage of hexacopter is modeled as a rigid fuselage with six non-linear degrees of freedom. In other words, the airframe has all three-translation and rotational motions. The airframe/fuselage is defined by inputting the total vehicle mass and inertia properties. The parameters shown in Table 5.6 are parameters taken from CAMRAD. Similar to CAMRAD, FLIGHTLAB uses total vehicle mass and inertial properties and rotor mass distribution to compute fuselage mass and inertial properties. Specifically, FLIGHTLAB calculates rotor inertia properties through using mass distribution along the rotor blade and subtracts it from total vehicle inertial properties to obtain fuselage mass and inertial properties. The total vehicle center of gravity is also defined. No aerodynamic loads on the airframe are being modeled due to configuration of a hexacopter. Furthermore, there are no additional aerodynamic surfaces being added to model as no other aerodynamics surfaces are needed for a hexacopter to perform its mission. For the purpose of the project pilot station and sensors have been neglected as well.

Table 5.6:Airframe parameters

Parameter	Value
Vehicle c.g. (m)	[0,0,-0.08]
Total vehicle mass (kg)	17.81
Total roll moment of inertia ($kg.m^2$)	4.127
Total pitch moment of inertia ($kg.m^2$)	4.012

Total yaw moment of inertia ($kg.m^2$)	7.449
Total X-Y product of inertia ($kg.m^2$)	0
Total X-Z product of inertia ($kg.m^2$)	0
Total Y-Z product of inertia ($kg.m^2$)	0

5.1.4. Propulsion

For this project purposes, the propulsion system of the hexacopter is being modeled as an ideal engine. The following choice is made to accurately model flight dynamics without any loss in power over time.

5.1.5. Flight Control

Once a model has been fully setup, CSGE (Control System Graphical Editor) is used to design the control mixer for the model that can be integrated into FLME. The designed control system takes the following pilot input. In other words, FLIGHTLAB describes its control inputs as "pilot" inputs. The same terminology is used for a fully autonomous vehicle like hexacopter.

- Initial longitudinal stick
- Initial lateral stick
- Initial collective
- Initial pedal

Each pilot input mentioned above is in terms of percentage with travel range of [0,100] percent. Figure 5.1 illustrates the control mixer designed for the hexacopter. As seen in the figures below, the designed hexacopter only has collective control. Therefore, thrust is generated by changing the collective of each rotor instead of changing rotor rpm. All pilot inputs are transferred through a swashplate mechanism. Specifically, the vertical force is generated by changing the collective of all rotors. The change in collective of all rotors is transferred to all six swashplates. Furthermore, a yaw moment is produced through differential collective which depends on the rotating direction of each rotor. Both pitch and roll moments are generated by change in thrust produced by a unique collective combination of different rotors. No yaw and vertical force are generated when producing both roll and pitch moments. Equations 5.1-5.6 presents the designed mixer mathematically. Where,

- θ = Swashplate collective input
- δ_{xc} =Collective input in deg
- δ_{xa} = Lateral input in deg
- δ_{xb} = Longitudinal input in deg
- δ_{xp} = Pedal Input in deg

$$\theta_1 = \delta_{xc} + 0 * \delta_{xa} + \delta_{xb} - \delta_{xp} \quad (5.1)$$

$$\theta_2 = \delta_{xc} - 0.86 * \delta_{xa} + 0.5 * \delta_{xb} + \delta_{xp} \quad (5.2)$$

$$\theta_3 = \delta_{xc} - 0.86 * \delta_{xa} - 0.5 * \delta_{xb} - \delta_{xp} \quad 5.3$$

$$\theta_4 = \delta_{xc} + 0 * \delta_{xa} - \delta_{xb} + \delta_{xp} \quad 5.4$$

$$\theta_5 = \delta_{xc} + 0.86 * \delta_{xa} - 0.5 * \delta_{xb} - \delta_{xp} \quad 5.5$$

$$\theta_6 = \delta_{xc} + 0.86 * \delta_{xa} + 0.5 * \delta_{xb} + \delta_{xp} \quad 5.6$$

Each rotor is listed in Figure *5.2*. All responses are converted into degrees before transferring the input to each swashplate. For example, in case of a collective input, all other inputs are set to zero and the input angle is converted into degrees before transferring it to all six swashplates. In case of the lateral input, negative collective is applied to rotor number 2 and 3, whereas positive collective is applied to rotor 5 and 6. During lateral moment, the collective of rotors 1 and 2 are set to zero. Similarly for the longitudinal input, positive collective is applied rotors 1,2, and 6. Whereas, negative collective input is applied to rotors 3,4, and 5. Applying the above collective input, results in nose up moment of the hexacopter. Yaw moment is obtained by applying positive collective to rotors 2,4, and 6 and negative to rotors 1,3, and 5.

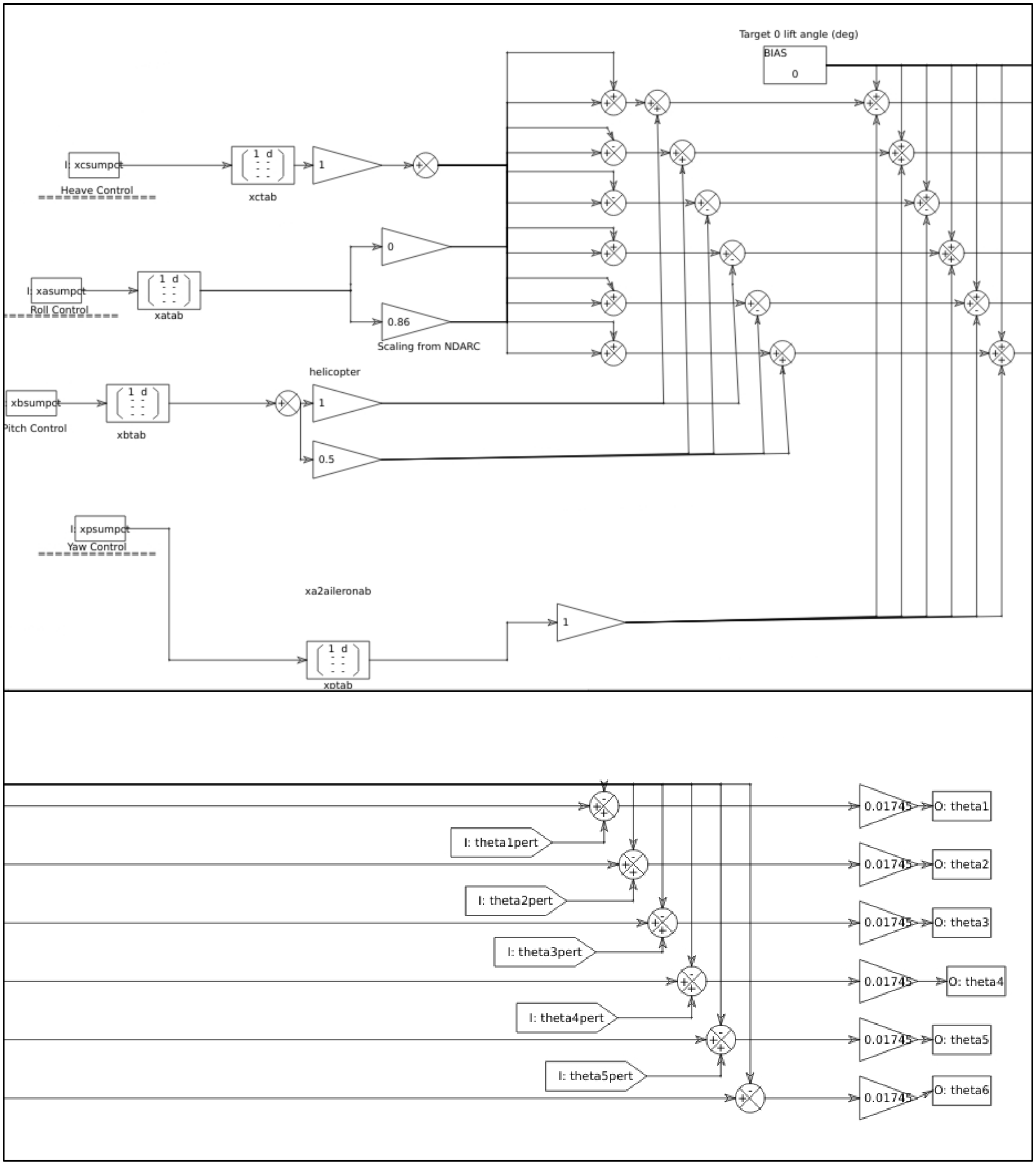

Figure 5.1:Control mixer for the hexacopter

The model is ready to be validated after the control input mixer is implemented into FLME. Figure 5.2 and Figure 5.3 show the top and side view of the hexacopter respectively. The model consists of aerodynamic, structural, masses, and geometry components. The airframe is shown as a point mass with no available airloads, whereas all six rotors have distributed mass along the blade length with airloads and flap hinge offset (Figure 5.4).

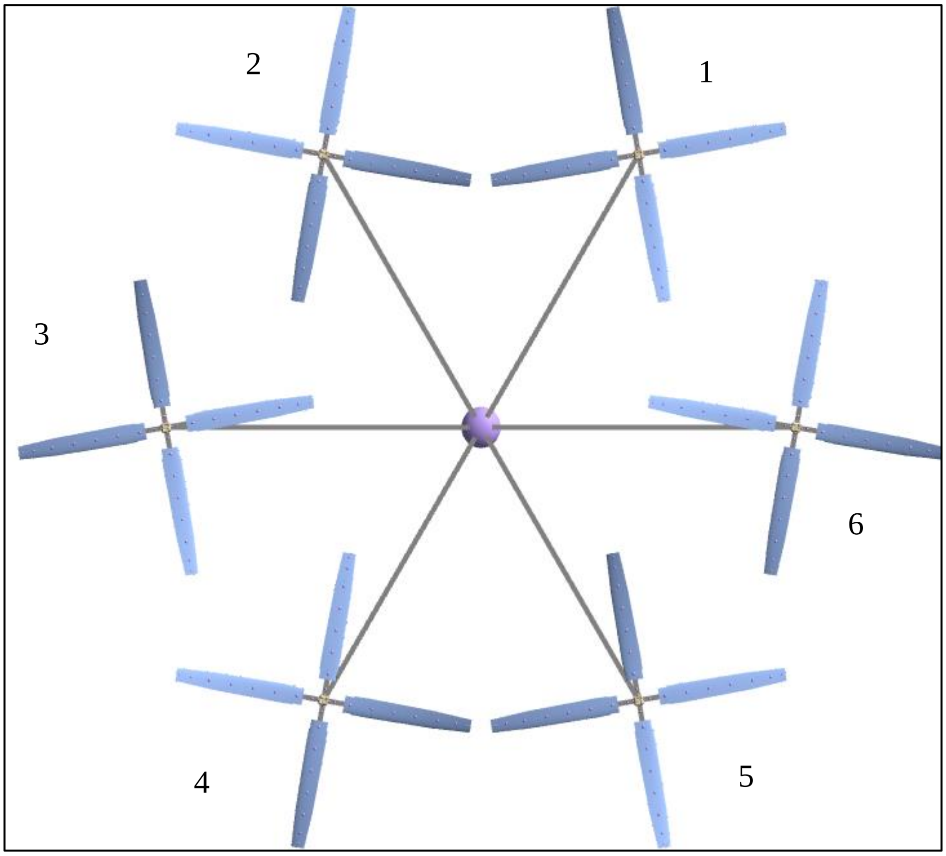

Figure 5.2: Top view of the designed hexacopter

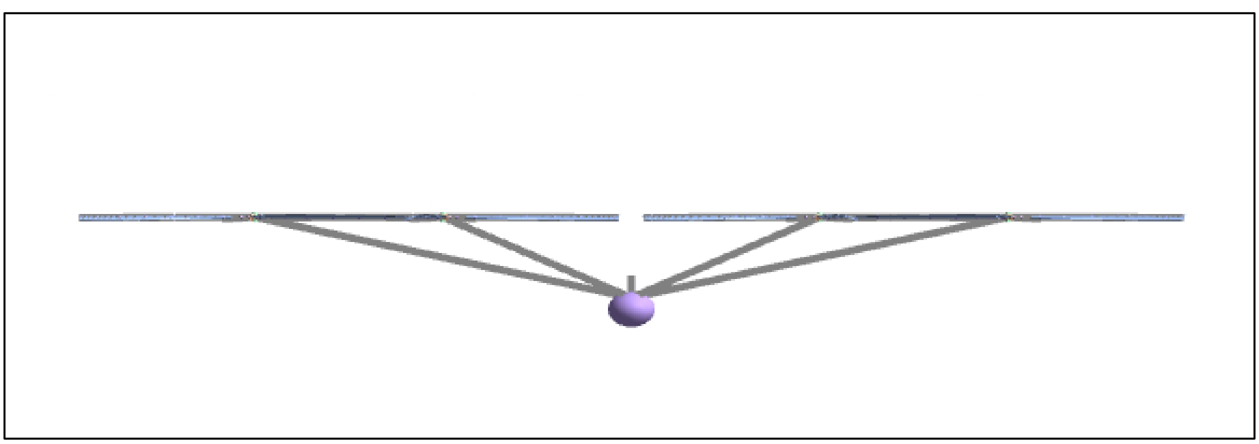

Figure 5.3:Side view of the designed hexacopter

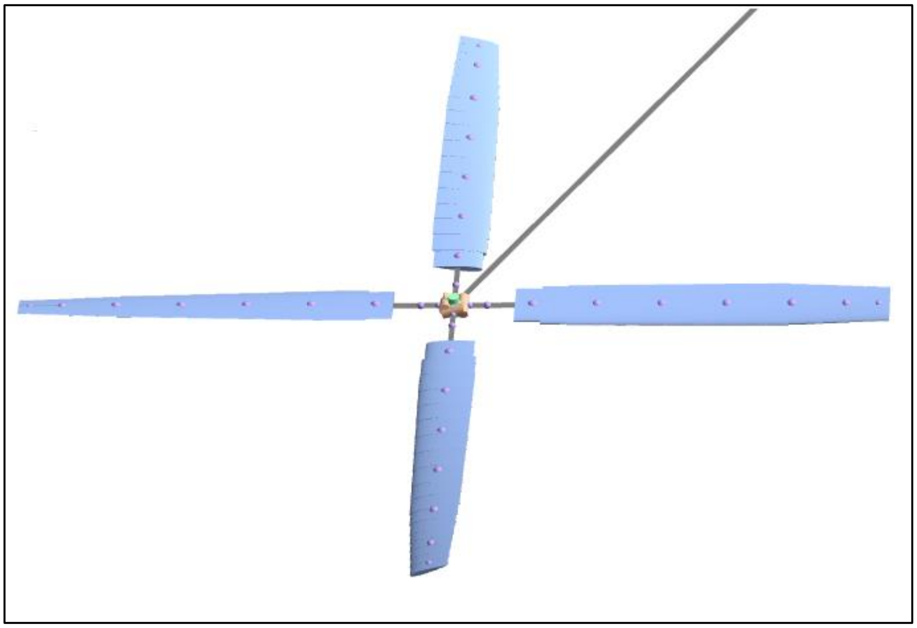

Figure 5.4:Rotor design

5.2.Mars' Atmosphere

To model the change in dynamics caused by two different environments, another model is built using a similar FLME template but in Mars' atmospheric condition.

5.2.1. Solution Parameters and Environment

Like the hexacopter model in Earth's environment, the Mars model also uses the solution parameters mentioned in Table 5.1. but with the environment changed to Mars conditions. NASA's Mars atmosphere model is used to produce the atmospheric table needed to change the environment to Mars conditions [30]. Mars atmosphere is divided into two separate atmospheres, i.e., lower atmosphere and upper atmosphere. The lower atmosphere is defined from the surface of the Mars to an altitude of 7,000 meters. Temperature and pressure for altitude of 7,000 meters and below are calculated as follow [30],

$$\mathrm{T} = -31 * 0.000998 * \mathrm{h} \tag{5.7}$$

$$\mathrm{P} = 0.699 * \mathrm{e}^{-0.00009*\mathrm{h}} \tag{5.8}$$

Where, T is temperature in (°C) and P is pressure in (kPa). For an altitude above 7,000 meters, temperature and pressure are calculated using the following equation [30].

$$\mathrm{T} = -23.4 - 0.00222 * \mathrm{h} \tag{5.9}$$

$$P = 0.699 * e^{\wedge}(-0.00009 * h) \qquad 5.10$$

Density at the desired altitude is computed using the following equation.

$$\rho = P/[.1921 * (T + 273.1)] \qquad 5.11$$

Moreover, environment parameters such as,

- Specific heat ratio
- Gas constant
- Initial latitude

are also input according to Mars atmosphere which are as follow.

Table 5.7:Mars model parameters

Parameters	Value
Specific heat ratio (nd)	1.29
Gas constant (N-m/kg/degK)	191.8
Initial latitude (deg)	37.6

The Mars atmospheric table is attached in appendix B.

5.2.2. Rotor

Like the model built in Earth's atmosphere, the Mars model also consists of six rotor that also uses blade element theory. Each rotor is four bladed with a radius of 0.64m. The model is built with same rotor parameters as shown in Table 5.2 except rotor rpm are scaled to Mars atmospheric condition to obtain the same amount of power as in Earth's atmosphere. Table 5.8 shows the change in rotor rpm when operated on Earth and Mars.

Table 5.8: Rotor speed comparison

	Parameters	Value
Mars	Rotor 1-6 (rpm)	2782
Earth	Rotor 1-6 (rpm)	507

The rotor speed on Mars is much higher due to the atmosphere on Mars being very thin. Mathematically, the change in rotor speed is due to the change in speed of sound and density. Lower density on Mars reduces the lift generated per blade area. Therefore, rotor rpm needs to be scaled to obtain the same amount of thrust as it generates on Earth at 507 rpm. Furthermore, no addition changes were made between the Earth and Mars model for the given subsections.

- Airframe
- Propulsion
- Flight control

Figure 5.5 shows the model represented in FLME. Both models shown in Figure 5.2 and Figure 5.5 are identical as the only the operating conditions were changed between each model.

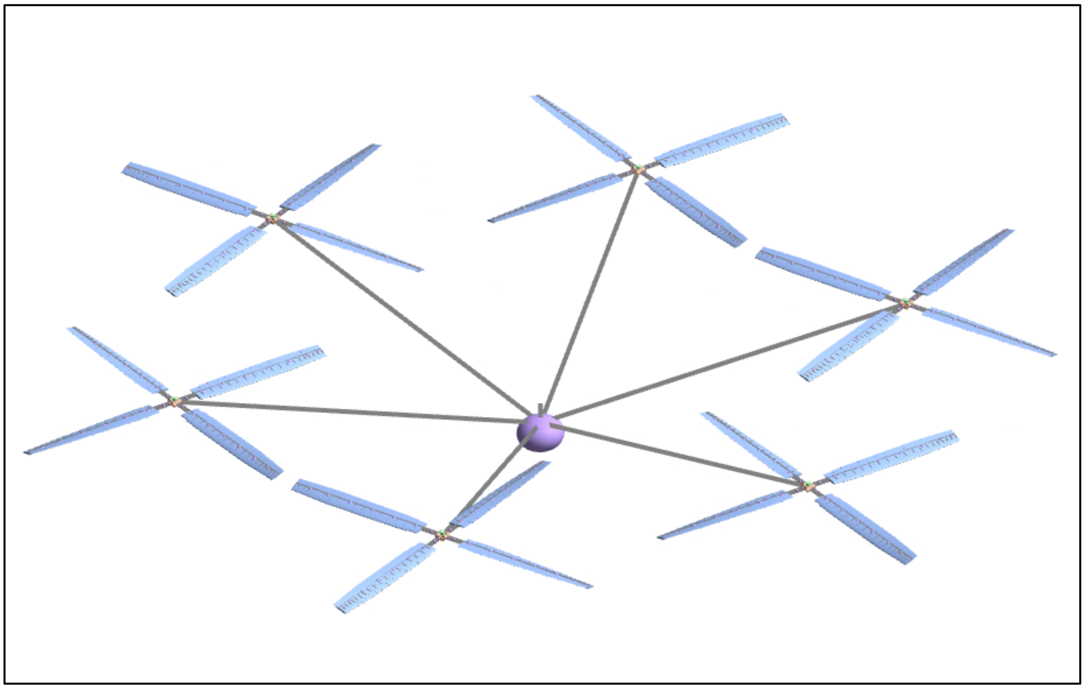

Figure 5.5: Hexacopter model for Mars atmosphere

Chapter 6. Linear Model Extraction and Validation

After the model is configured in FLME, the model is exported into X-analysis to perform flight dynamics analysis. For this project purposes, the flight dynamics of hexacopter in hover is analyzed both in Earth and Mars' environment. At first, linear time invariant (LTI) model is obtained by linearizing the non-linear dynamics of the hexacopter about an equilibrium point. The equilibrium point is reached by performing Newton Raphson algorithm with a relaxation factor of 0.15. Both translation and rotational rates were set as trim targets with a tolerance of 0.04. Once an equilibrium point was obtained, the system was linearized by reducing all control states. Genq perturbation method is used to generate linear responses of the hexacopter in Earth's atmosphere. The trim performance parameters are shown in Table 6.1. The trim collective trim mentioned in Table 6.1 translates as 0.2123 degrees.

Table 6.1:Response parameters

Parameters	Value
Longitudinal stick trim	50
Lateral stick trim	50
Collective stick trim	62
Pedal trim	50
Vehicle pitch attitude (deg)	0.00
Vehicle roll attitude (deg)	0.00

6.1.Flight Dynamic Analysis in Earth's Atmosphere

Upon linearizing the non-linear dynamics of hexacopter, linearized eigenvalues were extracted to examine the characteristic of the model. Figure 6.1 shows the eigenvalues of the designed hexacopter in Earth's atmosphere. A linear model of hexacopter was also extracted from CAMRAD, that the results obtained from FLIGHTLAB can be validated. Both sets of eigenvalues align very close to each other with 0.8% difference and predicts similar damping characteristic of the hexacopter in Earth's atmosphere. The eigenvalues from both FLIGHTLAB and CAMRAD are attached in appendix D. Moreover, each linear system predicts that the model is both statically and dynamically stable. Specifically, Figure 6.1 shows at least one pole exists at the origin, thus confirming the system can return to its equilibrium point when disturbed. Furthermore, FLIGHTLAB shows all poles of system in the left half plane, predicting a stable system whereas, CAMRAD shows one set of poles in the right half plane, thus predicting unstable behavior of hexacopter in Earth's atmosphere. The difference is due to the difference in modeling inflow which is explained later in this section. Flapping, airframe and inflow modes are shown in Figure 6.1. The flapping modes exists at high frequency range of [420 600] rad/sec, whereas the airframe modes exist at very low frequency range of [0.1 10] rad/sec. Furthermore, inflow modes exist at lower frequency range of [0.1 10] rad/sec and at higher frequency range of [340 420] rad/sec. A slight difference in inflow modes is observed between FIGHTLAB and CAMRAD linear models. Both CAMRAD and FLIGHTLAB uses uniform inflow method that uses momentum potential flow theory to conduct rotor wake analysis. The difference occurs due to CAMRAD using empirical correction factor of 1.15. No inflow correction has been implemented in FLIGHTLAB. Furthermore, the modes retrieved from CAMRAD linear model are slightly more damped than the ones retrieved from FLIGHTLAB. Overall, the modes obtained from FLIGHTLAB are valid as they show similar model characteristic to the ones obtained from CAMRAD.

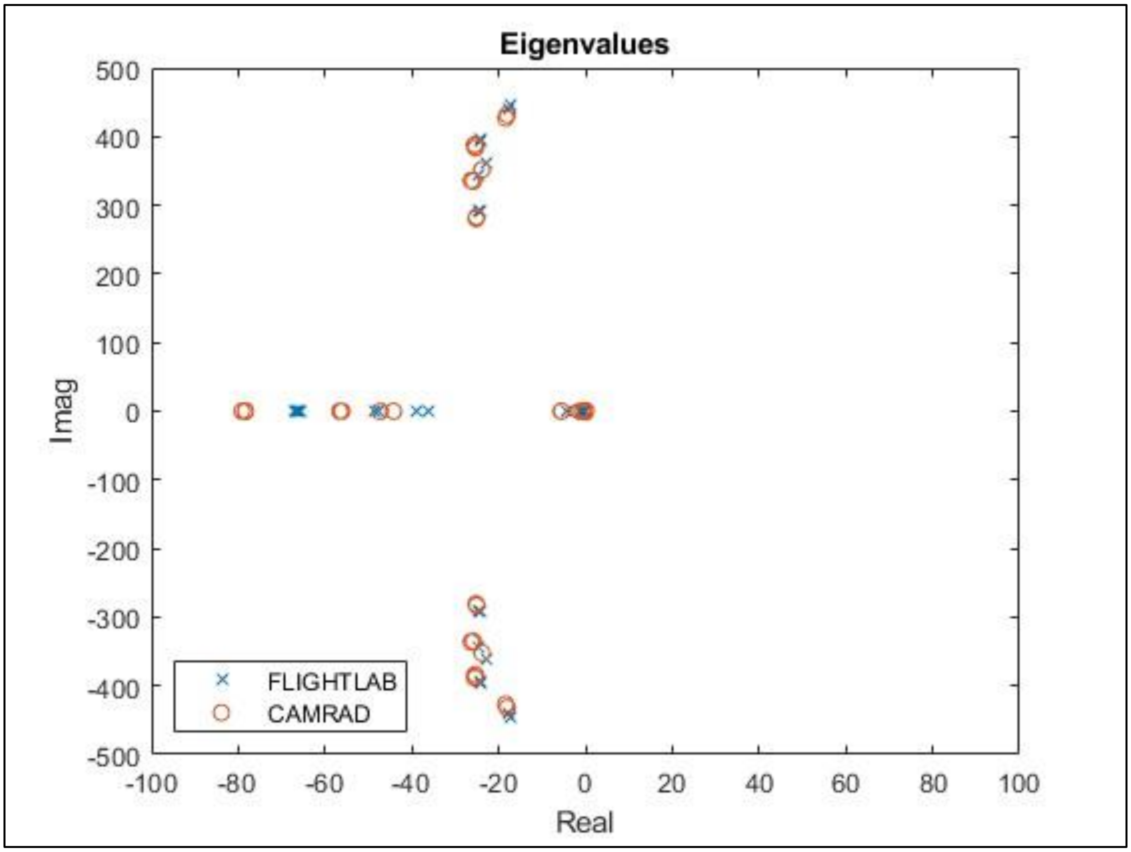

Figure 6.1: Eigenvalues of the hexacopter in Earth's atmosphere

In addition, frequency responses of the hexacopter are also extracted and validated against the CAMRAD model. Figure 6.2 shows the heave frequency response to a collective input. The responses of both linearized systems are plotted from 0.1 rad/s to 1000 rad/s. The results obtained from FLIGHTLAB aligns very closely with the results obtained from CAMRAD, thus validating the response produced by FLIGHTLAB. Figure 6.2 shows a first order response with a rotor mode present at the high frequency response. The present mode is the regressive mode which is generated at the frequency of $\upsilon_{flap} - 1$/rev. υ_{flap} is the flap frequency where coning mode occurs. For both heave and yaw rate, the regressive mode is generated at approximately 371 rad/sec. The coning rotor mode is generated due to blade flapping up and down. The mode is generated at the same frequency as rotating natural flap frequency. Specifically, a coning would be seen at approximately 430 rad/sec. furthermore, the system is also damped which is expected when operating in Earth's atmosphere. This is confirmed by the gradual decrease in phase angle which ensures that the system is damped. For flight control purposes, the heave response shown in Figure 6.2 is acceptable as no modes are present in the mid-range frequency and the response matches very closely to the one obtained from CAMRAD.

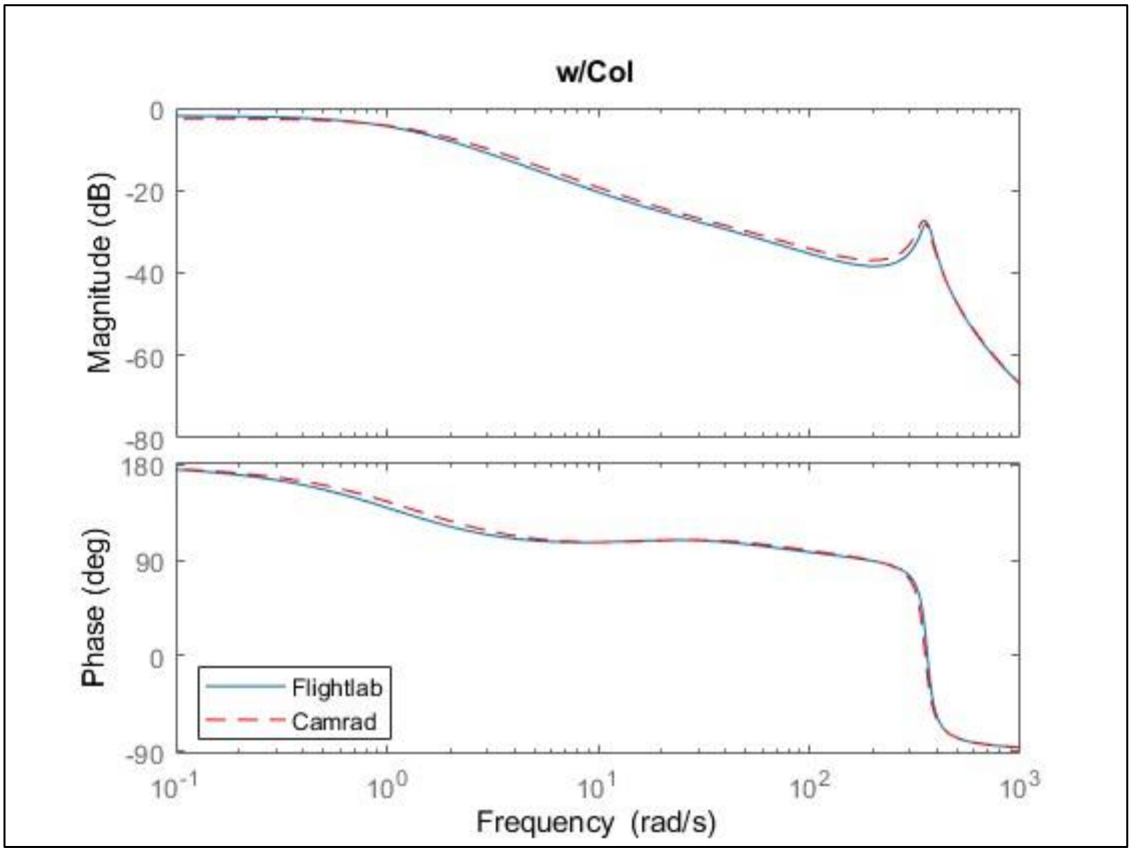

Figure 6.2: Heave response to collective input

Figure 6.3 shows the yaw rate response obtained from the linear model of FLIGHTLAB and CAMRAD. Like the heave response, the yaw rate response of the hexacopter from FLIGHTLAB also matches with the results obtained from CAMRAD. The obtained response is also first order response as expected with high damping characteristic due to Earth's atmosphere. Like heave response, a regressive mode is present at the same frequency.

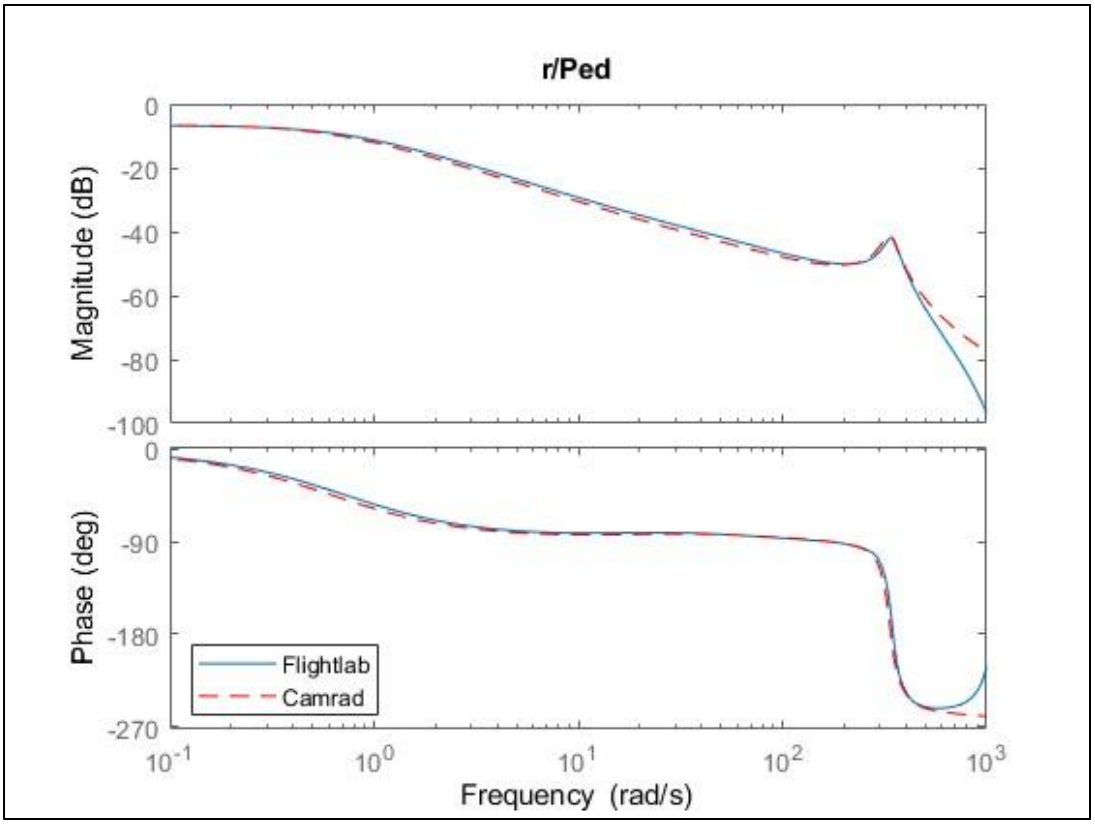

Figure 6.3: Yaw rate response to pedal input

Figure 6.4 and Figure 6.5 shows the pitch and roll rate response of the hexacopter in Earth's atmosphere respectively. Both figures also compare the two linear models obtained from FLIGHTLAB and CAMRAD. Like the frequency plots shown above, the characteristic and magnitude of both models aligns very closely. For example, the pitch response in from FLIGHTLAB has a magnitude of -0.279 dB at 1 rad/sec, whereas CAMRAD predicts a value of 0.504 dB at 1 rad/sec. Therefore, the results obtained from FLIGHTLAB are valid. When compared to the heave and yaw rate response, pitch rate and roll rate differ in both lower [0.1 10] rad/sec and high frequency range of [400 500] rad/sec. Specifically, an airframe mode is present at a lower frequency 0.5 rad/sec in FLIGHTLAB and at 10 rad/sec in CAMRAD for both pitch and roll rate responses. Specifically, there is a set of two conjugate complex airframe poles that exists in the right half complex plane at frequency of 1.06 rad/sec. Figure 6.7 shows the pole zero map of the hexacopter in Earth's atmosphere. The higher magnitude positive complex poles are shown in the CAMRAD model, whereas the positive poles in FLIGHTLAB are very small in magnitude and a lot closer to zero, thus can be neglected. Additional airframe modes are shown at a very low frequency of 4.65E-14 rad/sec (Figure 6.6). However, each model confirms both lateral and longitudinal phugoid modes in the right half plane of the system. The phugoid modes shown here are generated due to the coupling between the "attitude and horizontal speed states" [18]. The existence of modes can be understood by the given matrix [18].

$$A = \begin{bmatrix} 0 & -g & 0 \\ 0 & 0 & 1 \\ Mu & 0 & M_q \end{bmatrix} \quad 6.1$$

The above matrix is obtained from low frequency dynamics model below.

$$\begin{gathered} u' = X_u u - g\theta \\ q' = M_u + M_q q \\ \theta' = q \end{gathered} \quad 6.2$$

Matrix A is restricted to longitudinal dynamics and neglects longitudinal drag and pitch damping. The quantity M_u is helicopters pitch rate sensitivity to the gust hitting the helicopter from the front. M_q is the damping in Earth's atmosphere. As the gust becomes stronger, more nose-up moment is generated. The mode is stabilized by nose down moment generated either from the system or with the help of a control system. Even though, the phugoid mode exists in low frequency, it is still a fundamental part in designing a control system as it can help impose limitations on stability margin of the system. The shift in phase in lower frequency is due to each code, i.e., FLIGHTLAB and CAMRAD predicting different value of M_u which changes the distribution of thrust around the rotor disk. M_u is modeled differently due to not having inflow corrections in FLIGHTLAB model, which exists in CAMRAD. Furthermore, FLIGHTLAB and CAMRAD both uses different methods to model inflow. FLIGHTLAB uses momentum theory whereas, CAMRAD uses unsteady actuator disk theory. Equations 6.3 and 6.4 shows matrix of inflow gains for both momentum and actuator disk theory. As seen below, the gains in both matrices are different which can be one of the possible reasons for obtaining different value of M_u from FLIGHTLAB and CAMRAD [31].

$$L^* = \frac{1}{v} \begin{bmatrix} \frac{9}{16} & -\frac{3\pi}{8} * \frac{\mu}{\sqrt{\mu^2 + \lambda^2 + |\lambda|}} & 0 \\ \frac{\frac{3\pi}{8}\mu}{\sqrt{(\mu^2 + \lambda^2} + |\lambda|} & \frac{75}{16} * \frac{|\lambda|}{\sqrt{(\mu^2 + \lambda^2} + |\lambda|} & 0 \\ 0 & 0 & \frac{75}{16} * \frac{\sqrt{\mu^2 + \lambda^2}}{\sqrt{(\mu^2 + \lambda^2} + |\lambda|} \end{bmatrix} \quad 6.3$$

$$L^* = \frac{1}{v}\begin{bmatrix} \frac{1}{2} & -\frac{15\pi}{64} * \frac{\mu}{\sqrt{\mu^2+\lambda^2+|\lambda|}} & 0 \\ \frac{\frac{15\pi}{64}\mu}{\sqrt{(\mu^2+\lambda^2}+|\lambda|} & 4 * \frac{|\lambda|}{\sqrt{(\mu^2+\lambda^2}+|\lambda|} & 0 \\ 0 & 0 & 4 * \frac{\sqrt{\mu^2+\lambda^2}}{\sqrt{(\mu^2+\lambda^2}+|\lambda|} \end{bmatrix} \quad 6.4$$

Furthermore, a coning mode is also present in the higher frequency. It can be confirmed that the present mode is a coning mode since it exists exactly at the frequency of the rotating flap mode, i.e., 430 rad/sec. As mentioned previously, designing a control system only requires stable responses in mid-range frequencies as designing the control system around higher frequency range can overwork the actuators. Therefore, both longitudinal and lateral rates can easily be controlled with a control system as there are no resonant frequency in mid-range frequencies of [0.1 100] rad/sec.

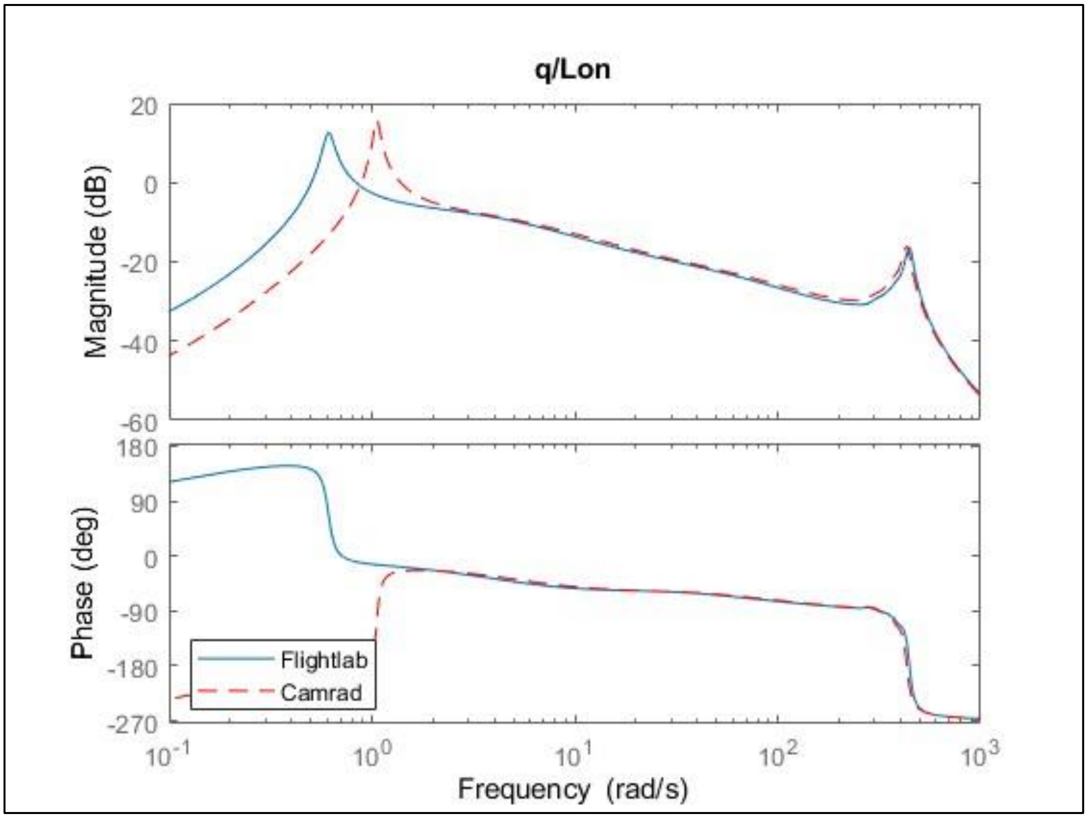

Figure 6.4: Pitch rate response to longitudinal input

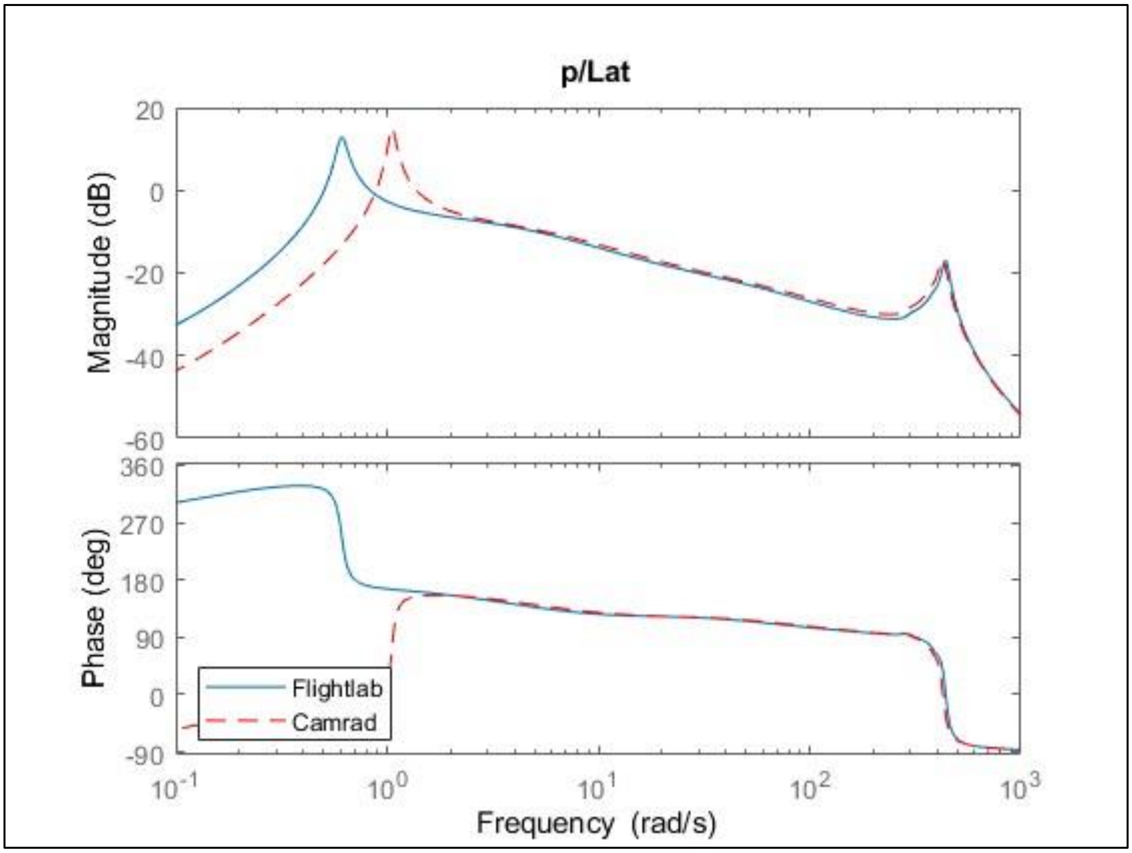

Figure 6.5: Roll rate response to lateral input

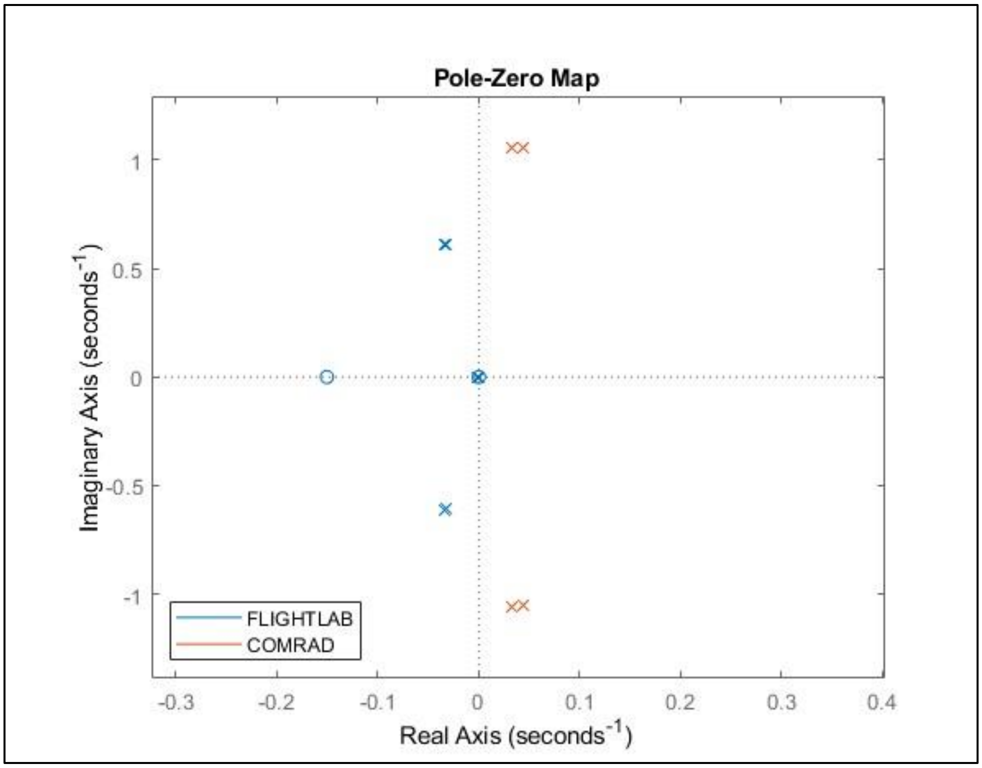

Figure 6.7: Pole zero map in Earth's atmosphere

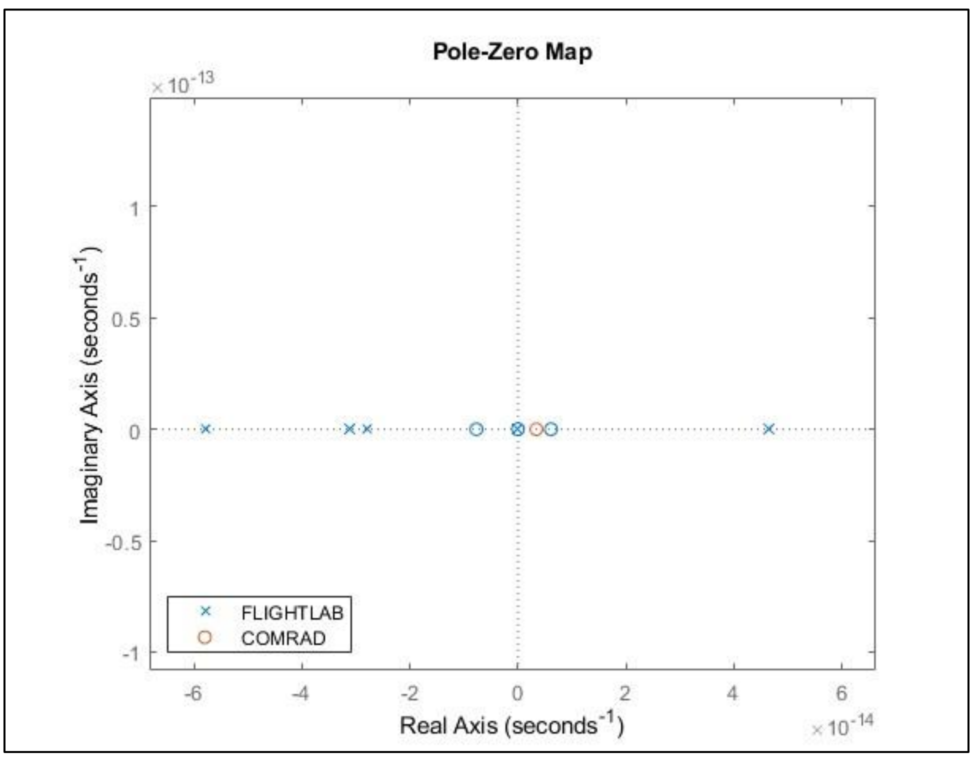

Figure 6.6: Zoomed in pole zero map in Earth's atmosphere

6.2. Flight Dynamic Analysis in Mars Atmosphere

As mentioned previously, flying on Mars comes with its own challenges. Mars atmosphere constitutes of 1% of the Earth density. Airfoils behave a lot different in Martian atmosphere than they behave on Earth. This is due to airfoils having to operate in low Reynolds number in the range of 10,000 to 25,000 [21] which reduces the lift generated per blade area. Hence, it is important to understand the dynamic behavior of a vehicle in Mars environment to check if a dynamically matched surrogate model can be created to conduct testing on Earth. Like flight dynamic analysis conducted in X-analysis for the hexacopter operating in Earth's atmosphere, Mars model is also analyzed in the Mars atmosphere. Once the model is imported into X-analysis, Mars test conditions were applied. The applied test conditions are attached in appendix C.

Due to Newton-Raphson trim algorithm not being able to achieve a trim convergence solution for Mars' condition lock number, artificial flap damping is introduced in the system. It is necessary to include artificial flap damping as FLIGHTLAB is not able to obtain an equilibrium point without introducing an artificial flapping coefficient. The reason is yet to be discovered. Specifically, $0.85\ kg * m^2/sec$ flap hinge damping coefficient is introduced. An equilibrium point is computed using the Newton Raphson algorithm with a relaxation factor of 0.15 using the flap hinge damping coefficient. After an equilibrium point is reached, the nonlinear dynamics of hexacopter on Mars is linearized without the flap hinge damping coefficient included into the system. In other words, the flap hinge coefficient of all six rotors is set to zero before linearization of hexacopter' s non-linear dynamics. To validate FLIGHTLAB'S linearized system, the obtained frequency responses from FLIGHTLAB are validated against the frequency responses from CAMRAD. First, eigenvalues from both computational methods are compared. Figure 6.8 shows the eigenvalues of Mars' hexacopter in Mars' test condition. As seen in the figure below, the eigenvalues obtained from FLIGHTLAB matches very closely with the eigenvalues from CAMRAD. Both models consist of higher frequency rotor modes [450 742] rad/sec, lower frequency airframe modes [0.1 10] rad/sec. Like the model in Earth's atmosphere, inflow modes exist in both low and high frequency range, i.e. [0 200] rad/sec and [400 600] rad/sec. The modes presented here are very less damped due to Mars' density being lower than Earth. Like the hexacopter in Earth's atmosphere, the hexacopter in Mars' atmosphere is also not stable as a set of poles exist in the right-side plane. Figure 6.9 gives a better representation of eigenvalues in Mars' atmosphere for stability purposes. Moreover, the eigenvalues obtained from CAMRAD are slightly more damped than the ones obtained from FLIGHTLAB. This is possible due to slightest difference in operating density and difference in inertial properties of the model.

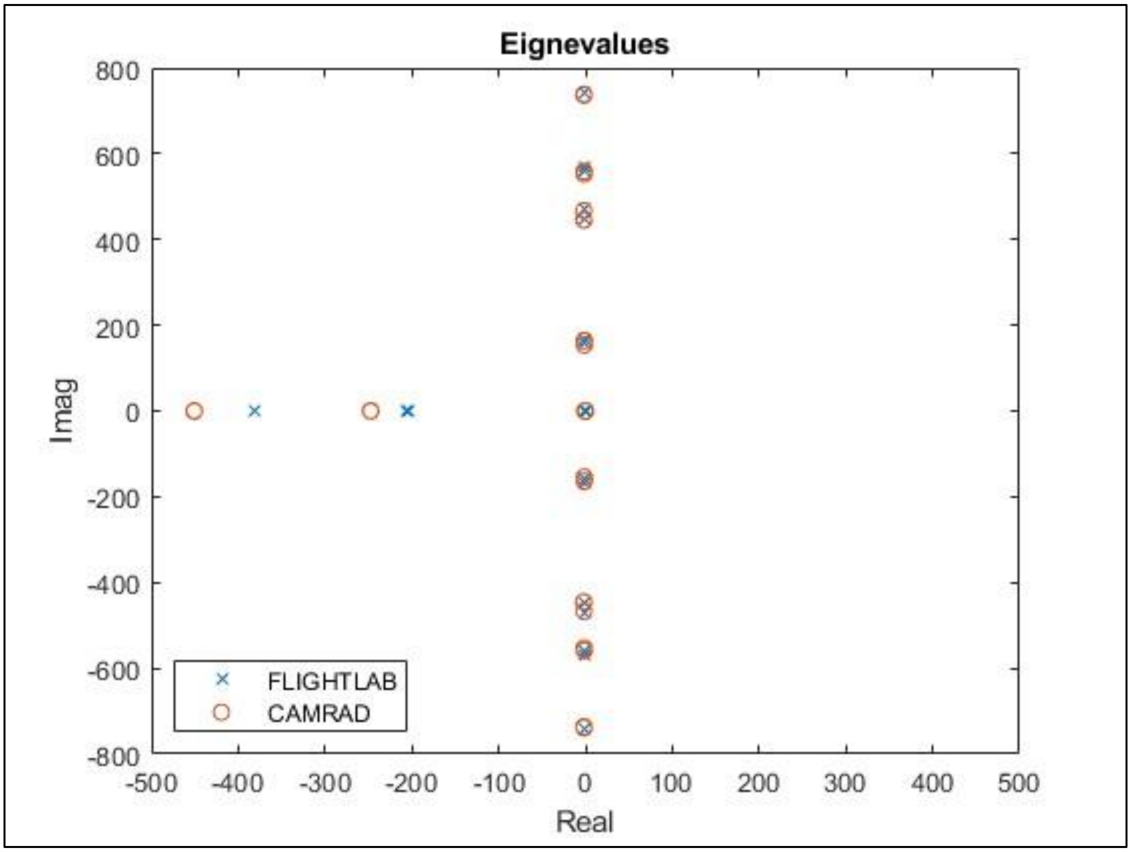

Figure 6.8: Eigenvalues of hexacopter in Mar's atmosphere

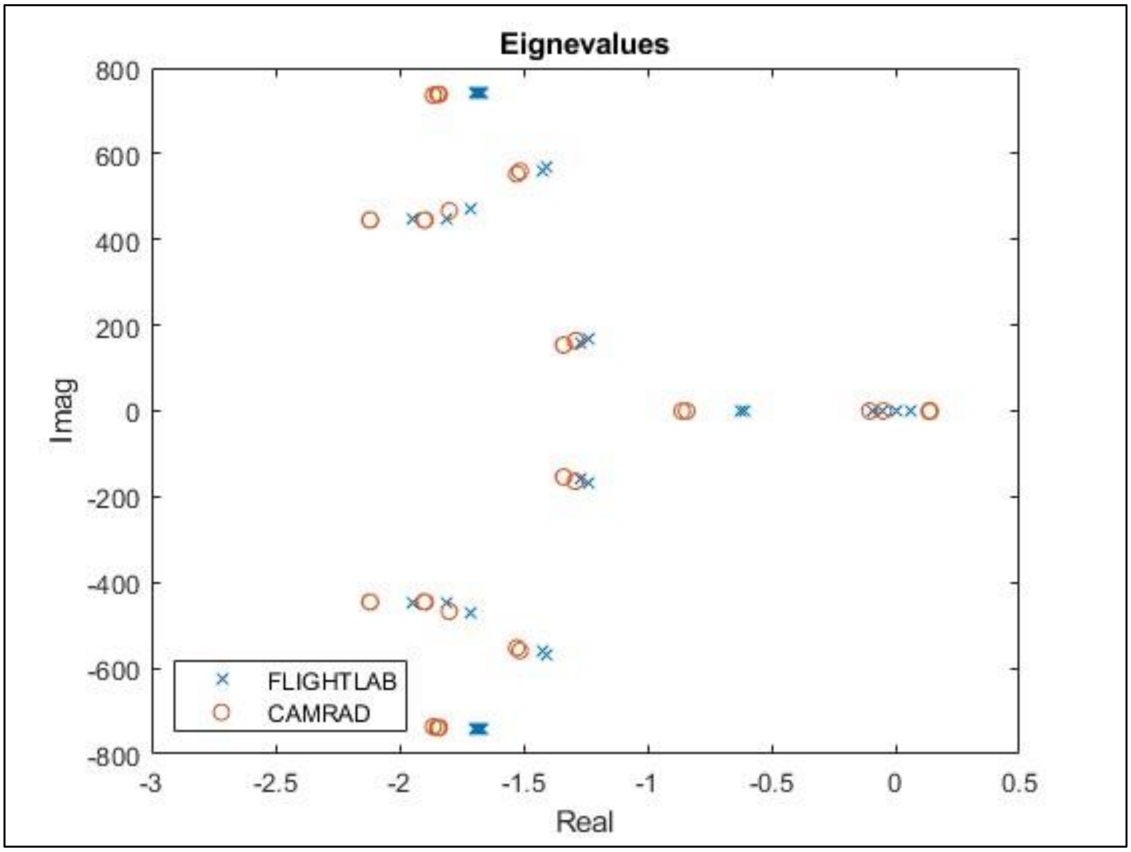

Figure 6.9: Zoomed in eigenvalues of hexacopter in Mars' atmosphere

Figure 6.10 shows the heave response of the hexacopter in Mars' atmosphere to collective input. Like the heave response obtained in Earth's atmosphere, the heave response obtained from the linearized model from FLIGHTLAB is validated against the linear model obtained from CAMRDAD. Both responses match very closely with each other, thus the heave response to collective input is valid. A coning mode is generated in the high frequency range of the response. The mode is coning mode as it is generated at the rotating flapping frequency of 448 rad/sec. The phase shift in the heave response is very sudden. Specifically, the phase drops to zero suddenly due to Mars' atmosphere being low in density and very slightly damped.

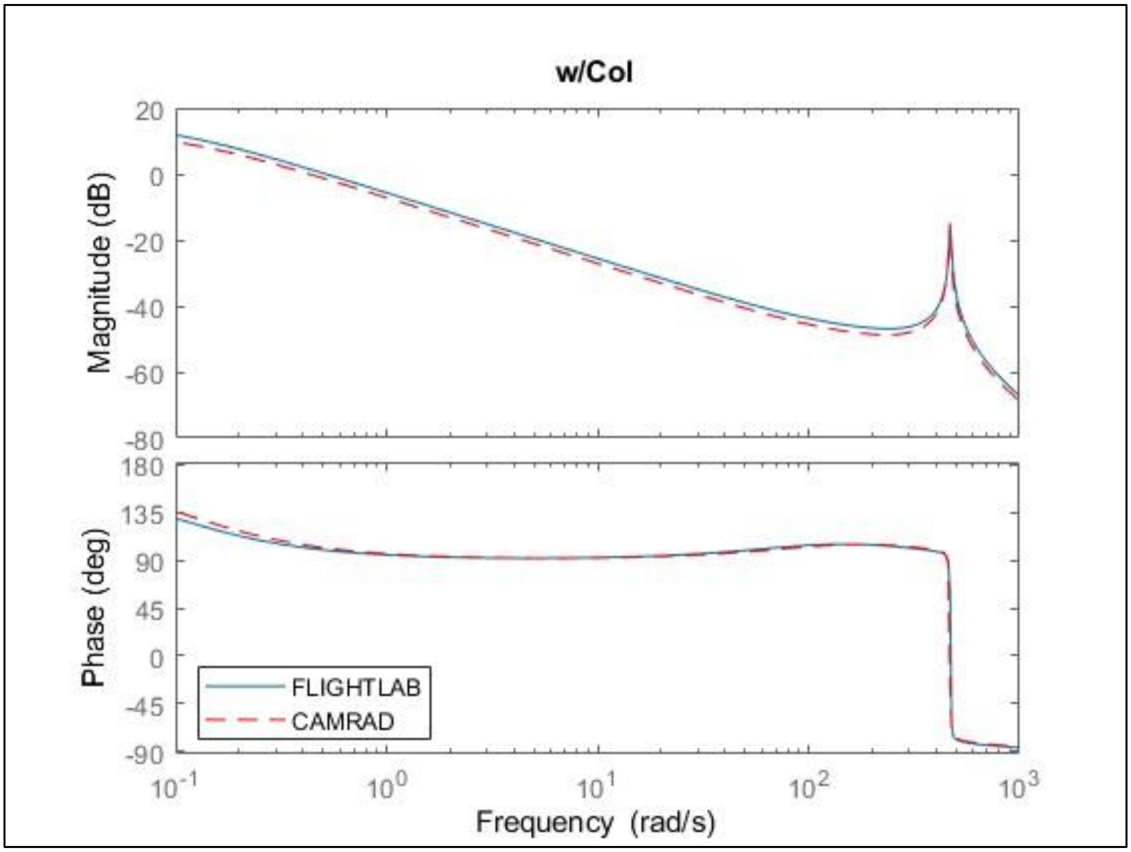

Figure 6.10: Heave response to collective input in Mars’ atmosphere

Figure 6.11 shows the yaw rate response to pedal input in Mars’ atmosphere. Like the heave response, the yaw rate response from FLIGHTLAB matches very closely with the linear model response from CAMRAD. Thus, validating the results obtained from FLIGHTLAB. Furthermore, a coning mode is also present in the yaw rate at the rotating natural frequency along with both regressive and advancing modes. The regressive and advancing modes are generated at $\nu_{flap} - 1/rev$ and $\nu_{flap} + 1/rev$ respectively. For the hexacopter operating in Mars’ condition with a $\nu_{flap} = 1.54/rev$, the regressing and advancing mode exist at approximately 157 rad/sec and approximately 740 rad/sec respectively. Figure 6.12 shows both regressive and advancing modes in the yaw rate response of hexacopter in Mars’ environment.

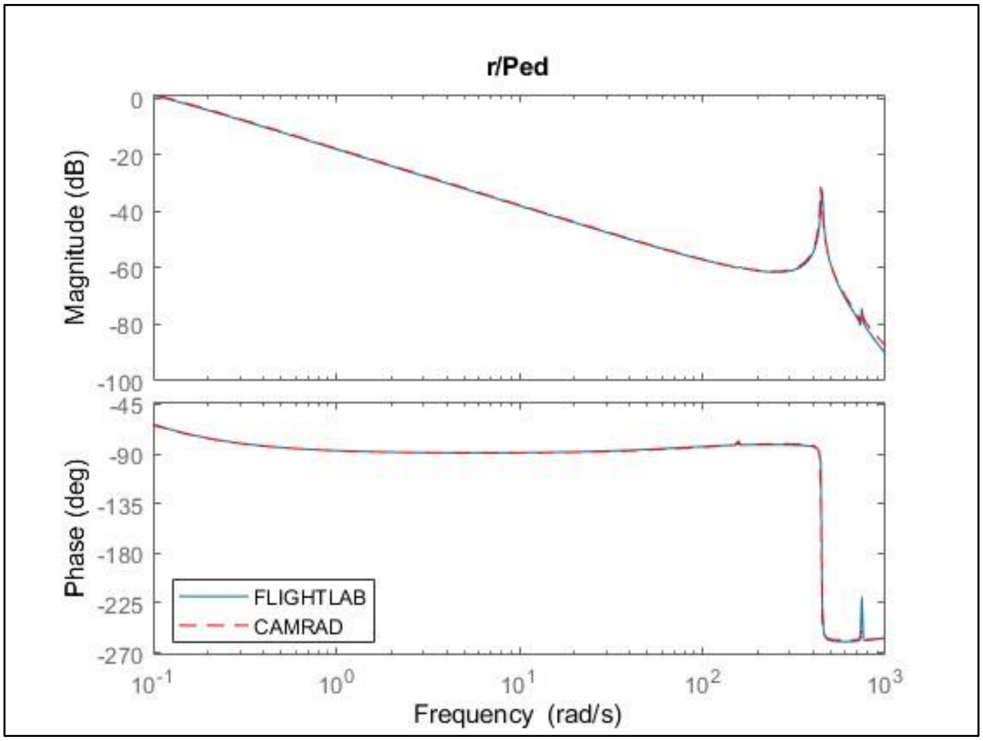

Figure 6.11: Yaw rate response to pedal input in Mars' atmosphere

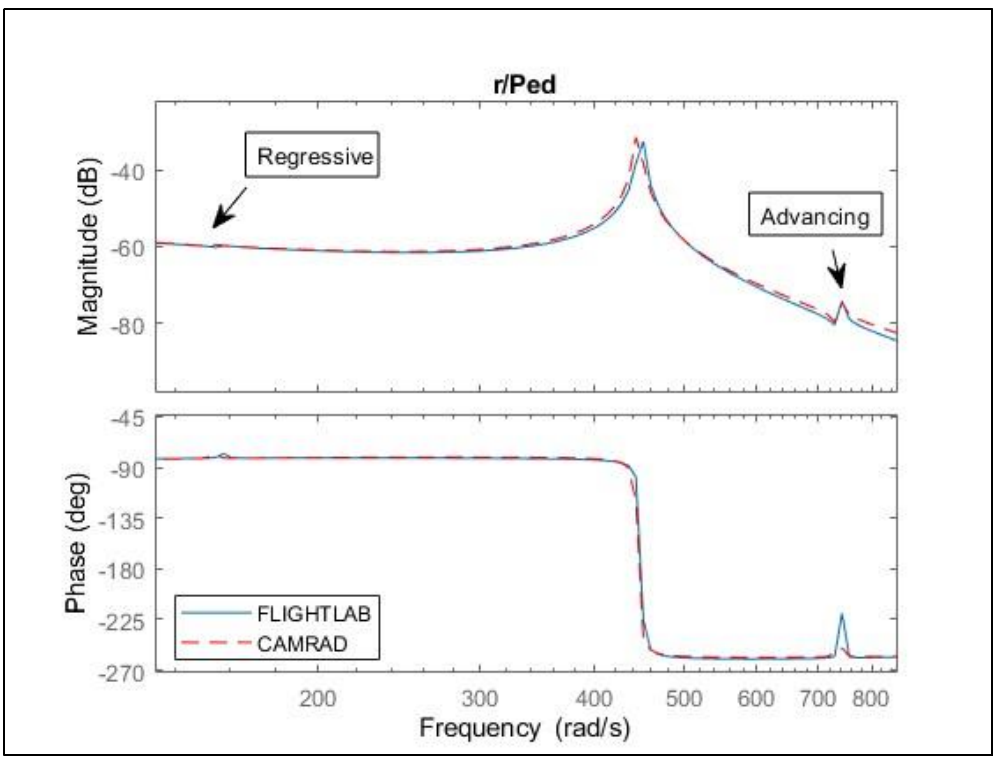

Figure 6.12: Regressive and advancing modes in yaw rate response in Mars' atmosphere

Figure 6.13 and Figure 6.14 show the pitch rate and roll rate response of the hexacopter in Mars' atmosphere respectively. Both responses do match closely with the results obtained from CAMRAD. Therefore, the results obtained from FLIGHTLAB are valid. Both responses do include a phugoid mode in the low frequency range with regressive, coning, and advancing modes in the high frequency range. As mentioned before, the phugoid is present due to the pitch and roll rate being sensitive to the gust or longitudinal velocity hitting the airframe. The phugoid mode in both responses is verified by the existence of unstable poles in right half plane (Figure 6.15). Furthermore, the phugoid mode obtained from FLIGHTLAB's linear model is slightly higher in magnitude than the one obtained from CAMRAD linear model. This can be caused by even the slightest different in gravity or M_u, explained above in section 6.1. The unstable poles shown in figure increase in frequency as M_u and gravity increases. In addition, the regressive and advancing modes exist at $\nu_{flap} - 1/rev$ (157 rad/sec) and $\nu_{flap} + 1/rev$ (740 rad/sec) respectively. The coning mode exists at the rotational flapping frequency of 448 rad/sec as expected.

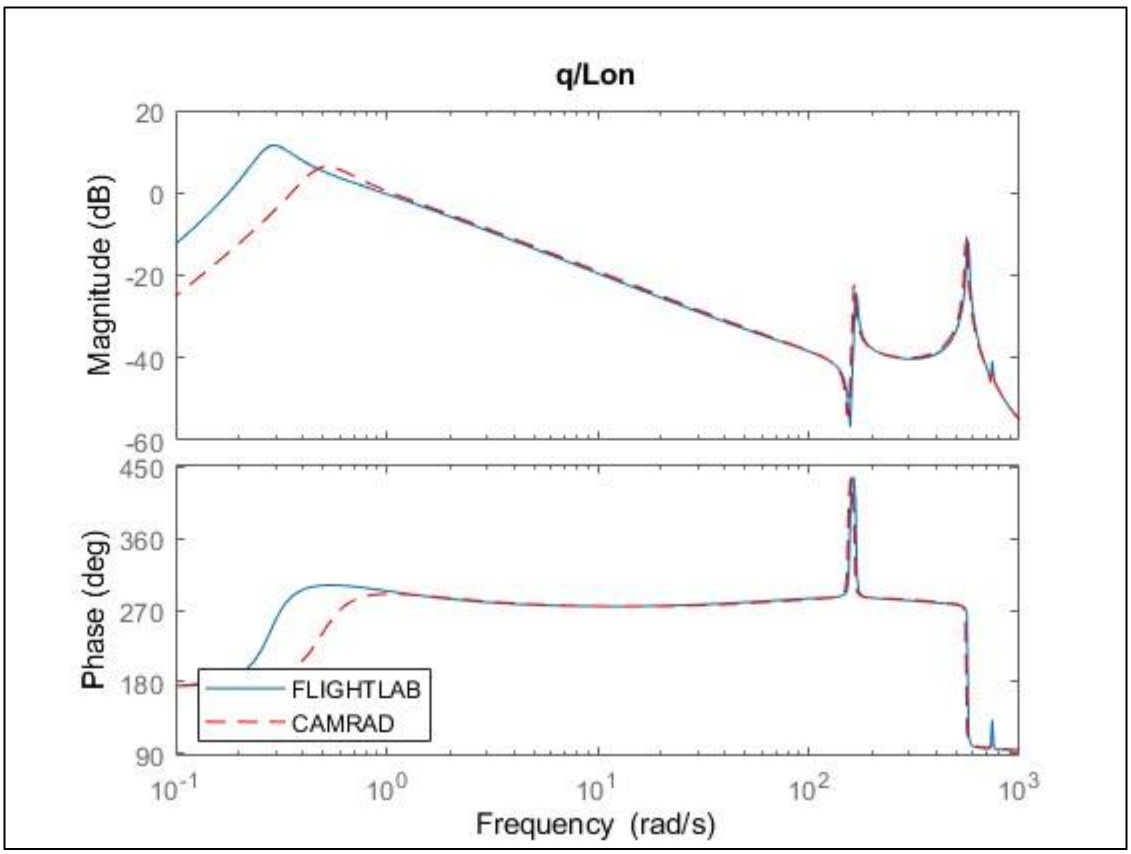

Figure 6.13: Pitch rate response to longitudinal input in Mars' atmosphere

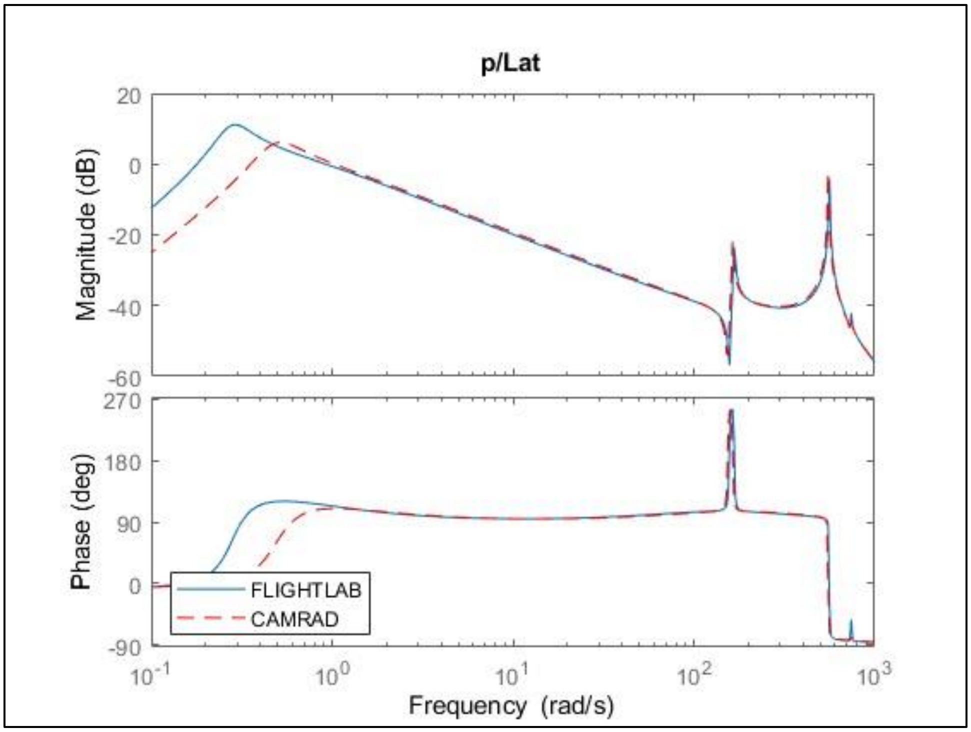

Figure 6.14: Yaw rate response to pedal input in Mars' environment

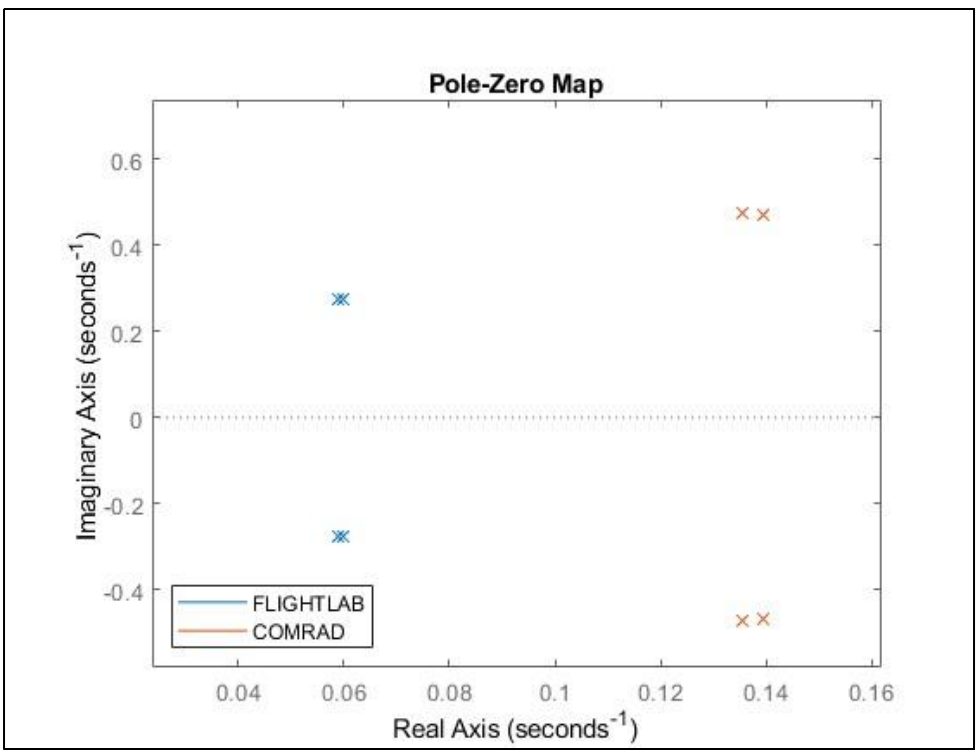

Figure 6.15: Pole zero map of the model in Mars' atmosphere

Chapter 7. Flight Behavior Differences Between Earth and Mars Environment

One of the main requirements of flying on Mars is having autonomous flights from one end to the other. Thus, understand the flight behavior when operating in Mars' atmospheric condition is important. In this chapter, the flight behavior differences between Earth and Mars are discussed. Figure 7.1 shows the eigenvalues obtained from FLIGHTLAB's linear model in Earth and Mars' environment. As seen in the figure below, the rotor (flapping) modes and inflow modes in Earth atmosphere are more damped than the ones in Mars' environment. Furthermore, the scaling effect between the Earth and Mars model can also be interpreted from the eigenvalues below. Due to the higher density in Earth, all modes do occur at much lower frequency than they do in Mars' atmosphere. Both models are stable as discussed previously.

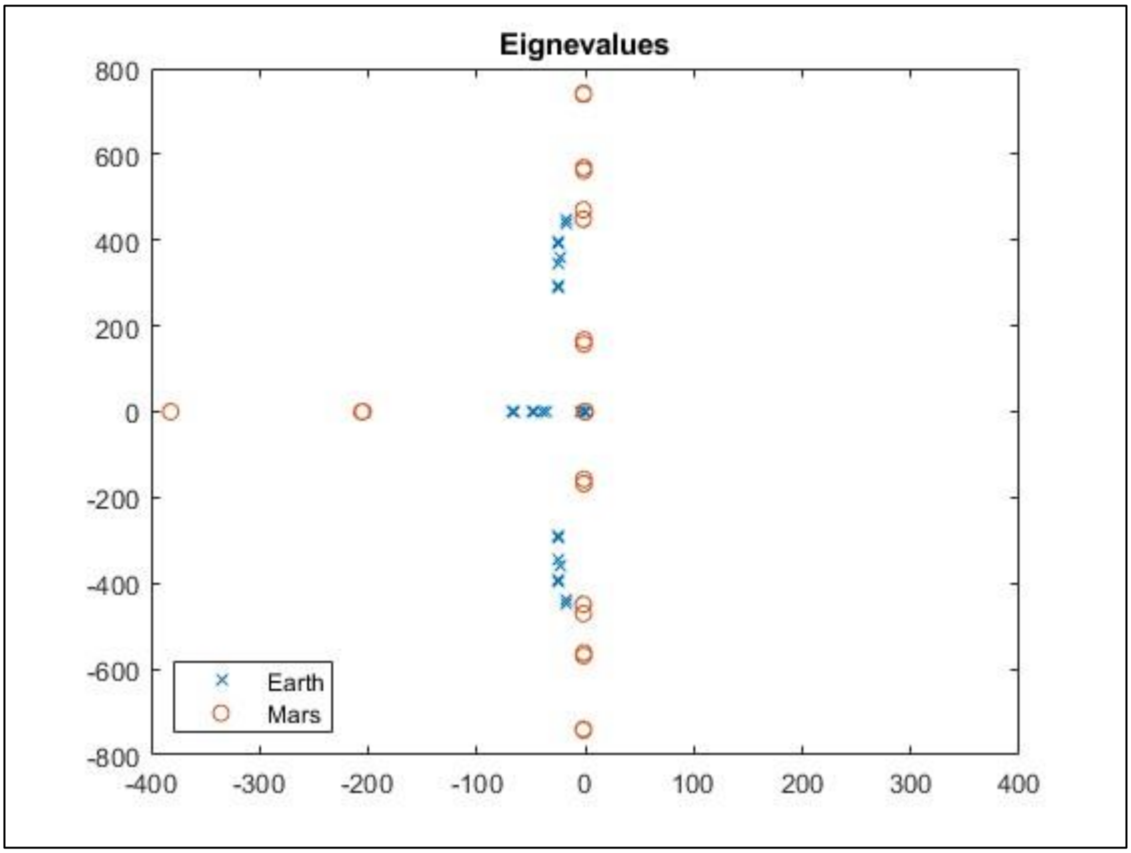

Figure 7.1: Eigenvalues when operating under Earth and Mars' atmospheric conditions

Figure 7.2 and Figure 7.3 shows the heave and yaw rate response of hexacopter in Mars and Earth's atmosphere. Both responses in Mars' atmosphere is very slightly damped compared to responses in the Earth's atmosphere. The slightly damped response in Mars compared to the response in Earth is confirmed by steep change in phase around the frequency of 450 rad/sec (Figure 7.2 Figure 7.3). The system response at Mars is not as sensitive to the input at the frequency range from 0.1 rad/sec to 400 rad/sec. As the system transition into the mid-range frequencies, the model in Earth is more responsive as there is a lower change in magnitude. At the higher frequency, the Mars' model predicts higher magnitude flapping modes due to decrease in density at Martian surface. Therefore, the flapping modes in Mars' atmosphere are higher in magnitude by 10 dB. The differences are further explained in the discussion section below.

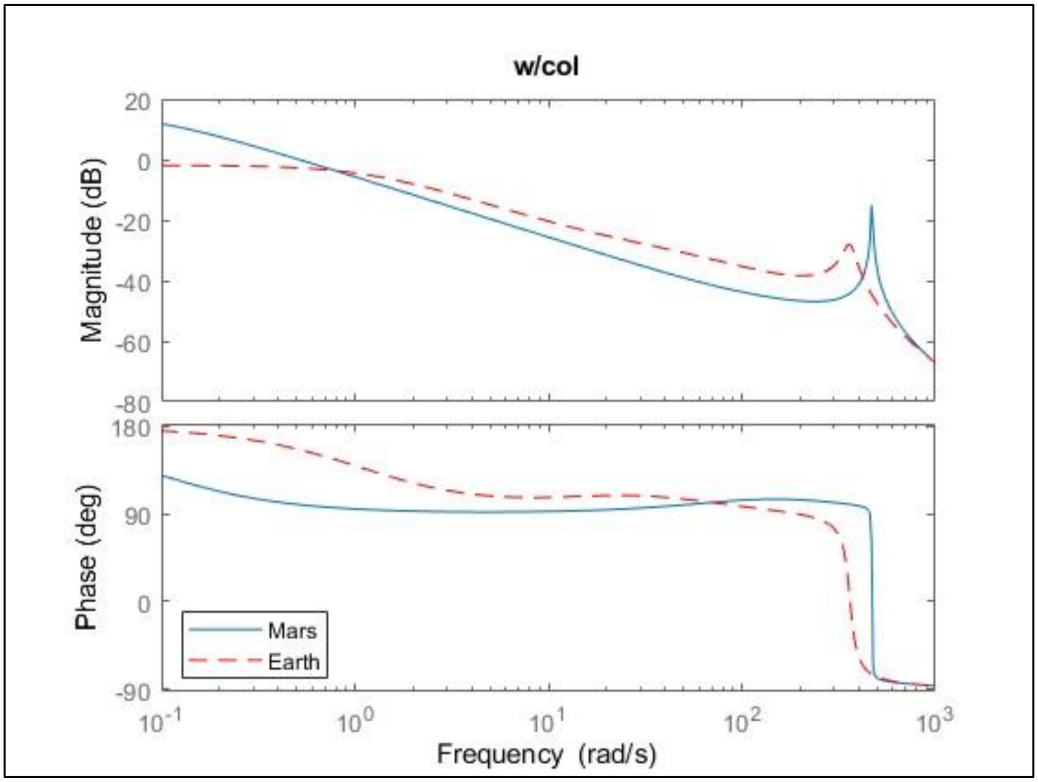

Figure 7.2: Heave response of the hexacopter in both Earth and Mars' atmosphere

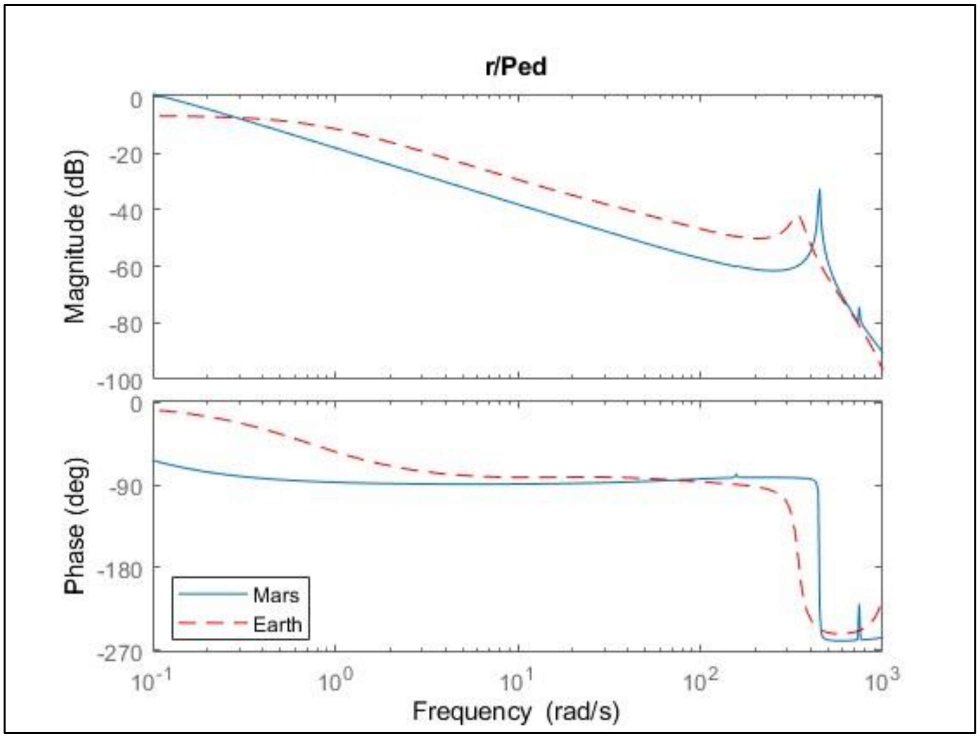

Figure 7.3: Yaw rate response compared between Earth and Mars' environment

A similar dynamic behavior difference is noticed for both pitch and roll rate as the heave and yaw rate response of the system. Specifically, the system is not as responsive at Mars atmospheric conditions than it is in Earth's atmosphere due to Mars' atmosphere being very thin. At 0.1 rad/sec frequency, the Mars' model reacts more like the model in Earth's atmosphere. The Mars' model becomes less responsive past 10 rad/sec frequency mark. Moreover, higher magnitude rotor modes exist in the high frequency domain. The modes are very slightly damped than they are in the Earth's atmosphere. Thus, the modes are more responsive in Mars' than Earth. The slightly damped modes are confirmed by not so gradual shift in phase for Mars' model, whereas the model operating in Earth's atmosphere is damped as the phase shift is very gradual. The phugoid mode in Mars is also at a lower frequency than Earth due to Mars gravity being 1% of Earth's atmosphere. Due to decrease in gravity, the damping parameter, i.e., M_q (equation 6.1) is negligible, thus making the system responsive to side gust in Mars' atmospheric conditions.

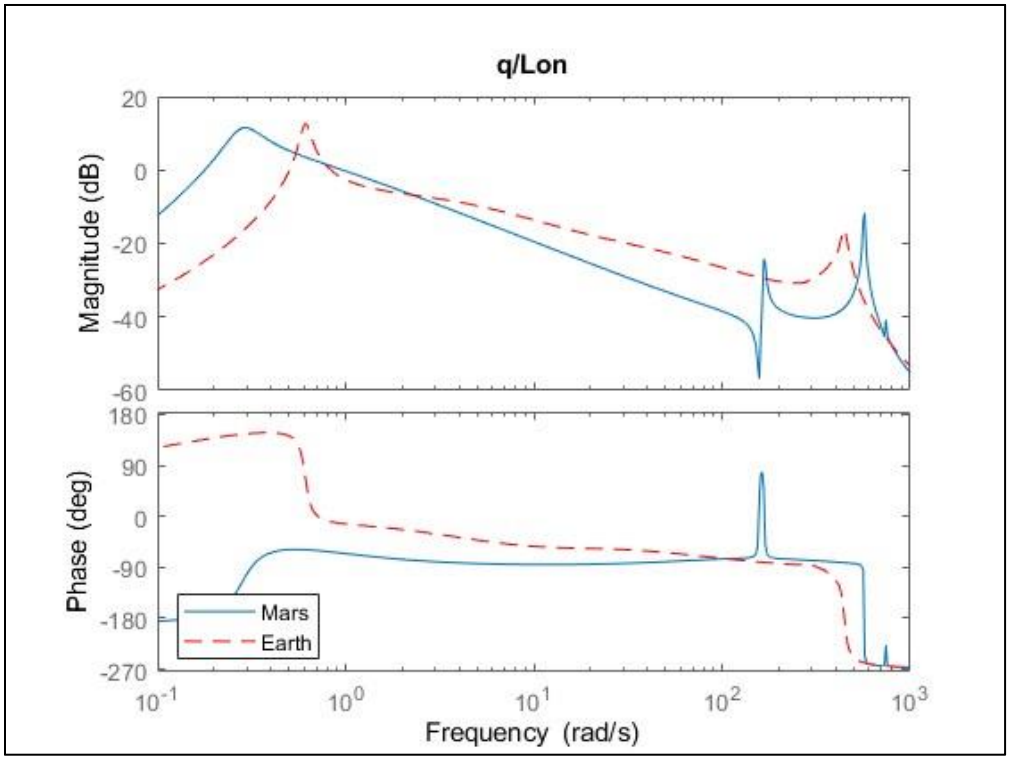

Figure 7.4: Pitch rate response comparison between Earth and Mars' environment

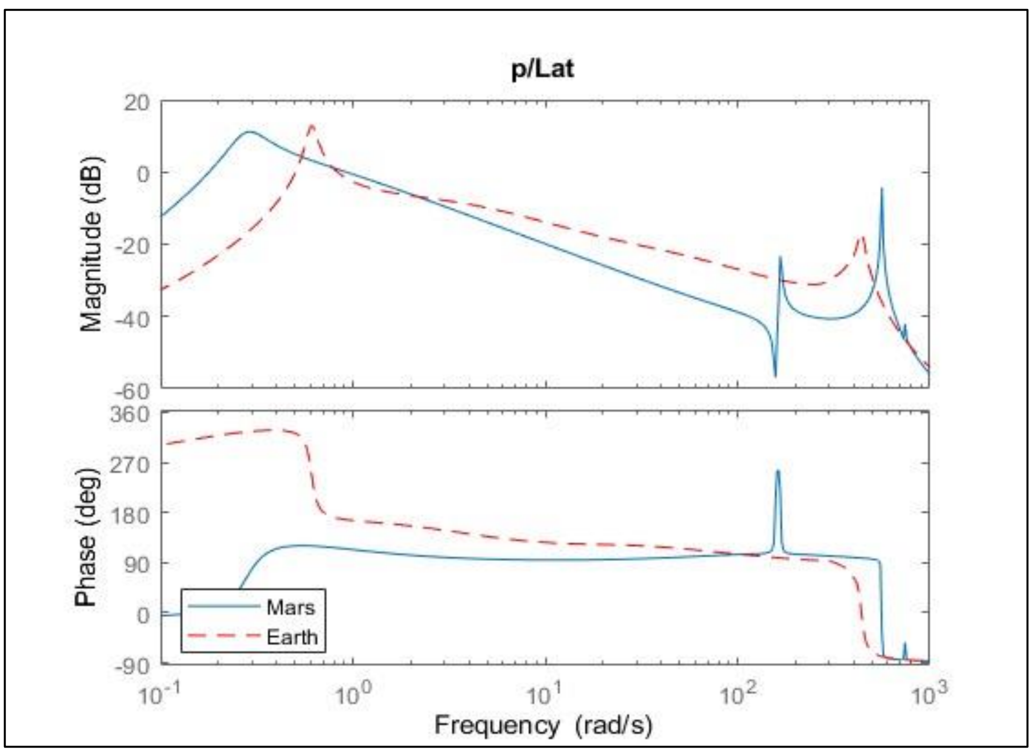

Figure 7.5: Roll rate response comparison between Earth and Mars' environment

Chapter 8. Discussion

As described before, the purpose of this project is to analyze the flight behavior differences of a hexacopter between the two environments. The comparison is needed to understand the feasibility of designing a dynamically matched surrogate helicopter to conduct flight testing on Earth. Based on the analysis conducted above, it is determined that bode plots are not sufficient to check if both systems are dynamically similar. Specifically, the linear model obtained from FLIGHTLAB predicts the pitch response of the system to longitudinal input in Earth's atmosphere being stable. Furthermore, the hexacopter in Earth's atmosphere is also a minimum phase system. Thus, one can predict the stability of the system in Earth's atmosphere by considering the gain and phase margin. In case of the hexacopter operating in Earth's atmosphere, the open loop predicts both gain and phase margin of 79 dB and 79 degrees respectively. In other words, the designed hexacopter will remain stable if the gain and phase margin is below 79 dB and 79 degrees respectively. In case of hexacopter operating in Mars' atmospheric conditions, FLIGHTLAB predicts the model to be unstable with non-minimum phase. Due to the model being unstable with non-minimum phase, bode plots along with stability margins are not informative. To determine if the system is stable, Nyquist stability criteria is applied to understand model's stability. In this project, Nichols charts are used to determine the stability of model. The Nyquist criteria is based on the number and direction of encirclements of the critical point. Figure 8.1 shows the pitch response to longitudinal input for hexacopter operating in both Earth and Mars' atmosphere. Since, bode plots with stability margins were sufficient in understanding the stability of the hexacopter in Earth's atmosphere, a Nicholas chart is used to understand the stability of hexacopter in Mars' atmosphere.

The model being modeled in this project is MIMO system, therefore, there exists four unstable eigenvalues. Assuming both pitch and roll can be stabilized independently, only two eigenvalues dominate per both pitch and roll response (np=2). Therefore, there exists two unstable poles for both pitch and roll responses. As seen in Figure 8.1, the Mars' curve makes two crossovers above the critical point: one above the critical point and one above the critical frequency. The two crossovers (N=-2) are equivalent to two counterclockwise encirclements of the critical point in the Nyquist plot. Furthermore, the Nyquist criteria also states that the number of zeros of the characteristic function Q(s)=1+L(s) in the right-hand plane is: Nz=N+np=-2+2=0. Since, the pitch response of the hexacopter in Mars' has zero numbers of zeros, the system is stable as zeros of function Q(s) equals the number of poles of T(s) in the RHP. Equation 8.1 states the transfer function of closed loop system showing numbers of zeros of Q(s) equals poles of T(s).

$$\mathrm{T(s)} = \frac{\mathrm{L}(s)}{1 + Q(s)} = \frac{\mathrm{L}(s)}{\mathrm{Q(s)}} \qquad 8.1$$

Even though the system is stable, the response system will still be oscillatory as the phase margin intersects the desirable stability margin block (Figure 8.1). The Nicholas plot gives phase margin of ~20.5 dB which is less than the desired phase margin of 45 degrees for the system to not be oscillatory.

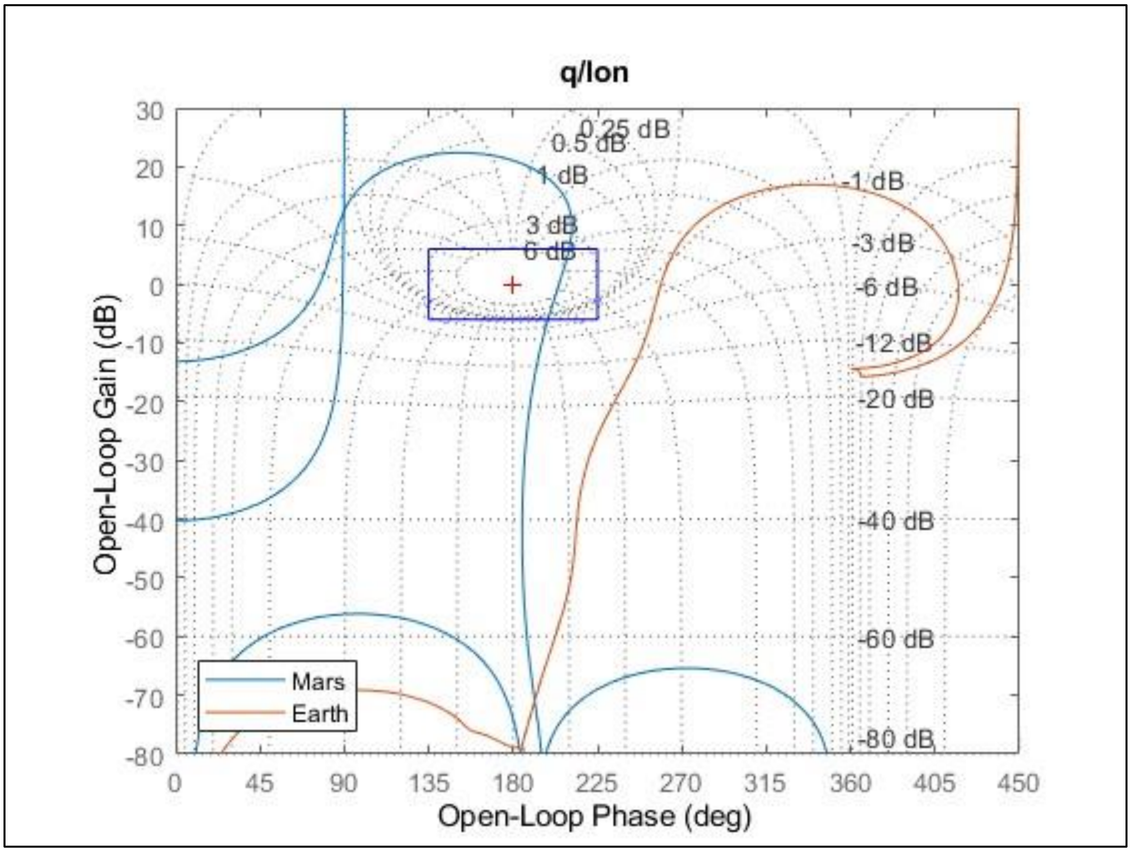

Figure 8.1: Nicholas chart (q/lon)

In addition to the pitch response of the system in both Earth and Mars' atmosphere, the roll response of the vehicle is also analyzed. Unlike the pitch response in Earth, the roll response in Earth is unstable with non-minimum phase. Therefore, Nyquist stability criteria must be applied in order to understand the roll stability of the vehicle. With the input same as the pitch response, the roll response is unstable as it gives two clockwise encirclements, thus adding two zeros in the right-hand plane. The phase of roll response can be converted into minimum phase by inverting the sign of input. Once the input is inverted, mirroring the roll response on Earth (Figure 8.2) about 180 degrees gives one crossover above the critical point and one above the critical frequency. Then the roll response of the hexacopter in Earth is stable as only two eigenvalues exist that dominates the roll response. The two counterclockwise encirclements of the critical point results in zero number of zeros of the characteristic function Q(s), thus the closed loop transfer function has zero number of poles in the right-hand plane.

Furthermore, the roll response of the hexacopter in Mars' predicts different behavior than pitch response of the hexacopter on Mars. Unlike pitch response, the roll response of the hexacopter on Mars' cannot be stabilized by only using the proportional gain technique. Closing the loop with just proportional gain only stabilizes one unstable pole as there exists only one counterclockwise encirclement, leaving one unstable pole in the right-hand side.

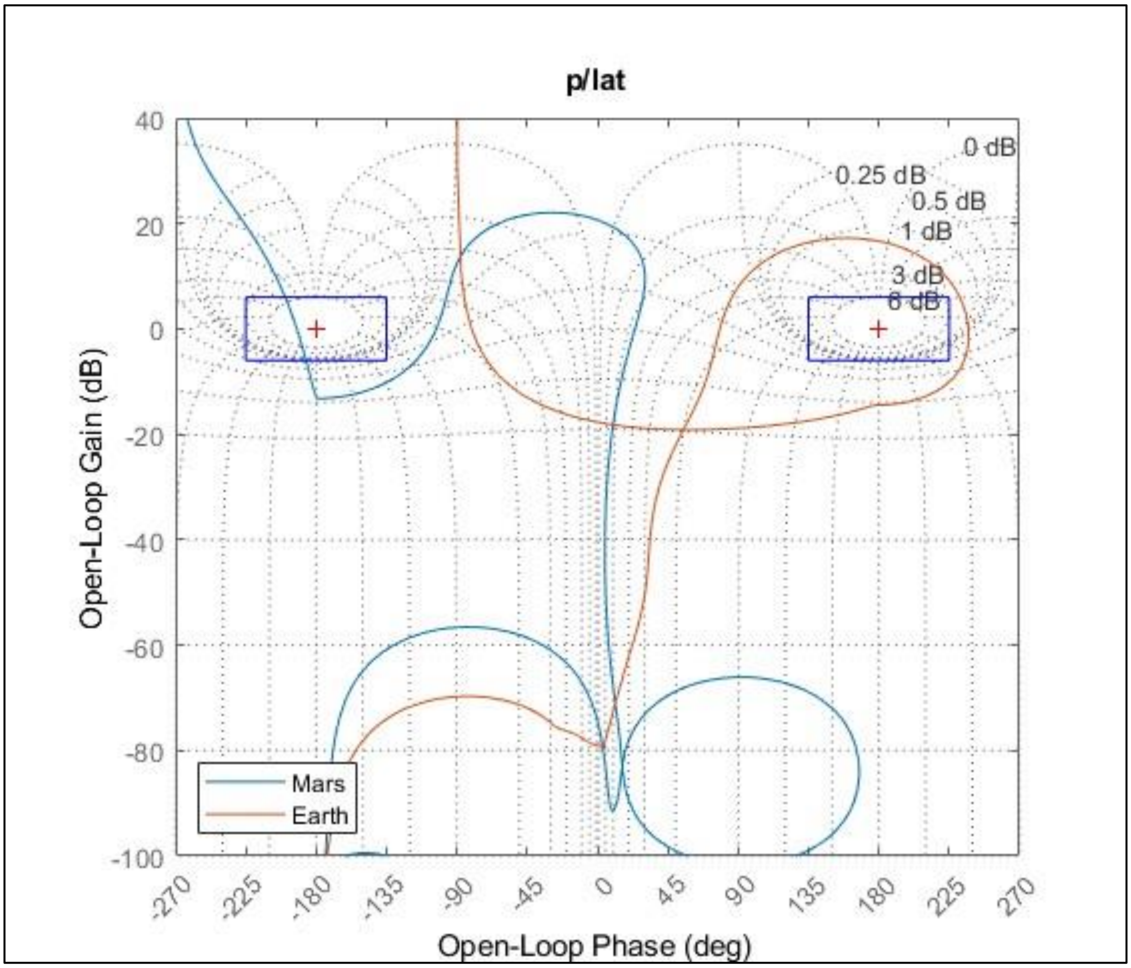

Figure 8.2: Nyquist plot (p/lat)

The flight behavior of the designed hexacopter differs significantly in both Earth and Mars environment. Specifically, it is easier to stabilize the pitch response of the vehicle on Earth than on Mars due to high gain and phase stability margins on Earth. The pitch response on Mars is oscillatory with very small phase margin allowability. In addition, the roll response of hexacopter is stable and unstable on Earth and Mars respectively. Based on the above analysis, proportional gain cannot be applied alone to stabilize both responses in both Earth and Mars as that would only decrease stability margins for both pitch and roll response of the hexacopter. Therefore, further analysis needs to be conducted to thoroughly understand the flight behavior differences between Earth and Mars. Further analysis is needed to determine if a dynamically matched surrogate model to conduct flight testing on Earth can be created.

Chapter 9. Conclusion

Comparing the fight behavior of the designed hexacopter in both Earth and Mars' atmosphere showed different flight characteristics. Specifically, the flight responses on Earth differs significantly than the responses on Mars. Below are some of the key findings from the conducted study.

- All obtained responses are first order responses as one would expect.
- The results obtained from FLIGHTLAB are valid as they match very closely with the results obtained from CAMRAD.
- Differences in results between CAMRAD and FLIGHTLAB occur due to not having inflow correction and using difference induced velocity techniques.
- The responses in Earth atmosphere are significantly more damped than the responses in Mars' atmosphere. The responses on Mars are not damped due to Mars' density being 1% of Earths.
- The designed hexacopter is fully stable in Earth's atmosphere than on Mars.
- Both pitch and roll rates are coupled due to the coupling between the horizontal speed rate and the attitude. The following coupling leads to phugoid mode in the low frequency domain.
- Nyquist stability criteria is used to determine the stability of both pitch and roll response of the hexacopter on Earth and Mars.
- Stability margins from bode plots are only informative when the system is stable and has minimum phase.
- It is certain that the technique of proportional gain is not sufficient to stabilize roll response of the designed hexacopter on Mars.

Overall, given the flight dynamics difference mentioned above, different control stabilizing techniques need to be explored such that the operating vehicle is stable in both roll and pitch when in hover. Thus, further analysis needs to be conducted to determine if a dynamically matched surrogate helicopter can be created to conduct flight testing on Earth.

Chapter 10. Future Work

In terms of the future work, several tasks need to be completed to reach to the conclusion if a dynamically matched surrogate helicopter can be created to conduct flight testing on Earth. The future tasks are as follows.

- Include inflow correction in the model
- Discover the reason for FLIGHTLAB not being able to trim the model without introducing artificial damping in Mars atmosphere.
- Re-trim the model without artificial damping and obtain linearize model.
- Set up forward flight configuration.
- Analyze forward flight configuration flight behavior in both Earth and Mars' environment.
- Reach to the conclusion if a dynamically matched surrogate helicopter can be created to conduct testing on Earth.

Completing the above tasks will assist in providing better understanding of the flight behavior differences in both Mars and Earth's atmospheric conditions. Understanding the flight behavior differences will help better predict a control system design that can help design a dynamically matched surrogate helicopter to conduct flight testing for Mars on Earth.

References

[1] Mars Exploration Program and the Jet Propulsion Laboratory for NASA's Science Mission Directorate, "NASA Science Mars Exploration Program," Jet Propulsion Laboratory , [Online]. Available: https://mars.nasa.gov/#red_planet/5. [Accessed 12 06 2022].

[2] Grip, H. F., Johnson, W., Malpica, C., Scharf ,D. P., Mandic, M., Young, L., Allan, B., Mettler, B. and Martin, M. S., "Flight Dynamics of Mars Helicopter," 43rd European Rotorcraft Forum, Milan, Italy, 2017.

[3] "MARS InSight Mission," NASA, [Online]. Available: https://mars.nasa.gov/insight/mission/science/results/. [Accessed 13 06 2022].

[4] Savu, G. and Trifu, O., "Photovltaic Rotorcraft For Mars Missions," Joint Conference and Exhibit, San Diego, 1995.

[5] Kroo, I. and Kunz, P., "Development of the Mesicopter: A Miniature Autonomous Rotorcraft," In Proc. American Helicopter Society Vertical Lift Aircraft Design Conf., San Francisco, 2000.

[6] Young, L. A., Chen, R. T. and Aiken, E. W., "Design Opportunites and Challenges in the Development of Vertical Lift Planetary Aerial Vehicles," American Helicopter Scoeity International Vertical Lift Airacraft Design Specialist's Meeting, San Francisco, 2000.

[7] Datta, A., Roget, B., Griffiths, D., Pugliese, G., Sitaraman, J., Bao, J., Liu, L. and Gamard, O., "Design of a Martian Autonomous Rotary-Wing Vehicle," *Journal of Aircraft ,* vol. 40, 2003.

[8] Lacerda, M., Park, D., Patel, S. and Schrage, D., "A Preliminary Systems Engineering Study on a Concept for Mars Exploration with an Unmanned Autonomous Vehicle and Ground Rover Configuration," AHS International 74th Annual Forum & Technology Display, Phoenix, 2018.

[9] Lacerda, M., Park, D., Patel, S. and Schrage, D., "A Preliminary systems Engineering Study on a Concept for Mars Exploration with an Unmanned Autonomous Vehicle and Ground Rover," in *American Helicopter Society 74th Annual Forum*, Phoenix, 2018.

[10] Fujita, K., Karaca, H. and Nagai, H., "Parametric Study of Mars Helicopter for Pit Crater Exploration," in *AIAA Paper No. 2020-1734*, 2020.

[11] Balaram, J., Daubar, J., Bapst, J. and Tzanetos, T., "HELICOPTERS ON MARS: COMPELLING SCIENCE OF EXTREME TERRAINS ENABLED BY AN AERIAL PLATFORM," in *Ninth International Conference on Mars 2019*, Pasadena, CA, 2019.

[12] Grip, H. F., Johnson, W., Malpica, C., Scharf, D. P., Mandic, M., Young, L., Allan, B., Mettler, B., Martin, M. S. and Lam, J., "Modelling and Identification of Hover Flight Dynamics for NASA's Mars Helicopter," *Journal of Guidance, Control, and Dynamics,* Vols. 43, Number 2, 2020.

[13] Grip, H. F., and et, a., "Flight Control System for NASA's Mars Helicopter," *AIAA Scitech Conference and Exhibition, AIAA Paper 2019-1289,* 2019.

[14] Grip, H. F., "Developing the Guidance, Navigation, and Control System for NASA's Mars Helicopter," in *Proceedings of the AAS Guidance, Navigation and Control Conference, AAS Paper 19-155*, Springfield,VA, 2019.

[15] Williams, D., "Mars Fact sheet," NASA Space Science Data Coorinated Archive, 2019. [Online]. Available: https://nssdc.gsfc.nasa.gov/planetary/factsheet/marsfact.html. [Accessed 08 06 2022].

[16] "Extreme Planet Takes its Toll," Mars Exploration Rover Mission:Spotlight , 12 June 2007. [Online]. Available: https://mars.nasa.gov/mer/spotlight/20070612.html. [Accessed 13 June 2022].

[17] Radotich, M., Maser, S. W., DeSouza, Z., Gelhar, S., and Gallagher, H., "A Study of Past, Present, and Future Mars Rotorcraft," San Jose, 2021.

[18] Grip, H. F., Scharf, D. P., Malpica, C., Johnson, W., Mandic, M., Singh, G. and Young, L., "Guidance and Control for a Mars Helicopter," in *2018 AIAA Guidance, Navigation, and Control Conference* , Kissimmee, Florida , 2018.

[19] Padfield, G. D., “Helicopter Flight Dynamics: The Theory and Applications of Flying Qualities and Simulation Modeling”, Reston,VA: AIAA, 1996.

[20] "Flightlab," Advanced Rotorcraft Technology, 2017. [Online]. Available: https://www.flightlab.com/aboutus.html. [Accessed 08 06 2022].

[21] Johnson, W., Maser, S. W., Young, L., Malpica, C., Koning, W. J., Kuang, W., Fehler, M., Tuano, A., Chan, A., Datta, A., Chi, C., Lumba, R., Escobar, Balaram, D., J., Tzanetos, T. and Grip, H. F., "Mars Science Helicopter Conceptual Design," NASA/TM-2020–220485, 2020.

[22] Advanced Rotorcraft Technology, INC, *FLIGHTLAB Theory Manual,* vol. one, Sunnyvale.

[23] Advanced Rotorcraft Technology, Inc, "FLIGHTLAB Theory Manual," vol. 2, 2018.

[24] Dymore User's Manual, [Online]. Available: https://www.dymoresolutions.com/AerodynamicProperties/UnsteadyAerodynamics.pdf. [Accessed 25 September 2022].

[25] Jhonson, W., "NDARC. NASA Design and Analysis of Rotorcraft," in *NASA TP 2015-218751*, 2015.

[26] Advanced Rotorcraft Technology, Inc, "Control System Graphical Editor Manual," Advanced Rotorcraft Technology, inc, Sunnyvale, 2018.

[27] Advanced Rotorcraft Technology, Inc, "FLIGHTLAB X-Analysis User Manual," Advanced Rotorcraft Technology, Inc, Sunnyvale, 2018.

[28] Jhonson, W., Rotorcraft Aeromechanics, New York: Cambridge University Press, 2013.

[29] Huang, J. and Peters, D., "Real-time solution of nonlinear potential flow equations for lifting rotors," *Chinese Journal of Aeronautics,* vol. 30, no. 3, pp. 871-890, 2017.

[30] NASA Glenn Research Center , "Mars Atmosphere Model," NASA, 13 May 2021. [Online]. Available: https://www.grc.nasa.gov/WWW/K-12/airplane/atmosmrm.html. [Accessed 07 August 2022].

[31] Maser, S. W., Johnson, W., Young, L., Koning, W., Kuang, W., Malpica, C., Balaram, J. and Tzanetos, T., "Mars Science Helicopter: Conceptual Design of the Next Generation of Mars Rotorcraft," 2020.

[32] Kaw, A., "Newton-Raphson Method of Solving Nonlinear Equations," 23 December 2009. [Online]. Available: http://mathforcollege.com/nm/mws/gen/03nle/mws_gen_nle_txt_newton.pdf. [Accessed 26 September 2022].

Appendix-A: Atmospheric Tables

!U	ft	slug/ft^3	lbf/ft^2	ft/sec	degR
-8000	0.002987	2805.104	1146.635	547.2105	-0.00357
-7743.55	0.002966	2780.508	1145.676	546.2953	-0.00357
-7487.1	0.002945	2756.088	1144.716	545.3801	-0.00357
-7230.65	0.002924	2731.842	1143.755	544.4649	-0.00357
-6974.19	0.002903	2707.769	1142.793	543.5497	-0.00357
-6717.74	0.002882	2683.869	1141.831	542.6345	-0.00357
-6461.29	0.002861	2660.141	1140.867	541.7194	-0.00357
-6204.84	0.002841	2636.584	1139.903	540.8043	-0.00357
-5948.39	0.00282	2613.197	1138.939	539.8892	-0.00357
-5691.94	0.0028	2589.978	1137.973	538.9741	-0.00357
-5435.48	0.00278	2566.928	1137.007	538.0591	-0.00357
-5179.03	0.00276	2544.044	1136.039	537.1441	-0.00357
-4922.58	0.00274	2521.326	1135.071	536.2291	-0.00357
-4666.13	0.00272	2498.774	1134.102	535.3141	-0.00357
-4409.68	0.0027	2476.386	1133.133	534.3991	-0.00357
-4153.23	0.00268	2454.161	1132.162	533.4842	-0.00357
-3896.77	0.002661	2432.098	1131.191	532.5693	-0.00357
-3640.32	0.002642	2410.197	1130.219	531.6544	-0.00357
-3383.87	0.002622	2388.457	1129.246	530.7395	-0.00357
-3127.42	0.002603	2366.876	1128.273	529.8247	-0.00357
-2870.97	0.002584	2345.453	1127.298	528.9099	-0.00357
-2614.52	0.002565	2324.189	1126.323	527.9951	-0.00357
-2358.07	0.002546	2303.082	1125.347	527.0803	-0.00357
-2101.61	0.002527	2282.13	1124.37	526.1655	-0.00357
-1845.16	0.002509	2261.334	1123.392	525.2508	-0.00357
-1588.71	0.00249	2240.692	1122.413	524.3361	-0.00357
-1332.26	0.002472	2220.203	1121.434	523.4214	-0.00357
-1075.81	0.002453	2199.867	1120.454	522.5067	-0.00357
-819.355	0.002435	2179.683	1119.473	521.5921	-0.00357
-562.903	0.002417	2159.649	1118.491	520.6775	-0.00357
-306.452	0.002399	2139.765	1117.508	519.7629	-0.00357
-50	0.002381	2120.03	1116.524	518.8483	-0.00357
0	0.002377	2116.2	1116.332	518.67	-0.00357
1164.169	0.002297	2028.593	1111.856	514.5186	-0.00357
2328.337	0.002219	1943.955	1107.362	510.3676	-0.00357
3492.506	0.002144	1862.21	1102.85	506.2171	-0.00357
4656.675	0.00207	1783.28	1098.32	502.0671	-0.00357
5820.843	0.001998	1707.09	1093.772	497.9175	-0.00357
6985.012	0.001928	1633.567	1089.205	493.7684	-0.00357

8149.181	0.00186	1562.637	1084.62	489.6197	-0.00357
9313.349	0.001793	1494.23	1080.015	485.4716	-0.00357
10477.52	0.001729	1428.276	1075.392	481.3238	-0.00357
11641.69	0.001666	1364.706	1070.749	477.1766	-0.00357
12805.86	0.001606	1303.455	1066.086	473.0298	-0.00357
13970.02	0.001546	1244.456	1061.403	468.8835	-0.00357
15134.19	0.001489	1187.645	1056.7	464.7376	-0.00357
16298.36	0.001433	1132.959	1051.977	460.5922	-0.00357
17462.53	0.001379	1080.336	1047.233	456.4472	-0.00357
18626.7	0.001327	1029.716	1042.468	452.3027	-0.00357
19790.87	0.001276	981.04	1037.681	448.1587	-0.00357
20955.04	0.001226	934.2495	1032.873	444.0152	-0.00357
22119.21	0.001178	889.288	1028.043	439.8721	-0.00357
23283.37	0.001131	846.1001	1023.19	435.7294	-0.00357
24447.54	0.001086	804.6313	1018.315	431.5873	-0.00357
25611.71	0.001043	764.8286	1013.417	427.4455	-0.00357
26775.88	0.001	726.6399	1008.496	423.3043	-0.00357
27940.05	0.000959	690.0145	1003.552	419.1635	-0.00357
29104.22	0.000919	654.9027	998.5829	415.0232	-0.00357
30268.39	0.000881	621.2558	993.59	410.8833	-0.00357
31432.55	0.000844	589.0264	988.5724	406.7439	-0.00357
32596.72	0.000808	558.1681	983.5298	402.605	-0.00357
33760.89	0.000773	528.6356	978.4618	398.4665	-0.00357
34925.06	0.000739	500.3847	973.3679	394.3285	-0.00357
36089.23	0.000707	473.3721	968.2479	390.1909	-0.00357
36089.25	0.000705	471.9545	967.9985	389.99	0
38177.06	0.000638	426.8524	967.9985	389.99	0
40264.86	0.000577	386.0605	967.9985	389.99	0
42352.67	0.000522	349.1669	967.9985	389.99	0
44440.47	0.000472	315.799	967.9985	389.99	0
46528.28	0.000427	285.6198	967.9985	389.99	0
48616.09	0.000386	258.3248	967.9985	389.99	0
50703.89	0.000349	233.6381	967.9985	389.99	0
52791.7	0.000316	211.3106	967.9985	389.99	0
54879.51	0.000286	191.1169	967.9985	389.99	0
56967.31	0.000258	172.8529	967.9985	389.99	0
59055.12	0.000234	156.3343	967.9985	389.99	0
61142.92	0.000211	141.3943	967.9985	389.99	0
63230.73	0.000191	127.8821	967.9985	389.99	0
65318.54	0.000173	115.6611	967.9985	389.99	0
67406.34	0.000156	104.608	967.9985	389.99	0
69494.15	0.000141	94.6112	967.9985	389.99	0
71581.96	0.000128	85.56974	967.9985	389.99	0

73669.76	0.000116	77.39232	967.9985	389.99	0
75757.57	0.000105	69.99637	967.9985	389.99	0
77845.38	9.46E-05	63.30721	967.9985	389.99	0
79933.18	8.55E-05	57.2573	967.9985	389.99	0
82020.99	7.74E-05	51.78554	967.9985	389.99	0
82021.01	7.74E-05	51.78554	967.9985	389.99	0.001646
86030.92	6.29E-05	42.83382	976.0901	396.5371	0.001646
90040.84	5.14E-05	35.54232	984.112	403.0818	0.001646
94050.75	4.21E-05	29.58287	992.0661	409.6239	0.001646
98060.67	3.46E-05	24.69605	999.9539	416.1635	0.001646
102070.6	2.85E-05	20.676	1007.777	422.7006	0.001646
106080.5	2.36E-05	17.35876	1015.537	429.2352	0.001646
110090.4	1.95E-05	14.61325	1023.235	435.7674	0.001646
114100.3	1.62E-05	12.33433	1030.872	442.297	0.001646
118110.2	1.36E-05	10.43736	1038.451	448.8241	0.001646
122120.2	1.13E-05	8.854015	1045.972	455.3487	0.001646
126130.1	9.5E-06	7.528927	1053.436	461.8709	0.001646
130140	7.98E-06	6.41711	1060.845	468.3905	0.001646
134149.9	6.73E-06	5.4819	1068.2	474.9076	0.001646
138159.8	5.68E-06	4.693327	1075.502	481.4223	0.001646
142169.7	4.81E-06	4.026821	1082.751	487.9345	0.001646
146179.6	4.08E-06	3.462188	1089.95	494.4442	0.001646
150189.6	3.47E-06	2.982784	1097.099	500.9514	0.001646
154199.5	2.96E-06	2.574854	1104.199	507.4561	0.001646
154199.5	2.84E-06	2.469334	1104.199	507.4561	0
155989	2.65E-06	2.311237	1104.199	507.4561	0
157778.6	2.48E-06	2.163262	1104.199	507.4561	0
159568.1	2.32E-06	2.024761	1104.199	507.4561	0
161357.7	2.18E-06	1.895127	1104.199	507.4561	0
163147.2	2.04E-06	1.773793	1104.199	507.4561	0
164936.8	1.91E-06	1.660227	1104.199	507.4561	0
166726.3	1.78E-06	1.553933	1104.199	507.4561	0
168515.9	1.67E-06	1.454443	1104.199	507.4561	0
170305.4	1.56E-06	1.361324	1104.199	507.4561	0
172095	1.46E-06	1.274166	1104.199	507.4561	0
173884.5	1.37E-06	1.192589	1104.199	507.4561	0
173884.5	1.37E-06	1.192589	1104.199	507.4561	-0.00247
184903.8	9.58E-07	0.790324	1074.709	480.7129	-0.00247
195923	6.57E-07	0.511791	1044.419	453.9978	-0.00247
206942.3	4.4E-07	0.322959	1013.257	427.3106	-0.00247
217961.5	2.88E-07	0.19794	981.1406	400.6513	-0.00247
228980.8	1.83E-07	0.11736	947.9716	374.0199	-0.00247
240000	1.12E-07	0.066988	913.6357	347.4163	-0.00247

Appendix B: Mars Atmospheric Table

-26246.7	6.23666E-05	32.13006	814.5099	448.3732	0.000548
-25996.7	6.19195E-05	31.88999	814.3855	448.2362	0.000548
-25746.7	6.14756E-05	31.65171	814.261	448.0992	0.000548
-25496.7	6.10349E-05	31.41521	814.1365	447.9622	0.000548
-25246.7	6.05974E-05	31.18047	814.012	447.8252	0.000548
-24996.7	6.0163E-05	30.94749	813.8875	447.6882	0.000548
-24746.7	5.97318E-05	30.71626	813.763	447.5512	0.000548
-24496.7	5.93036E-05	30.48675	813.6384	447.4142	0.000548
-24246.7	5.88785E-05	30.25895	813.5138	447.2772	0.000548
-23996.7	5.84565E-05	30.03286	813.3892	447.1402	0.000548
-23746.7	5.80375E-05	29.80845	813.2646	447.0032	0.000548
-23496.7	5.76215E-05	29.58573	813.14	446.8662	0.000548
-23246.7	5.72085E-05	29.36466	813.0153	446.7292	0.000548
-22996.7	5.67985E-05	29.14525	812.8907	446.5922	0.000548
-22746.7	5.63914E-05	28.92748	812.766	446.4552	0.000548
-22496.7	5.59872E-05	28.71133	812.6412	446.3182	0.000548
-22246.7	5.55859E-05	28.49681	812.5165	446.1812	0.000548
-21996.7	5.51875E-05	28.28388	812.3918	446.0442	0.000548
-21746.7	5.4792E-05	28.07254	812.267	445.9072	0.000548
-21496.7	5.43993E-05	27.86279	812.1422	445.7702	0.000548
-21246.7	5.40095E-05	27.6546	812.0174	445.6332	0.000548
-20996.7	5.36224E-05	27.44796	811.8926	445.4962	0.000548
-20746.7	5.32381E-05	27.24287	811.7677	445.3592	0.000548
-20496.7	5.28566E-05	27.03932	811.6429	445.2222	0.000548
-20246.7	5.24778E-05	26.83728	811.518	445.0852	0.000548
-19996.7	5.21017E-05	26.63675	811.3931	444.9482	0.000548
-19746.7	5.17283E-05	26.43772	811.2681	444.8112	0.000548
-19496.7	5.13576E-05	26.24018	811.1432	444.6742	0.000548
-19246.7	5.09896E-05	26.04412	811.0182	444.5372	0.000548
-18996.7	5.06242E-05	25.84952	810.8933	444.4002	0.000548
-18746.7	5.02614E-05	25.65637	810.7683	444.2632	0.000548
-18496.7	4.99013E-05	25.46467	810.6432	444.1262	0.000548
-18246.7	4.95437E-05	25.2744	810.5182	443.9892	0.000548
-17996.7	4.91887E-05	25.08555	810.3931	443.8522	0.000548
-17746.7	4.88362E-05	24.89811	810.2681	443.7152	0.000548
-17496.7	4.84863E-05	24.71207	810.143	443.5782	0.000548
-17246.7	4.81389E-05	24.52743	810.0178	443.4412	0.000548
-16996.7	4.77939E-05	24.34416	809.8927	443.3042	0.000548
-16746.7	4.74515E-05	24.16226	809.7675	443.1672	0.000548
-16496.7	4.71115E-05	23.98172	809.6424	443.0302	0.000548

-16246.7	4.6774E-05	23.80253	809.5172	442.8932	0.000548
-15996.7	4.64388E-05	23.62468	809.392	442.7562	0.000548
-15746.7	4.61061E-05	23.44816	809.2667	442.6192	0.000548
-15496.7	4.57758E-05	23.27295	809.1415	442.4822	0.000548
-15246.7	4.54478E-05	23.09906	809.0162	442.3452	0.000548
-14996.7	4.51222E-05	22.92646	808.8909	442.2082	0.000548
-14746.7	4.47989E-05	22.75516	808.7656	442.0712	0.000548
-14496.7	4.4478E-05	22.58513	808.6403	441.9342	0.000548
-14246.7	4.41593E-05	22.41638	808.5149	441.7972	0.000548
-13996.7	4.3843E-05	22.24888	808.3896	441.6602	0.000548
-13746.7	4.35289E-05	22.08264	808.2642	441.5232	0.000548
-13496.7	4.3217E-05	21.91764	808.1388	441.3862	0.000548
-13246.7	4.29074E-05	21.75387	808.0133	441.2492	0.000548
-12996.7	4.26001E-05	21.59133	807.8879	441.1122	0.000548
-12746.7	4.22949E-05	21.43	807.7624	440.9752	0.000548
-12496.7	4.19919E-05	21.26988	807.6369	440.8382	0.000548
-12246.7	4.16911E-05	21.11095	807.5114	440.7012	0.000548
-11996.7	4.13925E-05	20.95321	807.3859	440.5642	0.000548
-11746.7	4.1096E-05	20.79665	807.2604	440.4272	0.000548
-11496.7	4.08016E-05	20.64126	807.1348	440.2902	0.000548
-11246.7	4.05093E-05	20.48703	807.0092	440.1532	0.000548
-10996.7	4.02192E-05	20.33395	806.8836	440.0162	0.000548
-10746.7	3.99311E-05	20.18201	806.758	439.8792	0.000548
-10496.7	3.96451E-05	20.03122	806.6324	439.7422	0.000548
-10246.7	3.93611E-05	19.88154	806.5067	439.6052	0.000548
-9996.71	3.90792E-05	19.73299	806.381	439.4682	0.000548
-9746.71	3.87993E-05	19.58555	806.2553	439.3312	0.000548
-9496.71	3.85214E-05	19.4392	806.1296	439.1942	0.000548
-9246.71	3.82455E-05	19.29395	806.0038	439.0572	0.000548
-8996.71	3.79716E-05	19.14979	805.8781	438.9202	0.000548
-8746.71	3.76996E-05	19.00671	805.7523	438.7832	0.000548
-8496.71	3.74296E-05	18.86469	805.6265	438.6462	0.000548
-8246.71	3.71615E-05	18.72373	805.5007	438.5092	0.000548
-7996.71	3.68954E-05	18.58383	805.3749	438.3722	0.000548
-7746.71	3.66312E-05	18.44497	805.249	438.2352	0.000548
-7496.71	3.63688E-05	18.30715	805.1231	438.0982	0.000548
-7246.71	3.61084E-05	18.17036	804.9972	437.9612	0.000548
-6996.71	3.58498E-05	18.03459	804.8713	437.8242	0.000548
-6746.71	3.55931E-05	17.89984	804.7454	437.6872	0.000548
-6496.71	3.53382E-05	17.76609	804.6194	437.5502	0.000548
-6246.71	3.50851E-05	17.63335	804.4934	437.4132	0.000548
-5996.71	3.48339E-05	17.50159	804.3674	437.2762	0.000548
-5746.71	3.45844E-05	17.37082	804.2414	437.1392	0.000548

-5496.71	3.43368E-05	17.24103	804.1154	437.0022	0.000548
-5246.71	3.40909E-05	17.1122	803.9893	436.8652	0.000548
-4996.71	3.38468E-05	16.98434	803.8633	436.7282	0.000548
-4746.71	3.36044E-05	16.85743	803.7372	436.5912	0.000548
-4496.71	3.33638E-05	16.73148	803.6111	436.4542	0.000548
-4246.71	3.31249E-05	16.60646	803.4849	436.3172	0.000548
-3996.71	3.28877E-05	16.48238	803.3588	436.1802	0.000548
-3746.71	3.26522E-05	16.35922	803.2326	436.0432	0.000548
-3496.71	3.24185E-05	16.23699	803.1064	435.9062	0.000548
-3246.71	3.21863E-05	16.11566	802.9802	435.7692	0.000548
-2996.71	3.19559E-05	15.99525	802.854	435.6322	0.000548
-2746.71	3.17271E-05	15.87573	802.7277	435.4952	0.000548
-2496.71	3.14999E-05	15.75711	802.6014	435.3582	0.000548
-2246.71	3.12744E-05	15.63937	802.4751	435.2212	0.000548
-1996.71	3.10505E-05	15.52252	802.3488	435.0842	0.000548
-1746.71	3.08282E-05	15.40653	802.2225	434.9472	0.000548
-1496.71	3.06075E-05	15.29142	802.0961	434.8102	0.000548
-1246.71	3.03884E-05	15.17716	801.9698	434.6732	0.000548
-996.709	3.01708E-05	15.06376	801.8434	434.5362	0.000548
-746.709	2.99548E-05	14.9512	801.717	434.3992	0.000548
-496.709	2.97404E-05	14.83949	801.5905	434.2622	0.000548
-246.709	2.95275E-05	14.72861	801.4641	434.1252	0.000548
0	2.93189E-05	14.62	801.3393	433.99	0.000548
91.86	2.92416E-05	14.57977	801.2928	433.9397	0.000548
183.727	2.91645E-05	14.53964	801.2463	433.8893	0.000548
275.587	2.90876E-05	14.49963	801.1998	433.839	0.000548
367.4517	2.90109E-05	14.45972	801.1533	433.7886	0.000548
459.3152	2.89345E-05	14.41993	801.1069	433.7383	0.000548
551.1788	2.88582E-05	14.38024	801.0604	433.688	0.000548
643.0423	2.87821E-05	14.34066	801.0139	433.6376	0.000548
734.9058	2.87062E-05	14.3012	800.9674	433.5873	0.000548
826.7693	2.86305E-05	14.26184	800.9209	433.5369	0.000548
918.6328	2.85551E-05	14.22259	800.8744	433.4866	0.000548
1010.496	2.84798E-05	14.18345	800.8279	433.4362	0.000548
1102.36	2.84047E-05	14.14441	800.7814	433.3859	0.000548
1194.223	2.83298E-05	14.10549	800.7349	433.3356	0.000548
1286.087	2.82551E-05	14.06667	800.6883	433.2852	0.000548
1377.95	2.81806E-05	14.02795	800.6418	433.2349	0.000548
1469.814	2.81063E-05	13.98935	800.5953	433.1845	0.000548
1561.677	2.80323E-05	13.95085	800.5488	433.1342	0.000548
1653.541	2.79584E-05	13.91245	800.5023	433.0839	0.000548
1745.404	2.78847E-05	13.87416	800.4557	433.0335	0.000548
1837.268	2.78111E-05	13.83598	800.4092	432.9832	0.000548

1929.131	2.77378E-05	13.7979	800.3627	432.9328	0.000548
2020.995	2.76647E-05	13.75993	800.3161	432.8825	0.000548
2112.859	2.75918E-05	13.72206	800.2696	432.8322	0.000548
2204.722	2.7519E-05	13.68429	800.2231	432.7818	0.000548
2296.586	2.74465E-05	13.64663	800.1765	432.7315	0.000548
2388.449	2.73742E-05	13.60908	800.13	432.6811	0.000548
2480.313	2.7302E-05	13.57162	800.0834	432.6308	0.000548
2572.176	2.723E-05	13.53427	800.0369	432.5804	0.000548
2664.04	2.71582E-05	13.49702	799.9903	432.5301	0.000548
2755.903	2.70867E-05	13.45988	799.9438	432.4798	0.000548
2847.767	2.70153E-05	13.42284	799.8972	432.4294	0.000548
2939.63	2.6944E-05	13.3859	799.8506	432.3791	0.000548
3031.494	2.6873E-05	13.34906	799.8041	432.3287	0.000548
3123.357	2.68022E-05	13.31232	799.7575	432.2784	0.000548
3215.221	2.67315E-05	13.27568	799.7109	432.2281	0.000548
3307.084	2.66611E-05	13.23914	799.6644	432.1777	0.000548
3398.948	2.65908E-05	13.20271	799.6178	432.1274	0.000548
3490.811	2.65207E-05	13.16637	799.5712	432.077	0.000548
3582.675	2.64508E-05	13.13014	799.5246	432.0267	0.000548
3674.538	2.63811E-05	13.094	799.4781	431.9764	0.000548
3766.402	2.63115E-05	13.05797	799.4315	431.926	0.000548
3858.265	2.62422E-05	13.02203	799.3849	431.8757	0.000548
3950.129	2.6173E-05	12.98619	799.3383	431.8253	0.000548
4041.992	2.6104E-05	12.95045	799.2917	431.775	0.000548
4133.856	2.60352E-05	12.91481	799.2451	431.7246	0.000548
4225.719	2.59666E-05	12.87927	799.1985	431.6743	0.000548
4317.583	2.58981E-05	12.84382	799.1519	431.624	0.000548
4409.446	2.58299E-05	12.80848	799.1053	431.5736	0.000548
4501.31	2.57618E-05	12.77322	799.0587	431.5233	0.000548
4593.173	2.56939E-05	12.73807	799.0121	431.4729	0.000548
4685.037	2.56262E-05	12.70301	798.9655	431.4226	0.000548
4776.9	2.55586E-05	12.66805	798.9189	431.3723	0.000548
4868.764	2.54913E-05	12.63319	798.8722	431.3219	0.000548
4960.628	2.54241E-05	12.59842	798.8256	431.2716	0.000548
5052.491	2.53571E-05	12.56375	798.779	431.2212	0.000548
5144.355	2.52902E-05	12.52917	798.7324	431.1709	0.000548
5236.218	2.52236E-05	12.49469	798.6857	431.1206	0.000548
5328.082	2.51571E-05	12.46031	798.6391	431.0702	0.000548
5419.945	2.50908E-05	12.42601	798.5925	431.0199	0.000548
5511.809	2.50247E-05	12.39182	798.5458	430.9695	0.000548
5603.672	2.49587E-05	12.35771	798.4992	430.9192	0.000548
5695.536	2.48929E-05	12.3237	798.4525	430.8688	0.000548
5787.399	2.48273E-05	12.28979	798.4059	430.8185	0.000548

5879.263	2.47619E-05	12.25596	798.3593	430.7682	0.000548
5971.126	2.46966E-05	12.22223	798.3126	430.7178	0.000548
6062.99	2.46315E-05	12.1886	798.2659	430.6675	0.000548
6154.853	2.45666E-05	12.15505	798.2193	430.6171	0.000548
6246.717	2.45019E-05	12.1216	798.1726	430.5668	0.000548
6338.58	2.44373E-05	12.08824	798.126	430.5165	0.000548
6430.444	2.43729E-05	12.05497	798.0793	430.4661	0.000548
6522.307	2.43087E-05	12.02179	798.0326	430.4158	0.000548
6614.171	2.42446E-05	11.98871	797.986	430.3654	0.000548
6706.034	2.41807E-05	11.95572	797.9393	430.3151	0.000548
6797.898	2.4117E-05	11.92281	797.8926	430.2648	0.000548
6889.761	2.40534E-05	11.89	797.8459	430.2144	0.000548
6981.625	2.399E-05	11.85728	797.7993	430.1641	0.000548
7073.488	2.39268E-05	11.82464	797.7526	430.1137	0.000548
7165.352	2.38637E-05	11.7921	797.7059	430.0634	0.000548
7257.215	2.38009E-05	11.75965	797.6592	430.013	0.000548
7349.079	2.37381E-05	11.72728	797.6125	429.9627	0.000548
7440.942	2.36756E-05	11.69501	797.5658	429.9124	0.000548
7532.806	2.36132E-05	11.66282	797.5191	429.862	0.000548
7624.669	2.3551E-05	11.63073	797.4724	429.8117	0.000548
7716.533	2.34889E-05	11.59872	797.4257	429.7613	0.000548
7808.397	2.3427E-05	11.5668	797.379	429.711	0.000548
7900.26	2.33653E-05	11.53496	797.3323	429.6607	0.000548
7992.124	2.33037E-05	11.50322	797.2856	429.6103	0.000548
8083.987	2.32423E-05	11.47156	797.2389	429.56	0.000548
8175.851	2.3181E-05	11.43999	797.1922	429.5096	0.000548
8267.714	2.31199E-05	11.4085	797.1454	429.4593	0.000548
8359.578	2.3059E-05	11.37711	797.0987	429.409	0.000548
8451.441	2.29982E-05	11.3458	797.052	429.3586	0.000548
8543.305	2.29376E-05	11.31457	797.0053	429.3083	0.000548
8635.168	2.28772E-05	11.28343	796.9585	429.2579	0.000548
8727.032	2.28169E-05	11.25238	796.9118	429.2076	0.000548
8818.895	2.27568E-05	11.22141	796.8651	429.1572	0.000548
8910.759	2.26968E-05	11.19053	796.8183	429.1069	0.000548
9002.622	2.2637E-05	11.15973	796.7716	429.0566	0.000548
9094.486	2.25774E-05	11.12902	796.7248	429.0062	0.000548
9186.349	2.25179E-05	11.09839	796.6781	428.9559	0.000548
9278.213	2.24585E-05	11.06785	796.6313	428.9055	0.000548
9370.076	2.23994E-05	11.03739	796.5846	428.8552	0.000548
9461.94	2.23403E-05	11.00701	796.5378	428.8049	0.000548
9553.803	2.22815E-05	10.97672	796.4911	428.7545	0.000548
9645.667	2.22228E-05	10.94651	796.4443	428.7042	0.000548
9737.53	2.21642E-05	10.91638	796.3976	428.6538	0.000548

9829.394	2.21058E-05	10.88634	796.3508	428.6035	0.000548
9921.257	2.20475E-05	10.85638	796.304	428.5532	0.000548
10013.12	2.19895E-05	10.8265	796.2573	428.5028	0.000548
10104.98	2.19315E-05	10.7967	796.2105	428.4525	0.000548
10196.85	2.18737E-05	10.76699	796.1637	428.4021	0.000548
10288.71	2.18161E-05	10.73736	796.1169	428.3518	0.000548
10380.57	2.17586E-05	10.70781	796.0701	428.3014	0.000548
10472.44	2.17013E-05	10.67834	796.0234	428.2511	0.000548
10564.3	2.16441E-05	10.64895	795.9766	428.2008	0.000548
10656.17	2.15871E-05	10.61964	795.9298	428.1504	0.000548
10748.03	2.15302E-05	10.59042	795.883	428.1001	0.000548
10839.89	2.14735E-05	10.56127	795.8362	428.0497	0.000548
10931.76	2.14169E-05	10.53221	795.7894	427.9994	0.000548
11023.62	2.13604E-05	10.50322	795.7426	427.9491	0.000548
11115.48	2.13042E-05	10.47431	795.6958	427.8987	0.000548
11207.35	2.1248E-05	10.44549	795.649	427.8484	0.000548
11299.21	2.11921E-05	10.41674	795.6022	427.798	0.000548
11391.07	2.11362E-05	10.38807	795.5554	427.7477	0.000548
11482.94	2.10805E-05	10.35948	795.5085	427.6974	0.000548
11574.8	2.1025E-05	10.33097	795.4617	427.647	0.000548
11666.66	2.09696E-05	10.30254	795.4149	427.5967	0.000548
11758.53	2.09143E-05	10.27419	795.3681	427.5463	0.000548
11850.39	2.08592E-05	10.24591	795.3212	427.496	0.000548
11942.25	2.08043E-05	10.21771	795.2744	427.4456	0.000548
12034.12	2.07495E-05	10.18959	795.2276	427.3953	0.000548
12125.98	2.06948E-05	10.16155	795.1808	427.345	0.000548
12217.85	2.06403E-05	10.13358	795.1339	427.2946	0.000548
12309.71	2.05859E-05	10.1057	795.0871	427.2443	0.000548
12401.57	2.05317E-05	10.07788	795.0402	427.1939	0.000548
12493.44	2.04776E-05	10.05015	794.9934	427.1436	0.000548
12585.3	2.04236E-05	10.02249	794.9465	427.0933	0.000548
12677.16	2.03698E-05	9.994906	794.8997	427.0429	0.000548
12769.03	2.03162E-05	9.967399	794.8528	426.9926	0.000548
12860.89	2.02626E-05	9.939968	794.806	426.9422	0.000548
12952.75	2.02092E-05	9.912612	794.7591	426.8919	0.000548
13044.62	2.0156E-05	9.885331	794.7123	426.8415	0.000548
13136.48	2.01029E-05	9.858126	794.6654	426.7912	0.000548
13228.34	2.00499E-05	9.830995	794.6185	426.7409	0.000548
13320.21	1.99971E-05	9.803939	794.5716	426.6905	0.000548
13412.07	1.99444E-05	9.776957	794.5248	426.6402	0.000548
13503.93	1.98919E-05	9.75005	794.4779	426.5898	0.000548
13595.8	1.98395E-05	9.723217	794.431	426.5395	0.000548
13687.66	1.97872E-05	9.696457	794.3841	426.4892	0.000548

13779.53	1.97351E-05	9.669772	794.3373	426.4388	0.000548
13871.39	1.96831E-05	9.643159	794.2904	426.3885	0.000548
13963.25	1.96313E-05	9.61662	794.2435	426.3381	0.000548
14055.12	1.95795E-05	9.590154	794.1966	426.2878	0.000548
14146.98	1.9528E-05	9.563761	794.1497	426.2375	0.000548
14238.84	1.94765E-05	9.537441	794.1028	426.1871	0.000548
14330.71	1.94252E-05	9.511193	794.0559	426.1368	0.000548
14422.57	1.9374E-05	9.485017	794.009	426.0864	0.000548
14514.43	1.9323E-05	9.458913	793.9621	426.0361	0.000548
14606.3	1.92721E-05	9.432881	793.9152	425.9857	0.000548
14698.16	1.92213E-05	9.406921	793.8683	425.9354	0.000548
14790.02	1.91707E-05	9.381032	793.8213	425.8851	0.000548
14881.89	1.91202E-05	9.355214	793.7744	425.8347	0.000548
14973.75	1.90698E-05	9.329467	793.7275	425.7844	0.000548
15065.61	1.90196E-05	9.303792	793.6806	425.734	0.000548
15157.48	1.89695E-05	9.278187	793.6337	425.6837	0.000548
15249.34	1.89195E-05	9.252652	793.5867	425.6334	0.000548
15341.2	1.88697E-05	9.227188	793.5398	425.583	0.000548
15433.07	1.882E-05	9.201793	793.4929	425.5327	0.000548
15524.93	1.87704E-05	9.176469	793.4459	425.4823	0.000548
15616.8	1.8721E-05	9.151214	793.399	425.432	0.000548
15708.66	1.86717E-05	9.126029	793.352	425.3817	0.000548
15800.52	1.86225E-05	9.100913	793.3051	425.3313	0.000548
15892.39	1.85734E-05	9.075867	793.2581	425.281	0.000548
15984.25	1.85245E-05	9.050889	793.2112	425.2306	0.000548
16076.11	1.84757E-05	9.02598	793.1642	425.1803	0.000548
16167.98	1.8427E-05	9.001139	793.1173	425.1299	0.000548
16259.84	1.83785E-05	8.976367	793.0703	425.0796	0.000548
16351.7	1.83301E-05	8.951663	793.0234	425.0293	0.000548
16443.57	1.82818E-05	8.927027	792.9764	424.9789	0.000548
16535.43	1.82337E-05	8.902459	792.9294	424.9286	0.000548
16627.29	1.81856E-05	8.877959	792.8825	424.8782	0.000548
16719.16	1.81377E-05	8.853525	792.8355	424.8279	0.000548
16811.02	1.809E-05	8.829159	792.7885	424.7776	0.000548
16902.88	1.80423E-05	8.804861	792.7415	424.7272	0.000548
16994.75	1.79948E-05	8.780629	792.6945	424.6769	0.000548
17086.61	1.79474E-05	8.756463	792.6476	424.6265	0.000548
17178.48	1.79001E-05	8.732365	792.6006	424.5762	0.000548
17270.34	1.7853E-05	8.708332	792.5536	424.5259	0.000548
17362.2	1.7806E-05	8.684366	792.5066	424.4755	0.000548
17454.07	1.77591E-05	8.660466	792.4596	424.4252	0.000548
17545.93	1.77123E-05	8.636631	792.4126	424.3748	0.000548
17637.79	1.76656E-05	8.612862	792.3656	424.3245	0.000548

17729.66	1.76191E-05	8.589158	792.3186	424.2741	0.000548
17821.52	1.75727E-05	8.56552	792.2716	424.2238	0.000548
17913.38	1.75264E-05	8.541947	792.2246	424.1735	0.000548
18005.25	1.74803E-05	8.518439	792.1776	424.1231	0.000548
18097.11	1.74342E-05	8.494995	792.1306	424.0728	0.000548
18188.97	1.73883E-05	8.471616	792.0835	424.0224	0.000548
18280.84	1.73425E-05	8.448301	792.0365	423.9721	0.000548
18372.7	1.72968E-05	8.42505	791.9895	423.9218	0.000548
18464.56	1.72513E-05	8.401863	791.9425	423.8714	0.000548
18556.43	1.72059E-05	8.378741	791.8954	423.8211	0.000548
18648.29	1.71605E-05	8.355681	791.8484	423.7707	0.000548
18740.15	1.71153E-05	8.332686	791.8014	423.7204	0.000548
18832.02	1.70703E-05	8.309753	791.7543	423.6701	0.000548
18923.88	1.70253E-05	8.286884	791.7073	423.6197	0.000548
19015.75	1.69805E-05	8.264077	791.6602	423.5694	0.000548
19107.61	1.69358E-05	8.241334	791.6132	423.519	0.000548
19199.47	1.68912E-05	8.218653	791.5662	423.4687	0.000548
19291.34	1.68467E-05	8.196034	791.5191	423.4183	0.000548
19383.2	1.68023E-05	8.173478	791.472	423.368	0.000548
19475.06	1.67581E-05	8.150983	791.425	423.3177	0.000548
19566.93	1.67139E-05	8.128551	791.3779	423.2673	0.000548
19658.79	1.66699E-05	8.10618	791.3309	423.217	0.000548
19750.65	1.6626E-05	8.083871	791.2838	423.1666	0.000548
19842.52	1.65822E-05	8.061623	791.2367	423.1163	0.000548
19934.38	1.65386E-05	8.039437	791.1897	423.066	0.000548
20026.24	1.6495E-05	8.017311	791.1426	423.0156	0.000548
20118.11	1.64516E-05	7.995247	791.0955	422.9653	0.000548
20209.97	1.64082E-05	7.973243	791.0484	422.9149	0.000548
20301.83	1.6365E-05	7.9513	791.0014	422.8646	0.000548
20393.7	1.63219E-05	7.929417	790.9543	422.8143	0.000548
20485.56	1.6279E-05	7.907594	790.9072	422.7639	0.000548
20577.43	1.62361E-05	7.885832	790.8601	422.7136	0.000548
20669.29	1.61933E-05	7.864129	790.813	422.6632	0.000548
20761.15	1.61507E-05	7.842486	790.7659	422.6129	0.000548
20853.02	1.61082E-05	7.820903	790.7188	422.5625	0.000548
20944.88	1.60657E-05	7.799379	790.6717	422.5122	0.000548
21036.74	1.60234E-05	7.777914	790.6246	422.4619	0.000548
21128.61	1.59812E-05	7.756508	790.5775	422.4115	0.000548
21220.47	1.59392E-05	7.735161	790.5304	422.3612	0.000548
21312.33	1.58972E-05	7.713873	790.4833	422.3108	0.000548
21404.2	1.58553E-05	7.692644	790.4361	422.2605	0.000548
21496.06	1.58136E-05	7.671473	790.389	422.2102	0.000548
21587.92	1.57719E-05	7.65036	790.3419	422.1598	0.000548

21679.79	1.57304E-05	7.629306	790.2948	422.1095	0.000548
21771.65	1.5689E-05	7.608309	790.2477	422.0591	0.000548
21863.51	1.56477E-05	7.58737	790.2005	422.0088	0.000548
21955.38	1.56065E-05	7.566489	790.1534	421.9585	0.000548
22047.24	1.55654E-05	7.545665	790.1063	421.9081	0.000548
22139.11	1.55244E-05	7.524898	790.0591	421.8578	0.000548
22230.97	1.54835E-05	7.504189	790.012	421.8074	0.000548
22322.83	1.54427E-05	7.483537	789.9648	421.7571	0.000548
22414.7	1.54021E-05	7.462941	789.9177	421.7067	0.000548
22506.56	1.53615E-05	7.442402	789.8705	421.6564	0.000548
22598.42	1.53211E-05	7.42192	789.8234	421.6061	0.000548
22690.29	1.52807E-05	7.401494	789.7762	421.5557	0.000548
22782.15	1.52405E-05	7.381124	789.7291	421.5054	0.000548
22874.01	1.52004E-05	7.360811	789.6819	421.455	0.000548
22965.88	1.51604E-05	7.340553	789.6347	421.4047	0.000548
23057.74	1.51235E-05	7.320351	789.5073	421.2687	0.001217
23149.6	1.50859E-05	7.300204	789.4026	421.1569	0.001217
23241.47	1.50484E-05	7.280113	789.2978	421.0451	0.001217
23333.33	1.50109E-05	7.260078	789.193	420.9333	0.001217
23425.19	1.49736E-05	7.240097	789.0882	420.8215	0.001217
23517.06	1.49364E-05	7.220172	788.9834	420.7097	0.001217
23608.92	1.48992E-05	7.200301	788.8785	420.5979	0.001217
23700.78	1.48622E-05	7.180485	788.7737	420.4861	0.001217
23792.65	1.48252E-05	7.160723	788.6688	420.3743	0.001217
23884.51	1.47883E-05	7.141016	788.5639	420.2625	0.001217
23976.38	1.47516E-05	7.121363	788.459	420.1508	0.001217
24068.24	1.47149E-05	7.101765	788.3541	420.039	0.001217
24160.1	1.46783E-05	7.08222	788.2492	419.9272	0.001217
24251.97	1.46418E-05	7.062729	788.1443	419.8154	0.001217
24343.83	1.46054E-05	7.043291	788.0393	419.7036	0.001217
24435.69	1.45691E-05	7.023907	787.9344	419.5918	0.001217
24527.56	1.45328E-05	7.004577	787.8294	419.48	0.001217
24619.42	1.44967E-05	6.985299	787.7244	419.3682	0.001217
24711.28	1.44607E-05	6.966075	787.6194	419.2564	0.001217
24803.15	1.44247E-05	6.946904	787.5144	419.1446	0.001217
24895.01	1.43889E-05	6.927785	787.4093	419.0328	0.001217
24986.87	1.43531E-05	6.908719	787.3043	418.921	0.001217
25078.74	1.43174E-05	6.889705	787.1992	418.8092	0.001217
25170.6	1.42818E-05	6.870744	787.0942	418.6974	0.001217
25262.46	1.42463E-05	6.851835	786.9891	418.5856	0.001217
25354.33	1.42109E-05	6.832978	786.884	418.4738	0.001217
25446.19	1.41756E-05	6.814173	786.7788	418.362	0.001217
25538.06	1.41403E-05	6.79542	786.6737	418.2502	0.001217

25629.92	1.41052E-05	6.776718	786.5686	418.1384	0.001217
25721.78	1.40701E-05	6.758068	786.4634	418.0266	0.001217
25813.65	1.40352E-05	6.739469	786.3582	417.9148	0.001217
25905.51	1.40003E-05	6.720921	786.253	417.803	0.001217
25997.37	1.39655E-05	6.702424	786.1478	417.6912	0.001217
26089.24	1.39308E-05	6.683978	786.0426	417.5794	0.001217
26181.1	1.38962E-05	6.665583	785.9374	417.4676	0.001217
26272.96	1.38616E-05	6.647239	785.8322	417.3558	0.001217
26364.83	1.38272E-05	6.628945	785.7269	417.244	0.001217
26456.69	1.37928E-05	6.610701	785.6216	417.1322	0.001217
26548.55	1.37586E-05	6.592508	785.5163	417.0204	0.001217
26640.42	1.37244E-05	6.574365	785.411	416.9086	0.001217
26732.28	1.36903E-05	6.556271	785.3057	416.7968	0.001217
26824.14	1.36563E-05	6.538228	785.2004	416.685	0.001217
26916.01	1.36223E-05	6.520234	785.095	416.5732	0.001217
27007.87	1.35885E-05	6.502289	784.9897	416.4614	0.001217
27099.73	1.35547E-05	6.484394	784.8843	416.3496	0.001217
27191.6	1.35211E-05	6.466548	784.7789	416.2378	0.001217
27283.46	1.34875E-05	6.448752	784.6735	416.126	0.001217
27375.33	1.3454E-05	6.431004	784.5681	416.0142	0.001217
27467.19	1.34206E-05	6.413305	784.4627	415.9024	0.001217
27559.05	1.33872E-05	6.395655	784.3572	415.7906	-0.01509

Appendix C: Mars Flight Test Condition

```
// Set gravitational constant and planet radius to Martian

//world_model_cpg_configpar_flaginertia = 1;

WORLD_DATA_G = 17; // ft/s^2
WORLD_DATA_REARTH = 11142000; //
WORLD_DATA_REARTHPOLE = 11077000;
WORLD_DATA_GM = WORLD_DATA_REARTH^2*WORLD_DATA_G;

// Apply configuration
//exec("xaconfig.exc",1); exec("xatestcond.exc",1);

WORLD_DATA_G = 12.171916; // ft/s^2

// Apply configuration
//exec("xaconfig.exc",1); exec("xatestcond.exc",1);

// Not sure that this is actually needed
world_data_gravity = [0,0,world_data_g];
world_model_DATA_G0 = WORLD_DATA_G;
world_model_environ_data_g0 = world_data_g;


// FLightlab hardcoded 2 blade to call mhatinv -
//This is a way to circumvent it, as it tends to becomes singular
//WORLD_MODEL_ROTOR1_ROTOR_DATA_ISNEEDMHATINV = 0;
//WORLD_MODEL_ROTOR2_ROTOR_DATA_ISNEEDMHATINV = 0;


// Set test conditions for low flight in MC2 conditions
           world_model_cpg_testcond_atmflg = 0; // Given that the Mars atm
table is the fourth opt
           world_model_cpg_testcond_hpres = 2800; // [ft] Set desired
pressure altitude.
           world_model_cpg_testcond_TAMB = -49.95; // [degC]  Set desired
ambient temperature t 223.2 in K
// Apply configuration
//exec("xaconfig.exc",1);
exec("xatestcond.exc",1);
exec("assemble.exc",1);
```

Appendix D: Eigenvalues of Earth and Mars from FLIGHTLAB and CAMRAD

FLIGHTLAB			
Mars (Real and imag)		Earth (Real and Imag)	
0.00	0.00	0	0
0.00	0.00	0	0
0.00	0.00	0	0
0.00	0.00	0	0
0.00	0.00	0	0
0.00	0.00	0	0
0.00	0.00	0	0
-1.69	742.12	-17.1675	445.691
-1.69	-742.12	-17.1675	-445.691
-1.69	741.95	-17.4929	440.0697
-1.69	-741.95	-17.4929	-440.07
-1.70	742.04	-24.0721	393.03
-1.70	-742.04	-24.0721	-393.03
-1.69	739.80	-24.1171	393.257
-1.69	-739.80	-24.1171	-393.257
-1.71	739.80	-24.1015	397.8157
-1.71	-739.80	-24.1015	-397.816
-1.42	568.91	-24.3114	292.3715
-1.42	-568.91	-24.3114	-292.372
-1.43	561.71	-24.3084	292.3244
-1.43	-561.71	-24.3084	-292.324
-1.73	739.79	-24.3343	290.5589
-1.73	-739.79	-24.3343	-290.559
-1.73	470.51	-24.267	396.7573
-1.73	-470.51	-24.267	-396.757
-1.24	167.72	-24.267	396.7573
-1.24	-167.72	-24.267	-396.757
-1.24	167.32	-24.267	396.7573
-1.24	-167.32	-24.267	-396.757
-207.19	0.00	-22.7983	361.2173
-207.17	0.00	-22.7983	-361.217
-206.90	0.00	-24.4223	290.0006
-204.74	0.00	-24.4223	-290.001
-204.94	0.00	-24.4223	290.0006

-204.93	0.00	-24.4223	-290.001
-1.27	157.29	-24.4223	290.0006
-1.27	-157.29	-24.4223	-290.001
-1.27	157.19	-24.5708	344.6397
-1.27	-157.19	-24.5708	-344.64
-381.97	0.06	-48.4143	0
-381.97	-0.06	-47.9045	0
-381.97	0.05	-4.4404	0
-381.97	-0.05	-4.3159	0
-381.98	0.05	-39.1	0
-381.98	-0.05	-36.1722	0
-1.27	157.19	-0.0342	0.6098
-1.27	-157.19	-0.0342	-0.6098
-385.87	0.06	-0.0329	0.6095
-385.87	-0.06	-0.0329	-0.6095
-385.88	0.05	-66.9086	0
-385.88	-0.05	-66.784	0
-1.28	157.19	-0.725	0
-1.28	-157.19	-65.7849	0.4082
-385.87	0.05	-65.7849	-0.4082
-385.87	-0.05	-65.926	0
-1.83	448.86	-65.897	0
-1.83	-448.86	-24.6232	344.3264
-1.83	448.53	-24.6232	-344.326
-1.83	-448.53	-24.6232	344.3264
-1.83	448.53	-24.6232	-344.326
-1.83	-448.53	-36.1339	0
-0.63	0.00	-36.1339	0
-0.61	0.00	-1.1248	0
0.06	0.28	-65.7014	0.5708
0.06	-0.28	-65.7014	-0.5708
0.06	0.27	-65.7013	0.5708
0.06	-0.27	-65.7013	-0.5708
-0.05	0.00	-65.7013	0.5708
-1.99	448.81	-65.7013	-0.5708
-1.99	-448.81	-0.0008	0
-1.99	448.82	-24.7277	345.2694
-1.99	-448.82	-24.7277	-345.269
-1.95	448.81	0	0
-1.95	-448.81	0	0
-1.95	448.81	-24.7277	345.2694

-1.95	-448.81	-24.7277	-345.269
-1.95	448.81	-24.7277	345.2694
-1.95	-448.81	-24.7277	-345.269
-0.09	0.00	-24.7277	345.2694
-1.99	448.81	-24.7277	-345.269
-1.99	-448.81	-24.7277	345.2694
0.00	0.00	-24.7277	-345.269
0.00	0.00	-24.7277	345.2694
0.00	0.00	-24.7277	-345.269

CAMRAD			
Mars (Real and imag)		Earth (Real and Imag)	
-1.5138	559.14	-18.0466	431.8585
-1.5138	-559.14	-18.0466	-431.859
-1.527	552.65	-18.3904	426.8374
-1.527	-552.65	-18.3904	-426.837
-1.8418	738.32	-25.4073	383.8596
-1.8418	-738.32	-25.4073	-383.86
-1.8393	738.62	-25.3517	383.6122
-1.8393	-738.62	-25.3517	-383.612
-1.8461	738.76	-25.4859	388.6103
-1.8461	-738.76	-25.4859	-388.61
-1.8642	736.48	-23.8586	352.0759
-1.8642	-736.48	-23.8586	-352.076
-1.8634	736.47	-25.6215	387.4899
-1.8634	-736.47	-25.6215	-387.49
-1.8634	736.47	-25.6215	387.4894
-1.8634	-736.47	-25.6215	-387.489
-1.799	467.08	-25.6215	387.4896
-1.799	-467.08	-25.6215	-387.49
-1.8968	445.47	-25.1131	282.9682
-1.8968	-445.47	-25.1131	-282.968
-1.9011	445.13	-25.1089	282.9134
-1.9011	-445.13	-25.1089	-282.913
-1.9005	445.13	-25.1397	281.1695
-1.9005	-445.13	-25.1397	-281.17
-1.2908	164.27	-25.8284	335.3425
-1.2908	-164.27	-25.8284	-335.343
-1.2906	163.88	-25.8712	335.0087
-1.2906	-163.88	-25.8712	-335.009

-2.1196	445.47	-25.8716	335.0077
-2.1196	-445.47	-25.8716	-335.008
-1.3372	153.98	-25.2033	280.5832
-1.3372	-153.98	-25.2033	-280.583
-1.3389	153.88	-25.2033	280.5835
-1.3389	-153.88	-25.2033	-280.584
-1.3385	153.88	-25.2033	280.5838
-1.3385	-153.88	-25.2033	-280.584
-1.3385	153.88	-26.3624	336.1548
-1.3385	-153.88	-26.3624	-336.155
-0.86057	0	-5.6494	0
-0.84196	0	-5.4992	0
0.13561	0.47319	0.0319	1.0578
0.13561	-0.47319	0.0319	-1.0578
0.13959	0.46889	0.0446	1.0542
0.13959	-0.46889	0.0446	-1.0542
-0.10432	0	-1.3978	0
-0.049482	0	-0.6259	0
-247.83	0	-56.6194	0
-247.75	0	-56.1115	0
-247.39	0	-47.2983	0
-247.27	0	-44.2436	0
-247.23	0	-44.2164	0
-247.22	0	-44.2172	0
-450.77	0.45675	-79.1564	0.0509
-450.77	-0.45675	-79.1564	-0.0509
-450.58	0.46953	-78.4251	0.029
-450.58	-0.46953	-78.4251	-0.029
-450.59	0.46689	-78.3972	0.318
-450.59	-0.46689	-78.3972	-0.318
-450.59	0.46325	-78.349	0.3973
-450.59	-0.46325	-78.349	-0.3973
-450.59	0.46349	-78.35	0.3973
-450.59	-0.46349	-78.35	-0.3973
-450.59	0.46349	-78.35	0.3973
-450.59	-0.46349	-78.35	-0.3973
-2.1174	445.47	-26.3624	336.1548
-2.1174	-445.47	-26.3624	-336.155
-2.1174	445.47	-26.3625	336.1548
-2.1174	-445.47	-26.3625	-336.155
-2.1174	445.47	-26.3625	336.1548

-2.1174	-445.47	-26.3625	-336.155
-2.1174	445.47	-26.3624	336.1548
-2.1174	-445.47	-26.3624	-336.155
-2.1174	445.47	-26.3624	336.1548
-2.1174	-445.47	-26.3624	-336.155

Appendix F: Matlab Script to Plot Frequency Responses from CAMRAD and FLIGHTLAB

```
%% Load state-space system matrices for Mars
camradoutputpath='.'; % Path pointing to where you've unpacked the CAMRAD output
[A,B,C,D]=readcamrad(fullfile(camradoutputpath,'hexdyn.out.txt'),74,13,0); %
'hexdyn.out.txt' corresponds to hover case
%% Calculate relevant quantities for Mars-CAMRAD
E=eig(A); % eigenvalues
w=logspace(-4,4,1000);
clearvars('H');
B(:,2)=-B(:,2);
G=ss(A,B,[zeros(4,2) eye(4) zeros(4,68)],0);
for i=1:4;
    H(:,i)=squeeze(freqresp(G(i,i),w));
    figure(i);
    bode(frd(H(:,i),w));

end
% figure(5);
% plot(E,'x');
Mag=abs(H);
Phase=unwrap(angle(H))*180/pi;

%% CAMRAD Results for Mars

CM_response1=Mag(:,1);
CM_response2=Mag(:,2);
CM_response3=Mag(:,3);
CM_response4=Mag(:,4);


%convert amp mag to DB
CM_response1_db=20.*log10(CM_response1);
CM_response2_db=20.*log10(CM_response2);
CM_response3_db=20.*log10(CM_response3);
CM_response4_db=20.*log10(CM_response4);

CM_response=[CM_response1_db, CM_response2_db, CM_response3_db, CM_response4_db];

%Camrad Phase data in deg

phase_degrees2=[Phase(:,1),Phase(:,2), Phase(:,3), Phase(:,4)];

%Camrad Euler Representatin
complexVector5 = [10.^(CM_response(:,1)./20) .* exp(1j*deg2rad(phase_degrees2(:,1)))]
complexVector6 = [10.^(CM_response(:,2)./20) .* exp(1j*deg2rad(phase_degrees2(:,2)))]
complexVector7 = [10.^(CM_response(:,3)./20) .* exp(1j*deg2rad(phase_degrees2(:,3)))]
complexVector8 = [10.^(CM_response(:,4)./20) .* exp(1j*deg2rad(phase_degrees2(:,4)))]
%
% % Using FRD for Heave
```

```
% fl1=frd(complexVector1,Frequency);
cm1=frd(complexVector5,w);
% fl2=frd(complexVector2,Frequency);
cm2=frd(complexVector6,w);
% fl3=frd(complexVector3,Frequency);
cm3=frd(complexVector7,w);
% fl4=frd(complexVector4,Frequency);
cm4=frd(complexVector8,w);



%% Load state-space system matrices for Earth-CAMRAD
camradoutputpath='.'; % Path pointing to where you've unpacked the CAMRAD output
[A1,B1,C1,D1]=readcamrad(fullfile(camradoutputpath,'hexdyn-earth.out.txt'),74,13,0);
% 'hexdyn.out.txt' corresponds to hover case
%% Calculate relevant quantities for Earth
E1=eig(A1); % eigenvalues
w1=logspace(-4,4,1000);
clearvars('H1');
B1(:,2)=-B1(:,2);
G1=ss(A1,B1,[zeros(4,2) eye(4) zeros(4,68)],0);
for i=1:4;
    H1(:,i)=squeeze(freqresp(G1(i,i),w1));
    figure(i);
    bode(frd(H1(:,i),w1));

end
% figure(5);
% plot(E1,'x');
Mage=abs(H1);
Phase1=unwrap(angle(H1))*180/pi;

%% CAMRAD Results for Earth

CM_response1e=Mage(:,1);
CM_response2e=Mage(:,2);
CM_response3e=Mage(:,3);
CM_response4e=Mage(:,4);


%convert amp mag to DB
CM_response1_dbe=20.*log10(CM_response1e);
CM_response2_dbe=20.*log10(CM_response2e);
CM_response3_dbe=20.*log10(CM_response3e);
CM_response4_dbe=20.*log10(CM_response4e);

CM_responsee=[CM_response1_dbe, CM_response2_dbe, CM_response3_dbe,
CM_response4_dbe];

%Camrad Phase data in deg

phase_degrees2e=[Phase1(:,1),Phase1(:,2), Phase1(:,3), Phase1(:,4)];

%Camrad Euler Representatin
```

```
complexVector5e = [10.^(CM_responsee(:,1)./20) .*
exp(1j*deg2rad(phase_degrees2e(:,1)))]
complexVector6e = [10.^(CM_responsee(:,2)./20) .*
exp(1j*deg2rad(phase_degrees2e(:,2)))]
complexVector7e = [10.^(CM_responsee(:,3)./20) .*
exp(1j*deg2rad(phase_degrees2e(:,3)))]
complexVector8e = [10.^(CM_responsee(:,4)./20) .*
exp(1j*deg2rad(phase_degrees2e(:,4)))]

% Using FRD
% fl1e=frd(complexVector1e,Frequency);
cm1e=frd(complexVector5e,w1);
% fl2e=frd(complexVector2e,Frequency);
cm2e=frd(complexVector6e,w1);
% fl3e=frd(complexVector3e,Frequency);
cm3e=frd(complexVector7e,w1);
% fl4e=frd(complexVector4e,Frequency);
cm4e=frd(complexVector8e,w1);
%

%% Flightlab model for Earth-System Matrices
E9=eig(F5); % eigenvalues
w=logspace(-4,4,1000);
clearvars('m');
% %B(:,2)=-B(:,2);
G2=ss(F5,G5,H5,0);
 for i=1:4
     m(:,i)=squeeze(freqresp(G2(i,i),w));
%       figure(i);
%       bode(frd(m(:,i),w));

 end
%  figure(5);
%  plot(E,'x');
 Magm=abs(m);
 Phasem=unwrap(angle(m))*180/pi;
%%
CM_response1m=Magm(:,1);
CM_response2m=Magm(:,2);
CM_response3m=Magm(:,3).*0.304;
CM_response4m=Magm(:,4);


%convert amp mag to DB
CM_response1_dbm=20.*log10(CM_response1m);
CM_response2_dbm=20.*log10(CM_response2m);
CM_response3_dbm=20.*log10(CM_response3m);
CM_response4_dbm=20.*log10(CM_response4m);

CM_responsem=[CM_response1_dbm, CM_response2_dbm, CM_response3_dbm,
CM_response4_dbm];

%Camrad Phase data in deg

phase_degrees2m=[Phasem(:,1),Phasem(:,2), Phasem(:,3), Phasem(:,4)];
```

```
%Camrad Euler Representatin
complexVector5m = [10.^(CM_responsem(:,1)./20) .*
exp(1j*deg2rad(phase_degrees2m(:,1)))]
complexVector6m = [10.^(CM_responsem(:,2)./20) .*
exp(1j*deg2rad(phase_degrees2m(:,2)))]
complexVector7m = [10.^(CM_responsem(:,3)./20) .*
exp(1j*deg2rad(phase_degrees2m(:,3)))]
complexVector8m = [10.^(CM_responsem(:,4)./20) .*
exp(1j*deg2rad(phase_degrees2m(:,4)))]

% Using FRD for Heave
fl1m=frd(complexVector5m,w);
% cm1=frd(complexVector5,w);
fl2m=frd(complexVector6m,w);
% cm2=frd(complexVector6,w);
fl3m=frd(complexVector7m,w);
% cm3=frd(complexVector7,w);
fl4m=frd(complexVector8m,w);
% cm4=frd(complexVector8,w);

 %% Plotting for Earth

o=bodeoptions('cstprefs');
o.xlim=[0.1 1000]
o.PhaseMatching='on'
o.phasematchingfreq=100
 bode(fl3m,o)
hold on


 bode(cm1e,'--r',o)
hold off

 legend({'Flightlab', 'Camrad'},'location','southwest')
 title('w/Col')

 figure
 bode(fl2m,o)
 hold on


 bode(cm2e,'--r',o)
 hold off
 legend({'Flightlab', 'Camrad'},'location','southwest')
 title('p/Lat')


 figure,
 bode(fl1m,o)
hold on


bode(cm3e,'--r',o)
hold off
```

```
legend({'Flightlab', 'Camrad'},'location','southwest')
 title('q/Lon')

 figure,
 bode(fl4m,o)
hold on


bode(cm4e,'--r',o);
hold off
legend({'Flightlab', 'Camrad'},'location','southwest')
 title('r/Ped')

 %% Compare Eigenvalues of eARTH-system Matrices
figure,

plot(E9,'x');
xlim([-100 100])
hold on
plot(E1,'o');
legend({'FLIGHTLAB', 'CAMRAD'},'location','southwest')
title('Eigenvalues')



%% Flightlab model for Mars-System Matrices
E6=eig(F7); % eigenvalues
w=logspace(-4,4,1000);
clearvars('l');
% %B(:,2)=-B(:,2);
G2m=ss(F7,G7,H7,0);
 for i=1:4
     l(:,i)=squeeze(freqresp(G2m(i,i),w));
     figure(i);
     bode(frd(l(:,i),w));

 end
%  figure(5);
%  plot(E,'x');
 Magmr=abs(l);
 Phasemr=unwrap(angle(l))*180/pi;
%%
CM_response1mr=Magmr(:,1); %pitch rate
CM_response2mr=Magmr(:,2);%roll rate
CM_response3mr=Magmr(:,3).*0.4;%Vz body
CM_response4mr=Magmr(:,4);%Yaw rate


%convert amp mag to DB
CM_response1_dbmr=20.*log10(CM_response1mr);
CM_response2_dbmr=20.*log10(CM_response2mr);
CM_response3_dbmr=20.*log10(CM_response3mr);
CM_response4_dbmr=20.*log10(CM_response4mr);
```

```
CM_responsemr=[CM_response1_dbmr, CM_response2_dbmr, CM_response3_dbmr,
CM_response4_dbmr];

%Camrad Phase data in deg

phase_degrees2mr=[Phasemr(:,1),Phasemr(:,2), Phasemr(:,3), Phasemr(:,4)];

%Camrad Euler Representatin
complexVector5mr = [10.^(CM_responsemr(:,1)./20) .*
exp(1j*deg2rad(phase_degrees2mr(:,1)))]
complexVector6mr = [10.^(CM_responsemr(:,2)./20) .*
exp(1j*deg2rad(phase_degrees2mr(:,2)))]
complexVector7mr = [10.^(CM_responsemr(:,3)./20) .*
exp(1j*deg2rad(phase_degrees2mr(:,3)))]
complexVector8mr = [10.^(CM_responsemr(:,4)./20) .*
exp(1j*deg2rad(phase_degrees2mr(:,4)))]

% Using FRD for Heave
fl1mr=frd(complexVector5mr,w);
% cm1=frd(complexVector5,w);
fl2mr=frd(complexVector6mr,w);
% cm2=frd(complexVector6,w);
fl3mr=frd(complexVector7mr,w);
% cm3=frd(complexVector7,w);
fl4mr=frd(complexVector8mr,w);
% cm4=frd(complexVector8,w);

 %% Plotting for Mars-system matrices

o=bodeoptions('cstprefs');
o.xlim=[0.1 1000]
o.phasematchingfreq=100
 bode(fl3mr,o)
hold on


 bode(cm1,'--r',o)
hold off


 legend({'FLIGHTLAB', 'CAMRAD'},'location','southwest')
 title('w/Col')

 figure
 bode(fl2mr,o)
 hold on


 bode(cm2,'--r',o)
 hold off
 legend({'FLIGHTLAB', 'CAMRAD'},'location','southwest')
 title('p/Lat')


 figure,
```

```
 bode(fl1mr,o)
hold on


bode(cm3,'--r',o)
hold off
legend({'FLIGHTLAB', 'CAMRAD'},'location','southwest')
 title('q/Lon')

 figure,
 bode(fl4mr,o)
hold on


bode(cm4,'--r',o);
hold off
legend({'FLIGHTLAB', 'CAMRAD'},'location','southwest')
 title('r/Ped')

 %% Compare Eigenvalues of Mars-system Matrices
figure,

plot(E6,'x');
xlim([-500 500])
hold on
plot(E,'o');
legend({'FLIGHTLAB', 'CAMRAD'},'location','southwest')
title('Eignevalues')

%% Comparing Mars and earth Dynamics-Flightlab
figure,
o=bodeoptions('cstprefs');

o.xlim=[0.1 1000]
o.PhaseMatching='on'
o.phasematchingfreq=100
bodeplot(fl3mr,o)

 hold on

bodeplot(fl3m,'--r',o)
hold on
legend({'Mars', 'Earth '},'location','southwest')
title('w/col')


 figure
 bodeplot(fl2mr,o)
 hold on


 bodeplot(fl2m,'--r',o)
hold on
%  sglegend({'Mars', 'Earth '},'location','bestoutside')
 title('p/Lat')
```

```
legend({'Mars', 'Earth '},'location','southwest')

figure,
bodeplot(fl1mr,o);
hold on
bodeplot(fl1m,'--r',o);
hold on
legend({'Mars', 'Earth '},'location','southwest')
title('q/Lon')

 figure

bodeplot(fl4mr,o)
hold on


bodeplot(fl4m,'--r',o);
hold off
legend({'Mars', 'Earth '},'location','southwest')
title('r/Ped')
 %%
 figure,

plot(E9,'x');
xlim([-400 400])
hold on
plot(E6,'o');
legend({'Earth', 'Mars'},'location','southwest')
title('Eignevalues')

%%
pzplot(G2m)
hold on
pzplot(G)
% xlim([0 .05])
% ylim([-2 2])
legend({'FLIGHTLAB', 'COMRAD'},'location','southwest')
```